Elucidating the origins of hysteresis and reaction mechanisms of electrode materials for Li and Na batteries

by

Donghee Chang

A dissertation submitted in partial fulfillment
of the requirements for the degree of
Doctor of Philosophy
(Materials Science and Engineering)
in The University of Michigan
2015

Doctoral Committee:

Associate Professor Anton Van der Ven, Co-Chair
Assistant Professor Emmanouil Kioupakis, Co-Chair
Assistant Professor Pierre Ferdinand P. Poudeu
Assistant Professor Donald J. Siegel

To my parents

ACKNOWLEDGEMENTS

First of all, I would like to express the deepest appreciation to my wonderful advisor, Anton Van der Ven for his great mentoring. He led me to finish my graduate study with constant encouragement and great patience. His expert guidance was essential to making this thesis possible.

I appreciate my thesis committee members, Professor Emmanouil Kioupakis, Donald J. Siegel and Pierre Ferdinand P. Peudeu. Their collective mentorship and support enhanced the depth of my research.

Professor Peter Khalifah and his graduate student Jue Liu were a great pleasure to collaborate with for the Na-CUBICON electrodes system. It was also a great pleasure to collaborate with Professor Xiaoqing Pan and his graduate student Sungjoo Kim for the lithiated titania polymorphs system. Collaboration with them broadened my research area and provided more depth to my research.

I also express special thanks to John Thomas, Qinqchuan Xu, and Brian Puchala. All of them are great teachers. Without their help during the first years of graduate school, it must have been pretty tough for me when I started my research.

I am also grateful to members of our group, in particular Anna Belak, John Goiri, Min-Hua (Ivy) Chen, Alexandra Emly, Anirudh Raju Natarajan and Max Radin. All of them are great friends and I learned a great deal from interactions with them. I thank Yizhou Wang for the elastic modulus calculation, who was an undergraduate student joined our group previously. I also thank Min-Hua Chen for performing the phonon calculations in the Li-Cu_2Sb system.

I also thank Renee Hilgendorf for her tireless assistance. Without her help, preparation for the administrative requirements would have been very difficult.

Lastly, but most importantly, I thank my parents and family for their unconditional love and constant support throughout my life and graduate school years. Their encouragement has been the most powerful source to motivation to overcome any difficulties. I thank my soon-to-be husband, Songjoo Kim again. He is my best friend, colleague, and great motivator. His great patience, love, thoughtfulness and great humor were vital to make this all possible.

TABLE OF CONTENTS

LIST OF FIGURES

Figure

LIST OF TABLES

Table

ABSTRACT

Elucidating the origins of hysteresis and reaction mechanisms of electrode materials for Li and Na batteries

by

Donghee Chang

Chair: Anton Van der Ven and Emmanouil Kioupakis

Voltage hysteresis and irreversibility upon electrochemical cycling of promising electrode chemistries are major impediments to increasing the energy density of Li ion batteries. To understand the origins of hysteresis and irreversibility, we performed a first principles study of the electronic, thermodynamic and kinetic properties of various anode materials undergoing three different types of reactions: intercalation, conversion (displacement), and alloying.

We investigate the origins of phase transformation hysteresis in electrodes of Li-ion batteries, focusing on the alloying reaction of Li with Sb. To this end, we perform a first-principles calculation of the thermodynamic and kinetic properties of Sb, Li_2Sb and Li_3Sb, three phases that can coexist as Li reacts with Sb. We identify a lever effect in the driving force for nucleation at high overpotentials that favors phases with large changes in Li concentration over phases that are closer in composition along the equilibrium charge or discharge path.

Electrode materials undergoing displacement and conversion reactions can achieve very high capacities, but also suffer from a variety of limitations that need to be

overcome. These include a poor reversibility and large capacity losses during charge and discharge. One exception to this trend is Cu_2Sb, a candidate anode material that undergoes a displacement reaction with Li, but exhibits only a limited degree of hysteresis in the voltage profile between charge and discharge. We perform a comprehensive first-principles study of Cu_2Sb to elucidate the intrinsic properties of the various reaction compounds that facilitate reversibility and minimize hysteresis between discharge and charge.

We also considered the origins of irreversibility of TiO_2(B), a promising intercalation compound. We found that a phase transformation from $LiTi_2O_4$(B) to anatase based $LiTi_2O_4$ is energetically possible and occurs along a strain invariant plane common to both anatase $LiTi_2O_4$ and $LiTi_2O_4$(B).

In addition to investigating the origins of hysteresis, we also studied the electrochemistry of novel intercalation host materials such as $CaTi_5O_{11}$ and $Na_3TiP_3O_9N$ for Li-ion and Na-ion battery applications, respectively.

CHAPTER I

Introduction

1.1 Current Li-ion and Na-ion batteries and needs

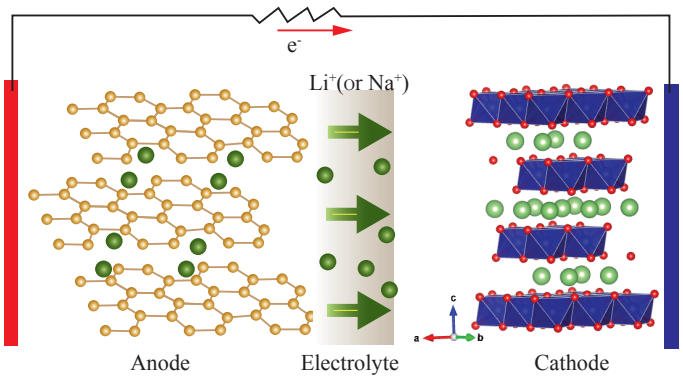

Figure 1.1: Schematic illustration of a Li-ion (or Na-ion) battery based on intercalation reaction during the discharge reaction.

Most electrode materials currently used in Li and Na batteries are intercalation compounds. As illustrated in Fig 1.1 upon discharge of battery, Li (or Na) ions are released from an anode and move to a cathode through an electrolyte. This type of reaction results in a valence shift of a transition metal ion. Fig 1.2 shows typical intercalation compounds employed in commercialized Li-ion batteries. While graphite is the most commonly used anode material, various transition metal oxides including $LiMnO_2$, $LiCoO_2$, and $LiFePO_4$ can serve as cathode materials. Although there are

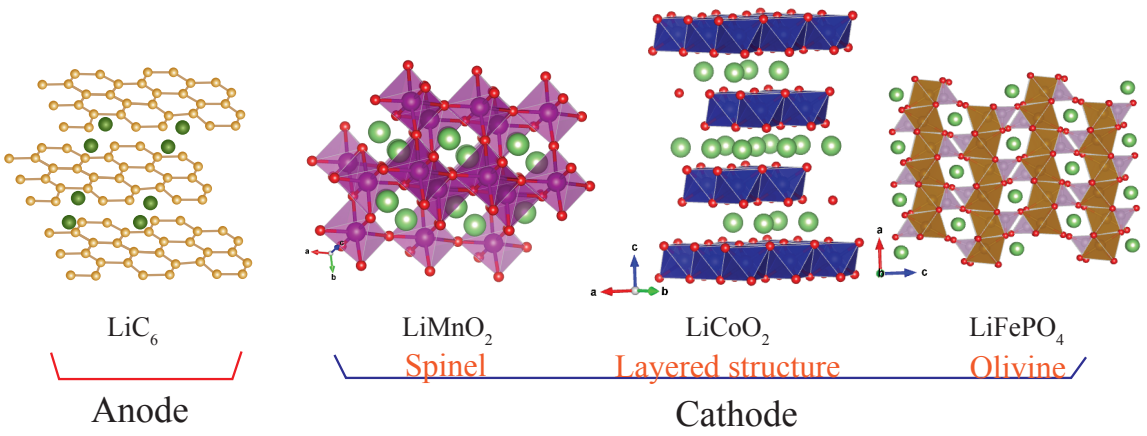

Figure 1.2: Intercalation compounds used in commercialized Li ion batteries

no electrode materials for commercially viable Na-ion batteries up to date, phosphate based materials such as $NaFePO_4$, $NaVPO_4F$, $Na_3V_2(PO_4)_3$, $Na_3V_2(PO_4)_2F_3$ have been considered as the most promising candidates to be cathodic materials.[56, 89, 35]

In an intercalation reaction, Li (or Na) ions are inserted or extracted from interstitial sites of the host structure without causing substantial structural degradation. This makes intercalation compounds an ideal class of materials for electrochemical energy storage applications. However, intercalation compounds have a limited capacity due to crystallographic constraints of the host and thermodynamic instabilities arising from large changes in Li (or Na) concentration within the host. Indeed in most practical applications, intercalation compounds only react with 0.5 electrons per transition metal.[86]

Hence, in order to increase the energy capacity of electrochemical energy storage, there has been a considerable interest in finding alternative electrode chemistries that undergo different solid-state reaction mechanisms.

1.2 Motivation and Overview

Alloying reactions and conversion reactions have been heavily investigated over the past decades as alternative solid-sate reaction mechanisms.[17, 73] Unlike an intercalation reaction, a conversion reaction is able to accommodate as many electrons per transitional metal, M, needed to reduce its metallic state M^{n+}.[66] Therefore, electrode materials undergoing conversion reactions can achieve much higher capacities than currently commercialized intercalation compounds. For example, FeF_2, a well known conversion reaction cathode material, has a theoretical capacity of 571 $mAhg^{-1}$,[2, 86] which is much higher than that of graphite (372 $mAhg^{-1}$). A conversion reaction can be classified into two types: pure conversion and displacement reaction. When the starting compound has a strong structural relationship with its lithiated products, the conversion reaction is usually called as displacement reaction.[49, 84]

Another possible reaction mechanism to achieve a high capacity is via Li (or Na) reacting directly with another element and forming a well-defined intermetallic phase (Li_xM, or Na_xM); this is called an alloying reaction.[87, 43, 25, 23] Good examples are Si and Sn that can form intermetallic compounds having very high Li concentrations (e.g. $Li_{3.75}Si$ and $Li_{4.4}Sn$). The theoretical capacities of Si and Sn are 3579 $mAhg^{-1}$ and 993 $mAhg^{-1}$ respectively.[26, 16, 54]

However, those materials exhibit a large hysteresis in the voltage profile and have very poor reversibility. A large hysteresis leads to irreversible energy loss upon cycling, and this makes commercialization difficult.

A fundamental understanding of the factors that cause hysteresis in electrodes undergoing complex solid-state reaction mechanisms is still quite limited. Therefore, a main focus of this thesis is to explain the causes of hysteresis in Li-ion battery electrodes that undergo either alloying or conversion reactions. There are several sources of hysteresis in solid-state electrochemical reactions. One is purely dissipative

and emerges from sluggish kinetics on the timescale of the charge and discharge cycle. Slowing the charge and discharge rate can systematically reduce this form of polarization. Hysteresis in the voltage profile will also emerge if the reaction follows a different path during discharge compared to that followed during charge.[21, 90] The resulting path hysteresis arises due to an asymmetry in competing kinetic mechanisms and becomes more likely as the number of accessible kinetic mechanisms of ion insertion/removal increases.[90] A third source of hysteresis can arise due to mechanical dissipation, either when coherency strains need to be overcome during two-phase coexistence[81] or in the form of plastic deformation, likely an important factor in some alloying reactions undergoing large volume changes.[51]

For alloying reactions, we consider the Sb electrode. Although Sb has a smaller specific capacity (660 $mAhg^{-1}$[58]) than Si and Sn, it undergoes a smaller volume change and fewer phase transformations upon reaction with Li. The electrochemical reaction of Li with Sb electrode is also accompanied by path hysteresis with different discharge and charge voltage profiles. However, interestingly, in spite of this, the charge and discharge profiles as well as the capacity do not change much over the different cycles in contrast to Si and Sn electrodes, which show large irreversible capacity loss.

To explore hysteresis in conversion reactions, we investigate Cu_2Sb which undergoes a displacement reaction with Li. Almost all electrode compounds that rely on a displacement or a conversion reaction exhibit a large hysteresis in the voltage profile between charge and discharge. However, Cu_2Sb exhibits a very small voltage hysteresis in the voltage profile upon charge and discharge. Our aim is, therefore, to determine what about the intrinsic properties of the Li+Cu_2Sb system allows it to cycle with minimal hysteresis.

We also investigate the causes of irreversibility in intercalation reactions due to phase transformations to more stable crystal structures upon Li insertion. From

the *in situ* high-resolution transmission electron microscopy (HRTEM) performed by Sungjoo Kim, a strain-induced phase transformation upon Li ion insertion into TiO_2(B) was observed. The irreversible phase transformation upon Li ion insertion also leads to energy losses during cycling. Thus we investigate phase stability of TiO_2 polymorphs and predict a possible phase transformation mechanism upon Li intercalation in TiO_2(B).

Lastly, $CaTi_5O_{11}$ and $Na_3TiP_3O_9N$ are investigated as a novel structural framework undergoing intercalation reactions in Li-ion and Na-ion batteries respectively. We explore the possible Li and Na sites and suggest possible diffusion mechanisms using first principles methodes.

CHAPTER II

Computational Method

To calculate the thermodynamic and kinetic properties of solids from first principles, we follow a two-step approach: (1) construct a cluster expansion and (2) perform Monte Carlo simulations. In this chapter, we will review first-principles calculations briefly and discuss the method for construction of the cluster expansion and the relevant basics of Monte Carlo simulations.

2.1 First-principles calculations

The energies of various atomic arrangements are essential ingredients for the construction of a cluster expansion Hamiltonian and the determination of phase stability. These energies must be calculated from first principles by solving the many-body time-independent Schrodinger equation:

$$H\Psi = E\Psi \tag{2.1}$$

where H is the Hamiltonian operator for the solid, Ψ is the many body wave function for the electrons, and E is the total energy of the solid. Within the Born-Oppenheimer approximation, ion and electron wave functions are independent from each other due to the large difference in their masses[14, 45]. Then the Hamiltonian can be simplified

as:

$$H = T_e + V_{en} + V_{ee} + V_{nn} \tag{2.2}$$

where T_e is the electronic kinetic energy operator which can be expressed as:

$$T_e = -\frac{1}{2}\sum_j \nabla_j^2 \tag{2.3}$$

V_{en} and V_{ee} describe the coulombic interactions between the nuclei and the electrons of the solid, and between the two different electrons respectively. These terms can be written as:

$$V_{en} = \sum_j \upsilon(\vec{r_j}) \tag{2.4}$$

$$V_{ee} = \sum_j \sum_{j<i} \frac{1}{|\vec{r_j} - \vec{r_i}|} \tag{2.5}$$

where $\vec{r_j}$ refers to the positions of the electrons. The last term in 2.2 is the Ewald energy arising from the coulombic interaction between the nuclei with charge Z_m and can be denoted as:

$$V_{nn} = \sum_n \sum_{m<n} \frac{Z_m Z_n}{|\vec{R_m} - \vec{R_n}|} \tag{2.6}$$

where $\vec{R_m}$ is the coordinates of the nuclei. V_{nn} is simply an additive term to obtain the total energy of the crystal. Then, the total energy E,

$$E = \frac{\langle\Psi|H|\Psi\rangle}{\langle\Psi|\Psi\rangle} \tag{2.7}$$

is the expectation value of the Hamiltonian.

However, it is well known that solving the many body Schrodinger equation is impos-

sible for realistic solids.[45, 69] Many approximations have been proposed to solve this problem such as the Hartree-Fock (HF) approach, Density Functional Theory (DFT), and various hybrid methods. However, the HF method is limited to simple systems because the full wave function is approximated by a product of individual electron wave functions.[69, 4] The DFT method avoids the full wave function by using the electron density, n(r), which describes the density of electrons at a particular position, r, in space.[69] While formally equivalent with the original Schrodinger equation for the many body wave function, the DFT is more suited for the introduction of approximation. Thus, all of the first principles calculations in this thesis are performed using the DFT.

2.1.1 Density Functional Theory

The fundamental theorems of DFT state that the ground state properties of a crystal are uniquely determined by the electron density.[42, 45, 59, 69]

The ground state energy functional can be written as:

$$E[\rho] = T_s[\rho] + J[\rho] + E_{xc}[\rho] + \int \rho(\vec{r})\upsilon(\vec{r})d\vec{r} \tag{2.8}$$

$$with \quad \rho(\vec{r}) = \sum_j \psi_j^*(\vec{r})\psi_j(\vec{r}) \tag{2.9}$$

where $T_s[\rho]$ is the kinetic energy of a system of non-interacting electrons with density ρ. J[ρ] is the classical coulombic interaction,

$$J[\rho] = \frac{1}{2}\int\int \frac{\rho(\vec{r})\rho(\vec{r'})}{|\vec{r}-\vec{r'}|}d\vec{r}\vec{r'} \tag{2.10}$$

and E_{xc} is the exchange-correlation functional. The last term is the coulombic interaction between the electrons and the nuclei.

This approach leads to Kohn-Sham equation[45, 60]

$$\left(-\frac{1}{2}\nabla^2 + \upsilon(\vec{r}) + \int \frac{\rho(\vec{r'})}{|\vec{r}-\vec{r'}|}d\vec{r'} + \upsilon_{xc}(\vec{r})\right)\psi_i(\vec{r}) = \varepsilon_i\psi_i(\vec{r}) \tag{2.11}$$

where the exchange-correlation potential,υ_{xc}, is given by the functional derivative[60]

$$\upsilon_{xc} = \frac{\delta E_{xc}[\rho]}{\delta\rho(\vec{r})} \tag{2.12}$$

E_{xc} includes the difference in kinetic energies between the system of independent electrons with density ρ and the actual interacting system with the same density. Since this difference is generally expected to be small[59], E_{xc} primarily accounts for a correction to $J[\rho]$ arising from electron correlations. The exact form of exchange-correlation functional is unknown, but it can be approximated as a local or nearly local functional of the electron density.

There are two well-known approximations for the exchange-correlation function: the local density approximation (LDA)[37] and the generalized-gradient approximation (GGA)[37, 63, 28]. Although several different parameterizations of the GGA functionals exist, two of the most widely used are the Perdew-Wang functional (PW91)[64], and the Perdew-Burke-Ernzerhof functional (PBE)[62]. In this thesis, all DFT calculation used the generalized-gradient approximation as parameterized by PBE.

2.1.2 Pseudopotential Method

Many numerical techniques for solving the Kohn-Sham equations exist. However, among them, the Linear Augmented Plane Wave (LAPW)[70] method and the pseudopotential[60, 65] method have proven to be most reliable. The LAPW method is more accurate among the two, but is computationally more expensive. The pseudopotential method based on the projector augmented wave (PAW)[12] method is fast and relatively accurate compared to the LAPW method.

The pseudopotential method with PAW approach replaces the effect of the core electrons around the ions that do not participate in bonding with a smoother pseudo-wave function. This provides a way to calculate all-electron properties along with smooth parts of the valence functions. As results, the PAW approach has the advantage in both computational efficiency and reliability.

All first-principles electronic structure calculations in this thesis were performed using the PAW approach implemented in the Vienna *ab initio* simulation package (VASP).[40, 38, 39]

2.2 Cluster expansion

2.2.1 Role of cluster expansion

Statistical mechanics serves as a bridge between the atomic-scale analysis and their macroscale thermodynamics. According to statistical mechanics, macroscopic properties are based on the weighted averages of all possible microstates. Therefore, the relative frequency of a solid being in a specific microstate σ determines the relative importance of the microstates in calculating the thermodynamic averages, and it is given at constant temperature T, volume V, and number of atoms N :

$$P_\sigma = \frac{exp(-E_\sigma/\kappa_B T)}{Q} \tag{2.13}$$

where κ_B is the Boltzman's constant and Q is the partition function. The partition function is a normalization factor and defined as:

$$Q = \sum_\sigma exp(-E_\sigma/\kappa_B T) \tag{2.14}$$

Thus, average thermodynamic properties can be evaluated as:

$$G = \sum_{\sigma} G_{\sigma} P_{\sigma} \tag{2.15}$$

Furthermore, the free energy G is related to the partition function according to the equation: [48]

$$G = -\kappa_B \; T \; lnQ \tag{2.16}$$

The free energy G is Gibbs free energy in canonical ensemble (constant T, V, and N). The Gibbs free energy is an important quantity to predict phase stability of different phases at finite temperatures. To accurately evaluate the free energy, it is required to know E_{σ} for all possible different excited states upon electronic, vibrational, and configurational excitations.

Therefore, we need a model that accurately describes the functional relationship between the energy and the associated degrees of freedom for all the microstates. For this thesis, the configurational excitation is the most important factor to understand thermodynamic properties. Hence, using cluster expansion, we represent the energy as a function of linear combination of configurational excitations.

2.2.2 Construct formalism

A cluster expansion describes the dependence of the energy of a multi-component crystal on the degree of ordering among its constituents. The evolution of the displacement reaction of Li with Cu_2Sb can be tracked in a ternary composition space spanned by Li, Cu and Sb. Several intermediate phases are stoichiometric compounds, while others form solid solutions over a limited concentration interval. All the phases that form during the displacement reaction maintain the fcc Sb sublattice, differing only in the arrangement and composition of Li and Cu over the interstitial tetrahedral

and octahedral sites of fcc Sb. Thus, We will use Li-Cu_2Sb system as an example to explain construction of ternary cluster expansion formalism.

We found it convenient to use Li_3Sb, in which Li fills all octahedral and tetrahedral sites of an fcc Sb sublattice, as a reference configuration for the cluster expansion. Other compounds in the Li-Cu-Sb ternary having an fcc Sb sublattice can be obtained from Li_3Sb by replacing a subset of Li with vacancies and Cu. A particular ordering of vacancies and Cu over the Li sites of Li_3Sb can be specified with the help of occupation variables assigned to each site. To this end, we introduce two occupation variables at each Li site i of Li_3Sb: p_i^{Va}, which is equal to 1 if site i is occupied by a vacancy and zero otherwise and p_i^{Cu}, which is 1 if the site is occupied by Cu and zero otherwise. If both occupation variables at a particular site i are zero, the site is occupied by Li. The collection of all occupation variables $\vec{p} = \{p_0^{Cu}, p_0^{Va}, ..., p_i^{Cu}, p_i^{Va}, ..., p_M^{Cu}, p_M^{Va}\}$ uniquely specifies the ordering of Li, Cu and vacancies over the M interstitial sites of Sb. The dependence of the fully relaxed energy of the crystal on degree of order can be written as an expansion in terms of polynomials of occupation variables according to [67, 20]

$$E\left(\vec{p}\right) = E_0 + \sum_{\alpha} E_{\alpha}^{\vec{D}} \cdot \Lambda_{\alpha}^{\vec{D}}\left(\vec{p}\right), \tag{2.17}$$

where E_0 and $E_{\alpha}^{\vec{D}}$ are expansion coefficients and $\Lambda_{\alpha}^{\vec{D}}$ are basis functions defined as

$$\Lambda_{\alpha}^{\vec{D}}\left(\vec{p}\right) = \prod_{j \in \alpha} p_j^{D(i)}. \tag{2.18}$$

where the index j runs over the sites of a cluster α and $\vec{D} = \{D(j)\}$ labels the type of occupation variable at each site j (i.e. p_i^{Va} or p_i^{Cu}). The symmetry of the crystal imposes constraints on the expansion coefficients by requiring that all symmetrically equivalent cluster basis functions, $\Lambda_{\alpha}^{\vec{D}}$, have the same expansion coefficient $E_{\alpha}^{\vec{D}}$. The

cluster expansion is only practical if it can be truncated beyond a maximal cluster size.

The coefficients of a truncated cluster expansion, $E_\alpha^{\vec{D}}$, were determined by fitting to a training set of first-principles total energies. We used a genetic algorithm to determine the optimal basis functions to be included in a truncated cluster expansion[13].

We used the CASM software package[83, 82] to construct the cluster expansions and parameterize their coefficients for first-principles total energy calculations.

2.3 Grand Canonical Monte Carlo simulations

Monte Carlo simulation is one of well known tools used in statistical mechanics.[1] The cluster expansion allows to estimate the formation energy of any imaginary configuration in a large supercell expeditely and accurately, while Monte Carlo simulations average the thermodynamic quantities according to a transition probability.

In this study, Grand canonical Monte Carlo (MC) simulations based on the Metropolis algorithm were applied to the cluster expansions to calculate thermodynamic properties at room temperature. Averages of the grand canonical energy, defined for each configuration as

$$\Omega(\vec{p}, \mu_{Li}, \mu_{Cu}) = E(\vec{p}) - N_{Li}\mu_{Li} - N_{Cu}\mu_{Cu} \tag{2.19}$$

as well as averages of the equilibrium number of Li, N_{Li}, and Cu, N_{Cu}, were calculated as a function of temperature, T, and chemical potentials μ_{Li} and μ_{Cu}. These quantities were used to calculate the Gibbs free energy as a function of Li and Cu concentration at room temperature, using standard free energy integration techniques

[77, 88].

$$\Omega(T_f, \mu_{Li_f}, \mu_{Cu_f}) = \frac{\beta_{T_i}\Omega(T_i, \mu_{Li_i}, \mu_{Cu_i}) + \int_{\beta_{T_i}}^{\beta_{T_f}} (E(\vec{p}) - \mu_{Li}N_{Li} - \mu_{Cu}N_{Cu})d\beta}{\beta_{T_f}} - \int_{\mu_{Li_i}}^{\mu_{Li_f}} N_{Li}d\mu_{Li} - \int_{\mu_{Cu_f}}^{\mu_{Cu_i}} N_{Cu}d\mu_{Cu} \quad (2.20)$$

where $\beta_{T_i} = 1/(\kappa_B \mathrm{T})$. The Gibbs free energy (G) defined as:

$$G(T, \mu_{Li}, \mu_{Cu}) = \Omega(T_f, \mu_{Li_f}, \mu_{Cu_f}) + N_{Li}\mu_{Li} + N_{Cu}\mu_{Cu} \quad (2.21)$$

The Gibbs free energies were then used to calculate a ternary phase diagram in the Li-Cu-Sb composition space and other derived thermodynamic properties including the open circuit voltage profile of the conversion reaction, which is linearly related to the Li chemical potential [90, 78].

CHAPTER III

Elucidating the origins of path hysteresis during electrochemical cycling of Li-Sb electrodes

3.1 Introduction

Li can react directly with another element such as Si, Sn, Al and Sb, which undergo alloying reactions. Unlike intercalation reactions, the reaction of Li with Si and Sn, for example, can yield compounds with very high Li concentrations (i.e. $Li_{3.75}Si$ and $Li_{4.4}Sn$) making capacities as high as 3579 $mAhg^{-1}$and 993 $mAhg^{-1}$theoretically possible.[26, 16, 54] However, as discussed on Section I, these materials exhibit a large hysteresis due to large volume changes and complex phase transformations during cycling.

Here, we focuss on the Sb electrode to shed light on the cause of hysteresis in electrodes of Li-ion batteries undergoing alloying reactions. Although Sb has a smaller specific capacity of 660 $mAhg^{-1}$than Si and Sn, it undergoes smaller volume changes and fewer phase transformations upon reaction with Li. The electrochemical reaction of Li with Sb electrodes is also accompanied by path hysteresis with the discharge voltage profile qualitatively differing in shape from the charge profile. Lithium insertion into Sb electrodes leads first to the formation of Li_2Sb having hexagonal symmetry followed by the formation of Li_3Sb having cubic symmetry.[58, 29] Upon

Li removal, however, Li_3Sb transforms directly to Sb, bypassing the intermediate hexagonal Li_2Sb phase.[58, 29] Hence, the discharge voltage curve has two plateaus separated by a small step at the Li_2Sb composition, while the charge profile has a single plateau, which is usually about 0.2-0.3 V above the discharge plateaus. The hysteresis persists even at low charge and discharge rates. In spite of this path hysteresis, the charge and discharge profiles as well as the capacity does not change much over many cycles[6] in contrast to bulk Si and Sn electrodes, which can show large irreversible capacity losses.[26, 57]

With the aim of elucidating the origin of the path hysteresis exhibited by the alloying reaction of Li with Sb, we perform first-principles calculations to establish a range of crystallographic, electronic, thermodynamic and kinetic properties of the three phases that form during the electrochemical reaction of Li with Sb. Based on these property predictions we argue that path hysteresis in Sb electrodes arises from an asymmetry in the competition between Li diffusion rates and driving forces for nucleation. These triggers are likely common to many other electrode chemistries that suffer from path hysteresis.

3.2 Method

First-principles electronic structure calculations were performed using density functional theory (DFT) within the generalized gradient approximation as parameterized by Perdew-Burke-Ernzerhof (PBE).[62] We used the Vienna Ab initio simulation package (VASP) plane wave pseudo-potential code[38, 39] with the projector augmented wave method (PAW) to describe the interactions between valence and core electrons.[40, 12] An energy cutoff of 400 eV was used. We used a Γ-point centered $12\times12\times12$ k-point mesh for the primitive cell of Li_3Sb, a $6\times6\times6$ k-point mesh for the unit cell of Li_2Sb and a $12\times12\times4$ mesh for the unit cell of Sb. The k-point meshes for supercell of these structures were chosen to yield a similar k-point density

in reciprocal space. Ionic positions and the lattice parameters of each structure were fully relaxed.

To study off stoichiometry at room temperature (as opposed to 0 K), we also performed a statistical mechanical study of the thermodynamic properties using cluster expansion Hamiltonians and Monte Carlo simulations. We used the CASM software package[83, 82] to construct the cluster expansions and parameterize their coefficients to first-principles total energy calculations as well as to perform Monte Carlo simulations.

Lithium migration mechanisms and barriers were determined using the climbing image nudged-elastic-band method,[27] as implemented in VASP. For each phase, a large supercell was used, allowing all atoms to relax while holding the lattice parameters and volume of the supercell fixed.

To calculate electronic densities of state and band structure of A7 Sb, hexagonal Li_2Sb and cubic Li_3Sb we used the HSE06 hybrid functional.[41]

3.3 Results

3.3.1 Crystallography

There are three distinct phases that can coexist when Li alloys with Sb. The first is pure Sb, prototype A7, which belongs to space group $R\bar{3}m$ (No.166).[68] Its crystal structure is shown in Fig. 3.1a and consists of puckered layers. The second phase is hexagonal Li_2Sb belonging to space group $P\bar{6}2c$ (No.190)[52] and is shown in Fig. 3.1b. The last phase is Li_3Sb which has cubic symmetry and belongs to space group $Fm\bar{3}m$ (No.225).[68, 15] Since A7 Sb, hexagonal Li_2Sb and cubic Li_3Sb are distinct phases that can tolerate some degree of off-stoichiometry, we will refer to them with the Greek letters α, β and γ respectively.

α-Sb, β-Li_2Sb and γ-Li_3Sb can each be described as the stacking of either trian-

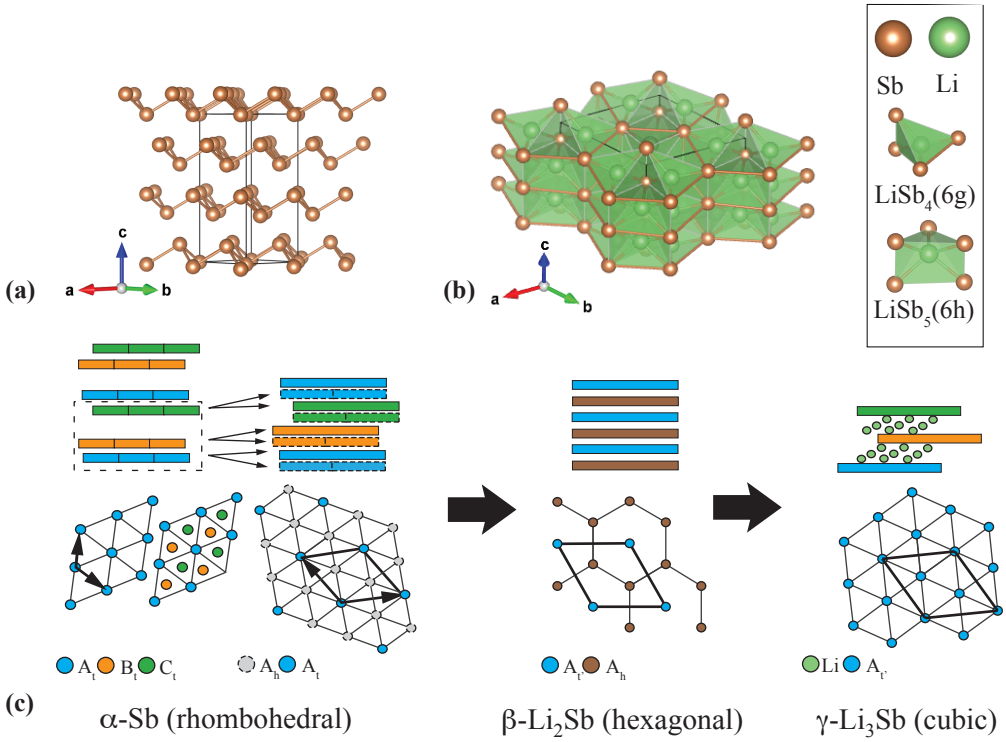

Figure 3.1: Crystal structures of (a) pure α-Sb ($R\bar{3}m$, prototype A7) and (b) hexagonal β-Li_2Sb ($P\bar{6}2c$). (c) Schematic illustrations of structural transformations from α-Sb to β-Li_2Sb and from β-Li_2Sb to γ-Li_3Sb. A_t,B_t, and C_t represent triangular lattices and A_h represents a honeycomb network. $A_{t'}$ represents a triangular lattice rotated by 30 degrees.

gular Sb layers or a combination of triangular and honeycomb Sb layers. Following convention, we denote stacking sequences of triangular layers with the letters A, B and C. To emphasize that these layers are triangular lattices, we add a subscript t such that the stacking in fcc, for example, would be denoted by $A_tB_tC_t$. There are also several ways of stacking a honeycomb network, which can also be denoted by the letters A, B and C. For a honeycomb layer, we add the subscript h. In describing the crystallographic relationships between α-Sb, β-Li_2Sb and γ-Li_3Sb, we will also need to distinguish between layers that have been rotated by 30 degrees around an axis perpendicular to the layer. We label these layers with a prime, e.g. $A_{t'}$.

The crystal structure of pure α-Sb is similar to the fcc lattice except that every other close-packed (111) layer is off-centered. Fig. 3.1c illustrates the α-Sb crystal structure as represented by layers of triangular lattices. The triangular lattices have an $A_tB_tC_t$ stacking sequence as in fcc, but with non-uniform spacing between pairs of planes. The off-centering of alternating layers allows the Sb of one close-packed plane to form three short bonds with neighboring Sb of the other close-packed plane (Fig. 3.1a).

The crystal structure of hexagonal β-Li_2Sb is also layered in the sense that the Sb sublattice can be described as consisting of two-dimensional honeycomb layers, A_h, interleaved by two-dimensional triangular lattices, $A_{t'}$. The Sb-Sb nearest neighbor distance within the $A_{t'}$ layers of β-Li_2Sb is substantially larger than that in the triangular layers of pure Sb as they reside above and below the centers of the honeycomb rings of the adjacent A_h layers. The Sb sublattice is identical to the omega phase of elemental metals such as Ti and Zr and their suboxides.[30, 76] The Li ions occupy two symmetrically distinct interstitial sites within this Sb sublattice. The first is a five-fold coordinated square pyramidal site (6h Wyckoff position), while the second is a four fold coordinated tetrahedral site (6g Wyckoff position).

The Sb sublattice of γ-Li_3Sb forms a perfect fcc lattice, which is a stacking of

close-packed triangular lattices, i.e. $A_tB_tC_t$. The Li ions occupy all the octahedral and tetrahedral interstitial sites of the fcc Sb sublattice.

Although several crystallographic pathways linking α-Sb to the Sb sublattice of the β-Li_2Sb phase can be identified, one is especially straightforward. It relies on the splitting of each triangular lattice of Sb into a honeycomb layer and a new triangular lattice that is rotated by 30 degrees and has a much larger nearest neighbor distance between Sb. An A_t layer of pure α-Sb, for example, can split into a A_h honeycomb layer and a $A_{t'}$ layer, as illustrated in Fig. 3.1c. The Sb atoms of A_t that ultimately form the $A_{t'}$ triangular lattice form a $\sqrt{3} \times \sqrt{3}$ supercell in the original A_t layer. If every triangular layer splits in this manner, an intermediate crystal is formed with $A_hA_{t'}B_hB_{t'}C_hC_{t'}$ stacking, as illustrated in Fig. 3.1c. This intermediate crystal must be sheared to obtain the $A_hA_{t'}A_hA_{t'}A_hA_{t'}$ of the Sb sub lattice in β-Li_2Sb, as shown in Fig. 3.1c.

A similar mechanism connects the Sb sublattice of β-Li_2Sb with that of γ-Li_3Sb. The collapse of a honeycomb network A_h with a triangular lattice $A_{t'}$ forms a triangular lattice A_t. The collapse of pairs of A_h and $A_{t'}$ must also be accompanied by a shear to take the resulting $A_tA_tA_t$ stacking to an fcc $A_tB_tC_t$ stacking characterizing the Sb sublattice of γ-Li_3Sb.

In view of the crystallographic similarities between the three phases, the possibility exists that the two-phase reactions between any pair of them could occur coherently. An important metric to analyze this possibility is the transformation strain required to deform one crystal into the other. If the transformation strain is small, the two-phase reaction may proceed coherently without incurring large coherency strain energy penalties. The transformation strain can be defined using the starting phase as the reference. The Green-Lagrange strain tensor, E, is related to

the deformation gradient $\hat{F}$ according to

$$E = \frac{\hat{F}^{+}\hat{F} - I}{2} \tag{3.1}$$

where, for homogeneous strain, the 3×3 deformation gradient matrix $\hat{F}$ relates the lattice vectors of the transformed crystal $\mathbf{a}'$, $\mathbf{b}'$ and $\mathbf{c}'$ to the lattice vectors of the original crystal $\mathbf{a}$, $\mathbf{b}$ and $\mathbf{c}$ according to $\mathbf{a}' = \hat{F}\mathbf{a}$. $\hat{F}^{+}$ corresponds to the transpose of $\hat{F}$.

In general, large misfit strains between the original crystal structure and the new crystal structure will incur large strain energy costs when the two phases coexist coherently. If this strain energy is larger than the cost of forming an incoherent interface, the transformation will occur reconstructively. As is to be expected for alloying reactions, the volume changes in the Li-Sb system are very large. Transforming from α-Sb to β-Li_2Sb results in a volume change of close to 90%, while the addition of Li to β-Li_2Sb to form γ-Li_3Sb results in a further increase of about 35% relative to the Sb volume. Large volume changes by themselves, though, do not necessarily result in strain energy penalties. There are special anisotropic transformation strains in which particular crystallographic planes do not undergo a strain as the original crystal transforms into the new crystal. The transformation can then proceed coherently in the absence of coherency strains if the interface separating the growing phase from the original phase within an electrode particle is parallel to these strain invariant planes. The requirement for the existence of a strain invariant plane is that one eigenvalue of E is equal to 0, one eigenvalue is greater than 0 and one eigenvalue is less than 0.[34]

The eigenvalues of the transformation strains (Eq. 3.1), assuming the crystallographic transformation paths described above and using experimentally measured lattice parameters[68, 52], are listed in Table 3.1. The transformation strains are very large as is clear by the large eigenvalues. However, they all show at least one

Transformation path	λ_1	λ_2	λ_3
α-Sb $\rightarrow$ β-Li_2Sb	-0.0416	0.0669	1.3652
α-Sb $\rightarrow$ γ-Li_3Sb	-0.1031	0.0817	2.4883
β-Li_2Sb $\rightarrow$ γ-Li_3Sb	-0.2224	0.0130	0.7493
β-Li_2Sb $\rightarrow$ α-Sb	-0.3660	-0.0590	0.0453
γ-Li_3Sb $\rightarrow$ β-Li_2Sb	-0.2999	-0.0127	0.4007
γ-Li_3Sb $\rightarrow$ α-Sb	-0.4163	-0.0702	0.1299

Table 3.1: The eigenvalues of the transformation strains for various crystallographic transformation paths using experimentally measured lattice parameters

positive and one negative eigenvalue as well as an eigenvalue close to zero. Nevertheless, the eigenvalues close to zero are still sizable and thus none of the transformation strains exhibit a strict strain invariant plane. If any of these transformations occur coherently, they will be accompanied by coherency strain. We point out though that the transformations that most closely approach the conditions for a strain invariant plane are between Li_2Sb and Li_3Sb.

3.3.2 Electronic structure

The electrodes of an electrochemical cell should exhibit some degree of electronic conductivity such that electrons can reach the electrode/electrolyte interface where the electrochemical reactions occur. We used both DFT-PBE as well as HSE06 [41] to calculate the electronic density of states and band structure of α-Sb, β-Li_2Sb and γ-Li_3Sb. The density of states and band structure as calculated with HSE06 are shown in Fig. 3.2. Both α-Sb and γ-Li_3Sb are predicted to be semi-conductors having band gaps of approximately 0.05 and 1.1 eV respectively. β-Li_2Sb is predicted to be metallic, but with the Fermi level close to a minimum in the density of states.

Lithium removal from γ-Li_3Sb lowers the Fermi level into the valence band resulting in the creation of holes. The density of states rises sharply when decreasing the Fermi level away from the valence band maximum. This suggests that the holes, created upon Li removal, will likely form itinerant states that are mobile, very quickly making γ-$Li_{3-y}Sb$ electronically conducting. The band gap of α-Sb is predicted to

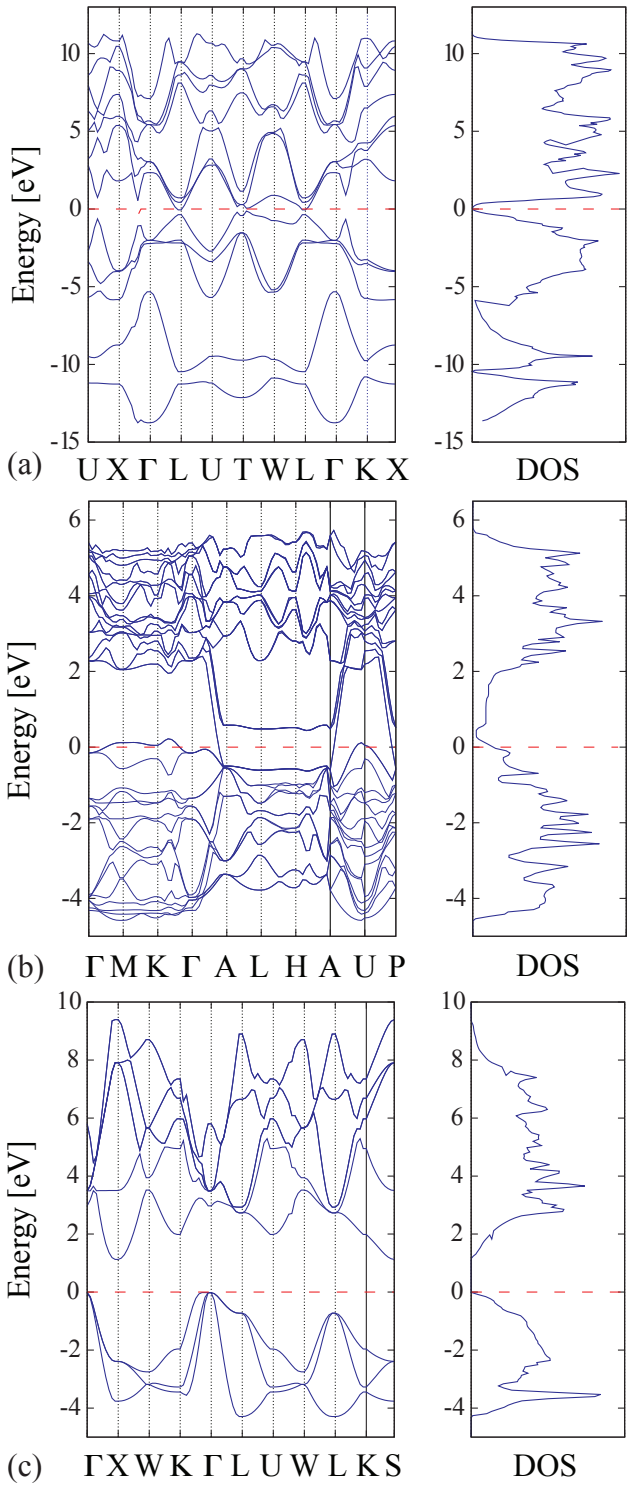

Figure 3.2: Calculated electronic density of states and band structures of (a) α-Sb (rhombohedral unit cell), (b) β-Li_2Sb (hexagonal unitcell), and (c) γ-Li_3Sb using the HSE screened hybrid functional. The Fermi level is set to zero.

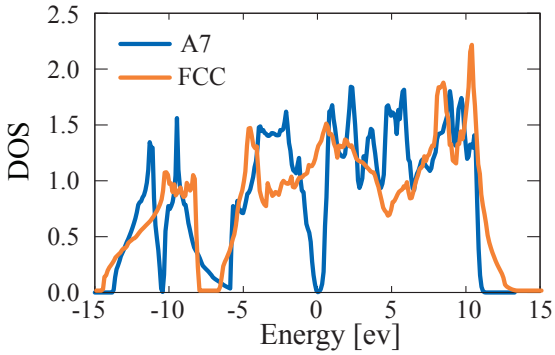

Figure 3.3: Density of states of the A7 form of α-Sb (blue) and the perfect fcc form of Sb (orange). The A7 form of α-Sb is similar to the fcc lattice with the exception that every other close-packed(111) layer is off-centered.

be very small. As described above, the A7 form of α-Sb can be derived from perfect fcc Sb by reducing the distance between alternating pairs of close packed planes, thereby lowering the symmetry of the crystal and doubling the size of the primitive unit cell. Perfect fcc Sb is predicted with HSE06 not to have a band gap. The band gap emerges as alternating pairs of (111) planes are shifted off center to form the A7 crystal structure (Fig. 3.3). The addition of interstitial Li to the Sb host should shift the Fermi level into the conduction band. Again, the density of states increases very rapidly when moving into the conduction band, suggesting that electrons donated by inserted Li are likely to be delocalized and itinerant due to the strong dispersion of the conduction bands.

3.3.3 Thermodynamic properties

An electrode material that undergoes path hysteresis will pass through metastable states for at least some portion of the charge and discharge process. While α-Sb, β-Li_2Sb and γ-Li_3Sb are line compounds their crystal structures suggest that they can tolerate some degree of off-stoichiometry, either by introducing interstitial Li in α-Sb, or by creating Li vacancies in β-Li_2Sb and γ-Li_3Sb. To determine the accessibility of these metastable off-stoichiometric compositions, we calculated the free energies of dilute α-Sb, β-Li_2Sb and γ-Li_3Sb using a cluster expansion approach.

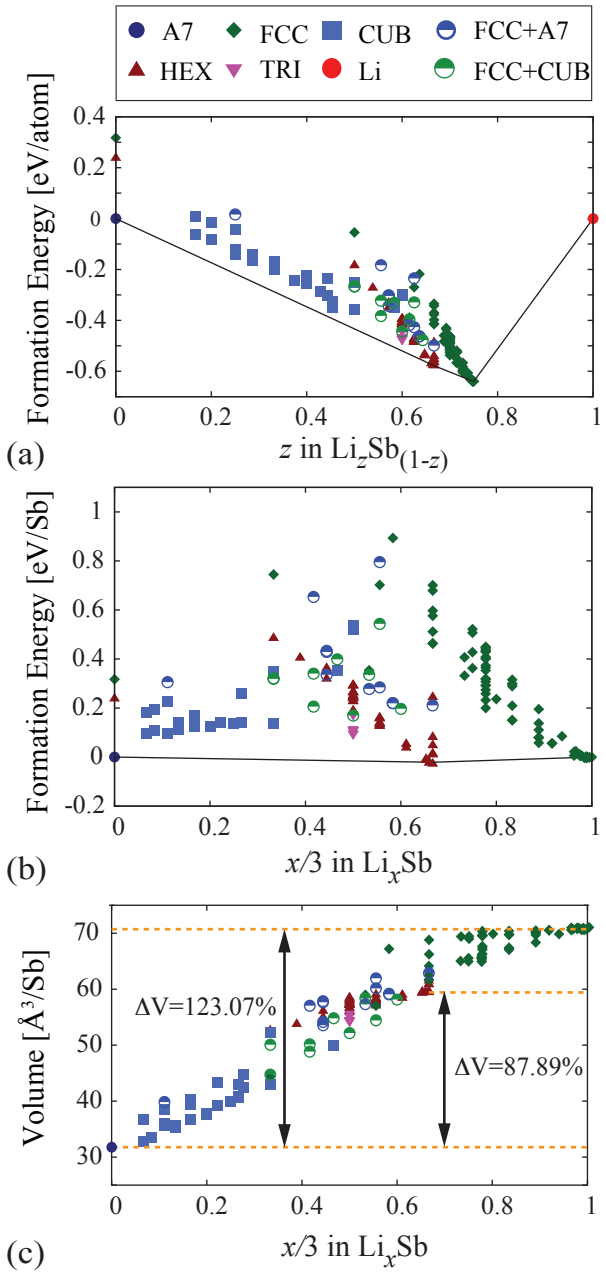

Figure 3.4: Formation energies of different configurations calculated from first-principles (a) per atom using α-Sb and pure Li as a reference (b) per Sb using γ-Li_3Sb and α-Sb as a reference. The energies of the ground states are connected with a black line forming a convex hull. (c) Volume per Sb for all calculated structures between α-Sb and γ-Li_3Sb. The changes in the volume of the ground state phases is shown with a dotted orange line.

Throughout the remainder of the text, we will work with different composition variables depending on the context. In some contexts it is convenient to track the number of Li, N_{Li}, normalized by the number of Sb, N_{Sb}, a quantity we will denote with $x = N_{Li}/N_{Sb}$. This composition variable appears in the chemical formula Li_xSb. In other contexts, it is convenient to work with an atomic fraction, which we define as $z = N_{Li}/(N_{Li} + N_{Sb})$. In terms of z, the chemical formula of the alloy is then $Li_zSb_{(1-z)}$. We will also denote off-stoichiometric forms of α-Sb, β-Li_2Sb and γ-Li_3Sb as $Li_\delta Sb$, $Li_{2-\epsilon}Sb$ and $Li_{3-\zeta}Sb$ respectively, where δ refers to a dilute Li concentration and ϵ and ζ refer to dilute vacancy concentrations (all normalized by the number of Sb).

As a first step in parameterizing cluster expansion Hamiltonians for each compound, we enumerated symmetrically distinct Li-vacancy orderings over the interstitial sites of α-Sb and over the Li sites of hexagonal $Li_{2-\epsilon}Sb$ and cubic $Li_{3-\zeta}Sb$. The Li-vacancy orderings were enumerated within symmetrically distinct supercells of the primitive unit cells of the parent compounds. We calculated the total energies of these configurations with DFT-PBE as implemented in VASP. Fig. 3.4a shows the resulting formation energies, defined as

$$\Delta E(z) = E(z) - zE_{Li} - (1-z)E_{Sb} \tag{3.2}$$

where, $E(z)$ is the DFT energy of a particular configuration in a supercell having an atomic fraction z. The energy $E(z)$ is normalized by the total number of atoms within that supercell $(N_{Li} + N_{Sb})$. E_{Li} and E_{Sb} are DFT energies per atom of bcc Li and α-Sb respectively.

Fig. 3.4a shows that hexagonal β-Li_2Sb, and cubic γ-Li_3Sb are predicted to be stable intermediate compounds in the Li-Sb binary. Interestingly, configurations having very dilute vacancy concentrations over the octahedral sites of γ-$Li_{3-\zeta}Sb$ are also predicted to reside on the convex hull (e.g. $Li_{2.96}$ and $Li_{2.98}Sb$). Moreover, a large

number of configurations with dilute concentrations of lithium vacancies in hexagonal β-Li_2Sb and cubic γ-Li_3Sb have formation energies close to the convex hull.

Fig. 3.4b shows formation energies calculated relative to α-Sb and γ-Li_3Sb and plotted versus Li concentration $x/3$. The energies of each structure in this plot are normalized by the number of Sb atoms. This figure more clearly illustrates the stability of the different metastable structures relative to the three ground states α-Sb, β-Li_2Sb and γ-Li_3Sb. The volumes of the different structures are also shown in Fig. 3.4c as a function of $x/3$.

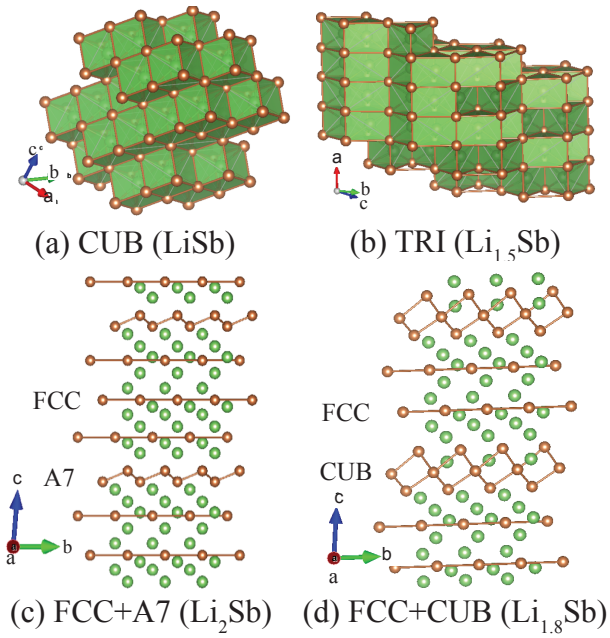

Figure 3.5: Examples of relaxed metastable structures upon creation of large vacancy concentrations in hexagonal β-Li_2Sb and cubic γ-Li_3Sb or upon insertion of small lithium concentrations in α-Sb.

The introduction of large vacancy concentrations in β-Li_2Sb and γ-Li_3Sb often causes the original structure to relax to very different final structures. We have been able to distinguish between several categories of crystal structures that emerge when relaxing β-Li_2Sb and γ-Li_3Sb upon removal of Li. The energies of these structures are denoted by different symbols in Fig. 3.4. The green diamonds (FCC) correspond to energies of structures in which the Sb sublattice of $Li_{3-\zeta}Sb$ maintains its fcc sub-

lattice as in stoichiometric cubic Li_3Sb. The dark red triangles (HEX) correspond to structures in which the Sb sublattice is that of stoichiometric Li_2Sb. Addition of Li to Sb starting in the A7 crystal structure, even at very dilute Li concentrations, causes the Sb sublattice to adopt a cubic network, as illustrated in Fig. 3.5a. The energies of these structures are denoted with blue squares (CUB) in Fig. 3.4. The pink triangles (TRI) having stoichiometry $Li_{1.5}Sb$ in Fig. 3.4 consist of close-packed triangular Sb sublattices having an $A_tA_tA_t$ stacking sequence (as illustrated in Fig. 3.5b). The Li occupy a subset of the trigonal prismatic interstitial sites within the Sb sublattice. For Li compositions between LiSb and Li_2Sb, a variety of hybrid structures emerge as shown in Fig. 3.5c and 3.5d. The half-blue circles (FCC+A7) in Fig. 3.4 correspond to the energies of layered structures that have several close packed triangular Sb layers as in fcc interleaved by a puckered Sb layer as in the A7 crystal structure of pure Sb (Fig. 3.5c). The half-green circles (FCC+CUB) correspond to energies of structures that are also layered, but have Sb triangular lattices interleaved by a layer made up of cubes of Sb as in the cubic structures of dilute Li_xSb (Fig. 3.5d).

The formation energies of configurations having low vacancy concentrations within hexagonal β-Li_2Sb and cubic γ-Li_3Sb were used to parameterize the expansion coefficients of cluster expansion Hamiltonians [67, 20]. Separate cluster expansions were constructed for hexagonal β-$Li_{2-\epsilon}Sb$ and cubic γ-$Li_{3-\zeta}Sb$. In parameterizing a cluster expansion for cubic γ-$Li_{3-\zeta}Sb$, only configurations that maintained the fcc Sb sublattice after relaxation (FCC in Fig. 3.4) were used, while in the parameterization of the cluster expansion for the hexagonal phase only configurations that maintained the Sb sublattice of β-Li_2Sb (HEX in Fig. 3.4) were used. The cluster expansions were subjected to grand canonical Monte Carlo simulations to predict the dependence of the Li chemical potential on Li concentration within each compound. This dependence was then integrated to calculate the Gibbs free energy, g (normalized by the total number of atoms) as a function of concentration z. The calculated free energies are

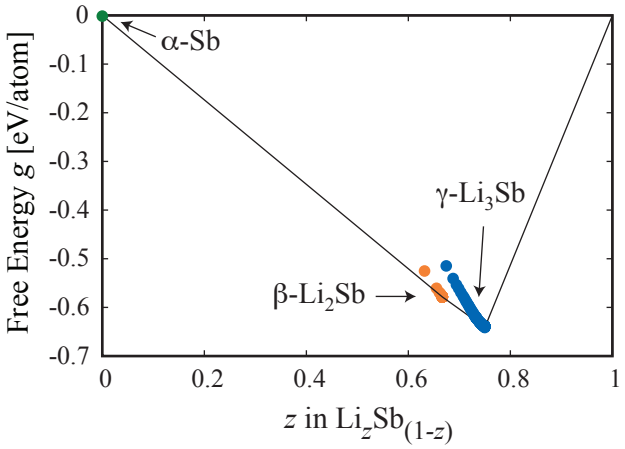

Figure 3.6: The calculated free energies of β-$Li_{2-\epsilon}Sb$ and γ-$Li_{3-\zeta}Sb$ at 300 K plotted as a function of atomic fraction z in Li_zSb_{1-z}.

shown in Fig. 3.6 [19].

The voltage of an electrochemical cell using metallic Li as the anode is related to the Li chemical potentials according to

$$V(z) = -(\mu_{Li}(z) - \mu^o_{Li})/e \tag{3.3}$$

where, $\mu_{Li}(z)$ is the Li chemical potential in Li_zSb_{1-z} and μ^o_{Li} is the Li chemical potential of metallic Li. The chemical potentials in Eq. 3.3 are in units of eV and e corresponds to the charge of an electron.

Fig. 3.7 shows the calculated equilibrium voltage curve as a function of Li concentration. A small step at the composition of β-Li_2Sb (z=0.66) separates two plateaus corresponding to two-phase reactions between α-Sb and β-Li_2Sb and between β-Li_2Sb and γ-Li_3Sb respectively. The step height is approximately 40 mV. Fig. 3.7 also shows metastable voltage profiles for β-$Li_{2-\epsilon}Sb$ and γ-$Li_{3-\zeta}Sb$. Cubic γ-$Li_{3-\zeta}Sb$ can reach high vacancy concentrations ($\zeta \sim 0.5$) with a 0.2V overpotential relative to the equilibrium γ-Li_3Sb to β-Li_2Sb voltage plateau.

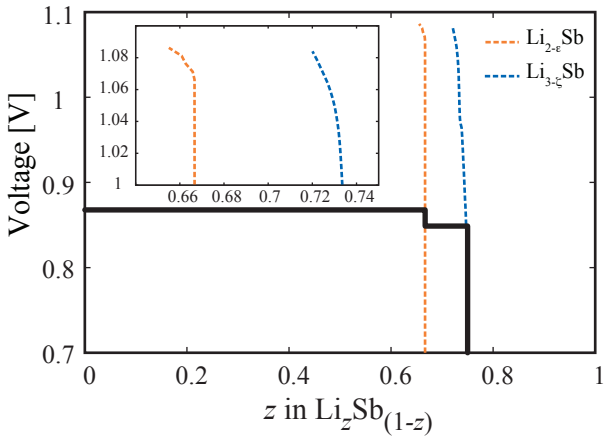

Figure 3.7: Equilibrium voltage profile (solid black line) and metastable voltage profiles for $Li_{2-\epsilon}Sb$ (orange dashed line) and $Li_{3-\zeta}Sb$ (blue dashed line).

3.3.4 Kinetic properties

Li diffusion within the three stable compounds is an important property as it determines the rates with which the electrode can be charged and discharged and is likely to play a role in the selection of kinetic pathways. A key quantity in assessing the mobility of Li ions is the migration barrier of individual hops. Diffusion in most electrode materials for Li-ion batteries occurs at non-dilute concentrations and can be quite complex due to the dependence of migration barriers and hop mechanisms on the local concentration and the varying degrees of disorder among lithium and vacancies.[78] A treatment of non-dilute diffusion requires kinetic Monte Carlo approaches combined with cluster expansion techniques, for example, to describe the dependence of atomic hop barriers on the local degree of Li-vacancy ordering.[80, 83, 10, 11] Since α-Sb, hexagonal β-$Li_{2-\epsilon}Sb$ and cubic γ-$Li_{3-\zeta}Sb$ are essentially line compounds, we need only consider diffusion in the presence of dilute concentrations of mediating defects such as Li interstitials or Li vacancies. The diffusion coefficient in these dilute limits is directly proportional to individual atomic hop frequencies[78], which can be approximated with transition state theory.[85]

In α-Sb, the relevant diffusion process is the migration of an isolated interstitial Li

from one site to an adjacent interstitial site, while in hexagonal β-$Li_{2-\epsilon}Sb$ and cubic γ-$Li_{3-\zeta}Sb$ atomic diffusion is mediated through the migration of isolated vacancies and possibly divacancies between adjacent sites of the Li sublattices of the compounds. Using the nudged elastic band method as implemented in VASP, we calculated the migration barriers for elementary hops in α-Sb, β-Li_2Sb and γ-Li_3Sb.

For nudged elastic band calculations of isolated interstitial Li hops in α-Sb, we used a 3×3×2 supercell of the hexagonal unit cell of A7 Sb, while for Li hops into isolated vacancies in β-Li_2Sb we used a 2×2×2 supercell of the hexagonal unit cell. Nudged elastic band calculations for Li hops into isolated vacancies and divacancies in cubic γ-Li_3Sb were performed with a 3×3×3 supercell of the primitive cell of cubic Li_3Sb.

At dilute Li concentrations, individual Li ions can occupy two distinct interstitial sites in A7 Sb: an eightfold coordinated site (3b), and a compressed octahedral site (3a). The eightfold 3b site is more stable than the compressed octahedral 3a site by ∼200 meV. Li can hop between adjacent sites, either by performing a curved hop by passing through an intermediate tetrahedral site or by following a direct hop as illustrated in Fig. 3.8b and 3.8d. The calculated migration barriers shown in Fig. 3.8a and 3.8c, are high when compared to typical Li migration barriers in electrode materials for Li-ion batteries.[80] The connectivity of these hops forms a three-dimensional network, such that Li diffusion will be three dimensional.

There are two symmetrically distinct Li sites in hexagonal Li_2Sb, a tetrahedral site (6g) and a square pyramidal site (6h). An isolated vacancy prefers to reside in the 6g tetrahedral site. The energy increases by ∼40 meV when the vacancy moves from the tetrahedral site to the 6h square pyramidal site. Fig. 3.9a shows the energy as a Li ion migrates from the square pyramidal site to a neighboring vacant tetrahedral site. Li can also hop between neighboring tetrahedral sites parallel to the **c** axis and the energy for this hop is shown in Fig. 3.9c. The migration barriers for both

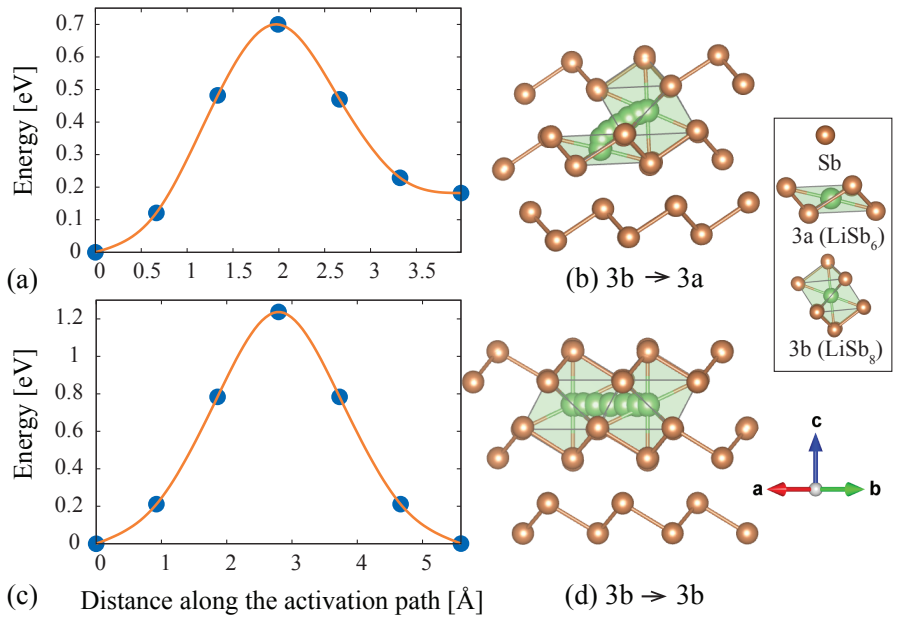

Figure 3.8: Migration barriers and paths for Li hops in α-Sb at dilute Li concentrations. (a) Barrier and (b) hop path for a Li hop from an eightfold coordinated site to an adjacent compressed octahedral site. (c) Barrier and (d) hop path for a Li hop in a basal plane from an eightfold coordinated site to an adjacent eightfold coordinated site.

hops are of the order of 200-250 meV. Hops between neighboring tetrahedral sites or neighboring square pyramidal sites parallel to the basal plane of the hexagonal unit cell are also possible, however, the barriers for these hops are of the order of 1 eV and are therefore unlikely to contribute much to macroscopic Li diffusion. The collection of the symmetrically equivalent nearest neighbor hops with low barriers forms a three dimensional network. The Li ions of cubic Li_3Sb fill both the tetrahedral and octahedral interstitial sites of the fcc Sb sublattice. An isolated vacancy prefers to reside on the octahedral site. The energy of the crystal increases by 100 meV when the vacancy moves from the octahedral site to the tetrahedral site. The energy along the migration path as a Li atom hops from a tetrahedral site to an octahedral site is shown in Fig. 3.10a. The energy barrier is less than 150 meV, a very small value. A similar migration barrier was recently predicted by Baggetto et al [6] for Li_3Sb. The calculated free energy for γ-$Li_{3-\zeta}Sb$ shown in Fig. 4.5 suggests that Li_3Sb can tolerate

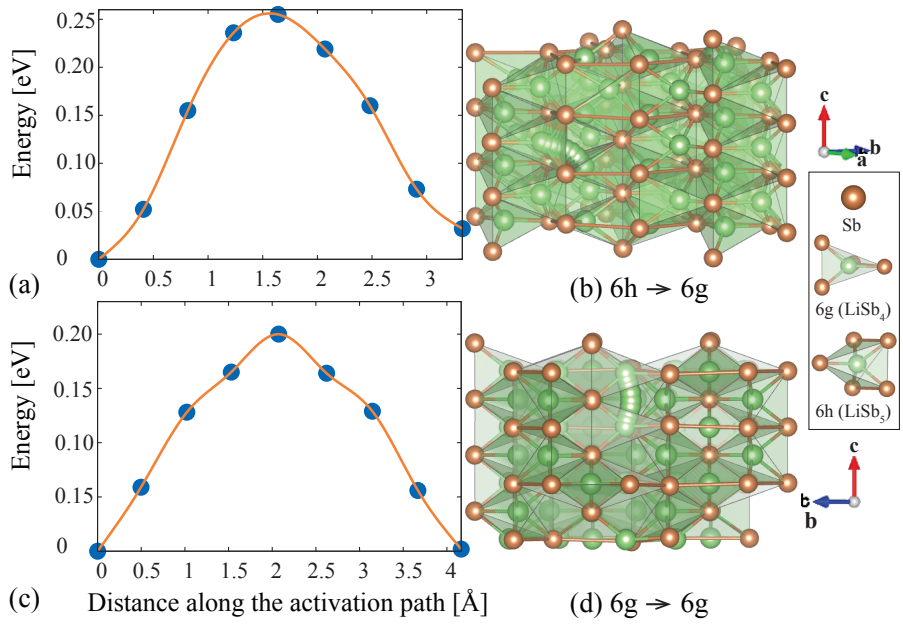

Figure 3.9: Migration barriers and paths for Li hops in hexagonal β-Li_2Sb. (a) Barrier and (b) hop path for a Li hop from a square pyramidal site to an adjacent vacant tetrahedral site. (c) Barrier and (d) hop path for a Li hop between neighboring tetrahedral sites parallel to the **c** axis.

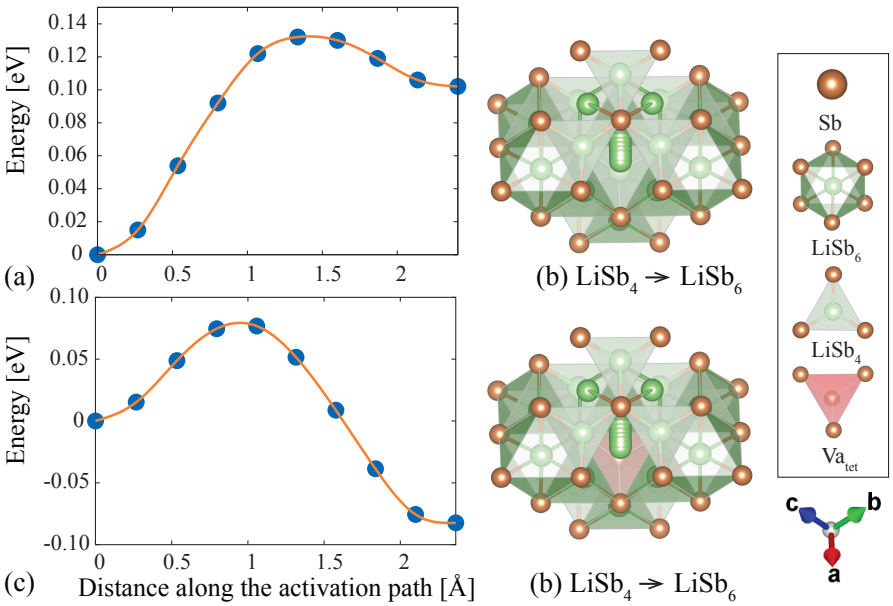

Figure 3.10: Migration barriers and paths for Li hops in cubic γ-Li_3Sb having an fcc Sb sublattice. (a) Barrier and (b) hop path for Li hop from a tetrahedral site to adjacent vacant octahedral site. (c) Barrier and (d) hop path for a Li hop from a tetrahedral site into a vacant octahedral site next to a vacant tetrahedral site (Li hops into a divacancy).

off stoichiometry and that vacancy clusters may be prominent [78]. We therefore also considered Li hops into a divacancy. Fig. 3.10c shows the energy as a Li hops from a tetrahedral site into a vacant octahedral site next to a vacant tetrahedral site. While isolated vacancies in Li_3Sb prefer to reside on octahedral sites, when an octahedral vacancy is next to a tetrahedral vacancy, the energy of the crystal actually decreases when a tetrahedral Li hops into the octahedral site, thereby forming two tetrahedral vacancies. The barrier for this hop, as for the single vacancy hop, is again very low and of the order of 150 meV.

3.4 Discussion

Although the charge and discharge of Sb electrodes appears facile and stable over many cycles, it nevertheless exhibits path hysteresis.[58, 29] The discharge voltage profile (i.e. during Li insertion) has two plateaus with a small step corresponding to the formation of Li_2Sb, while the charge voltage profile (Li extraction) has a single plateau between Li_3Sb and Sb. The voltage interval in which Li_2Sb is stable relative to Sb and Li_3Sb is very small ($\sim$ 0.04V as predicted from first principles) and may not appear as a sharp step in experimental discharge voltage profiles. Nevertheless, there is a consistent difference of $\sim$ 0.2-0.3 V between charge and discharge with *in situ* XRD indicating the formation of Li_2Sb upon discharge, but its absence during charge.[29]

The occurrence of a phase transformation requires some degree of supersaturation, or in electrochemical terms an overpotential relative to the equilibrium potential of two-phase coexistence. It is only then that thermodynamic driving forces for transformation exist. A thermodynamic driving force is defined as a difference between the free energy of the stable phase and the metastable (supersaturated) phase. The

grand canonical free energy defined as

$$\phi = \tilde{g} - \mu_{Li} x \tag{3.4}$$

is the relevant thermodynamic potential when electrochemically controlling the Li chemical potential through the cell voltage (see Eq. 3.3). In Eq. 3.4, $\tilde{g}$ is the Gibbs free energy normalized by the number of Sb, N_{Sb}. Figure 3.11 shows the calculated grand canonical free energies of α-Sb, β-Li_2Sb and γ-Li_3Sb as a function of voltage. Thermodynamic equilibrium at constant voltage (or equivalently at constant μ_{Li}) is determined by the phase with the lowest grand canonical free energy ϕ. Chemical potentials (or voltages) where grand canonical free energies of different phases cross correspond to equilibrium phase transition voltages. It is at these voltages that a plateau emerges in the voltage profile due to a discontinuous change in concentration when going from one phase to the next. As is clear in Figure 3.11, high voltages (above 0.87 V) stabilize α-Sb, while low voltages below 0.83 stabilize γ-Li_3Sb. The β-Li_2Sb phase is only stable in a narrow voltage window of ~ 0.04 eV. It can be shown that the slopes of the grand canonical free energies in Figure 3.11 are proportional to the Li concentration x. Since β-Li_2Sb and γ-Li_3Sb have similar Li concentrations, their grand canonical free energy curves, ϕ^β and ϕ^γ, have similar slopes.

The similarities in the slopes of ϕ^β and ϕ^γ as a function of voltage leads to a strong asymmetry in driving forces when transforming from α-Sb to β-Li_2Sb during discharge versus transforming from γ-Li_3Sb to β-Li_2Sb upon charge. During discharge of an Sb electrode, an underpotential (polarization), ΔV, relative to the equilibrium α-Sb $\rightarrow$ β-Li_2Sb voltage of ~ 0.87 V is required to create a driving force, $\Delta\phi^{\alpha\rightarrow\beta} = \phi^\beta - \phi^\alpha$, for the transformation. As is evident in Figure 3.11, this driving force very rapidly becomes large with increasing underpotential ΔV. While a driving force for a α-Sb to γ-Li_3Sb, $\Delta\phi^{\alpha\rightarrow\gamma}$, also emerges with an underpotential, it is approximately as

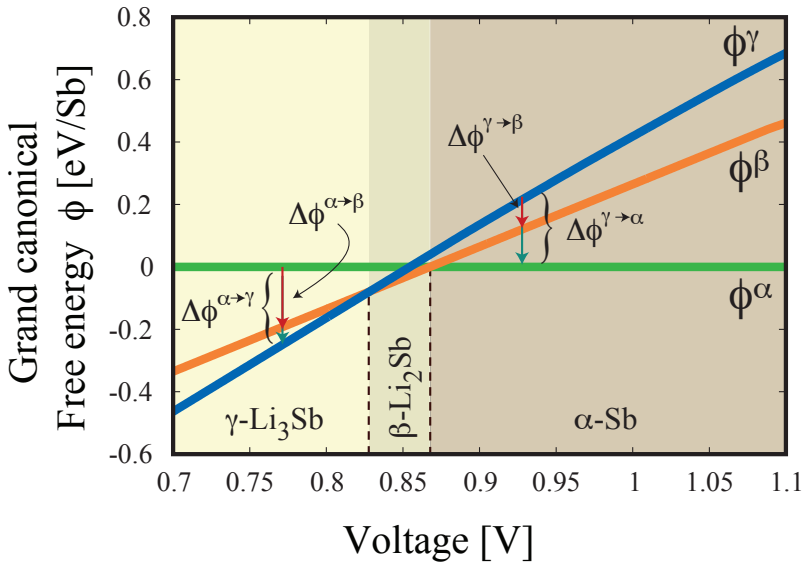

Figure 3.11: Grand Canonical Free Energies ϕ for α-Sb, β-Li_2Sb and γ-Li_3Sb as a function of voltage. The grand canonical free energies are normalized by the number of Sb in each phase.

large as $\Delta\phi^{\alpha\to\beta}$. In the opposite direction, when charging γ-Li_3Sb by increasing the voltage above the equilibrium γ - β transition voltage of 0.83 V, the driving force to form β-Li_2Sb, $\Delta\phi^{\gamma\to\beta}$, does not increase markedly with over potential since ϕ^{γ} and ϕ^{β} have similar slopes and run almost parallel to each other. Instead, for overpotentials ΔV larger than $\sim$ 0.02 eV, the driving force for the formation of α-Sb directly from γ-Li_3Sb, $\Delta\phi^{\gamma\to\alpha}$, emerges and very quickly becomes substantially larger than $\Delta\phi^{\gamma\to\beta}$. Figure 3.11 illustrates a general principle that the driving forces for transformation between phases having similar Li concentrations increases less rapidly with over (under) potential than that between phases having very different concentrations, when controlling the Li chemical potential electrochemically.

The asymmetry is further amplified when considering driving forces for nucleation. Nucleation driving forces and barriers play a key role in phase selection during a phase transformation. The driving force for nucleation are more conveniently represented in Gibbs free energy versus atomic fraction, z, diagrams as schematically illustrated in Figure 3.12. The Li chemical potential of a particular phase, α for example,

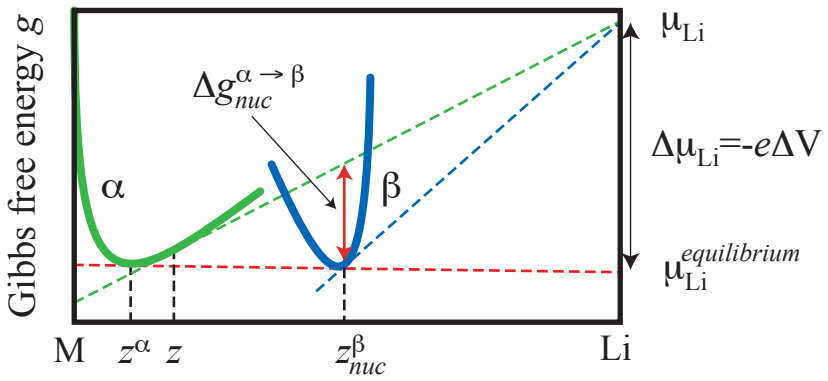

Figure 3.12: Schematic illustration of the driving force for the nucleation of a new phase (β) in a supersaturated phase (α).

corresponds to the intercept of the tangent to the free energy of α with the z=1 axis. A driving force for nucleation of a new phase β within a preexisting phase α can only emerge if α is supersaturated with respect to its equilibrium solubility limit z^{α} determined by the common tangent to the free energies of α and β as shown schematically in Fig. 3.12. A supersaturation in Li concentration ($z > z^{\alpha}$) results in an overpotential $\Delta\mu_{Li}$ relative to the equilibrium Li chemical potential, $\mu_{Li}^{equilibrium}$, of the $\alpha - \beta$ two-phase coexistence. The overpotential $\Delta\mu_{Li}$ can be represented graphically in a free energy versus concentration plot as illustrated in Fig. 3.12. According to Eq. 3.3, this overpotential in Li chemical potential is equal to -$e\Delta V$, where ΔV is an underpotential in voltage. As shown in Fig. 3.12, the driving force for the nucleation of a new phase, β, in a supersaturated phase, α, is equal to the distance between the free energy of β evaluated at the composition of nucleation, z_{nuc}^{β}, and the tangent to the free energy of the supersaturated α phase.[8]. While there are no a priori constraints on the concentration of the nucleus, z_{nuc}^{β}, here we will assume that the new phase nucleates at the same Li chemical potential as that of the parent phase. This is illustrated graphically in Fig. 3.12.

Fig. 3.13a graphically shows the nucleation driving forces for β-Li_2Sb and γ-Li_3Sb in a supersaturated α-Sb phase when an underpotential of 0.1V relative to the equi-

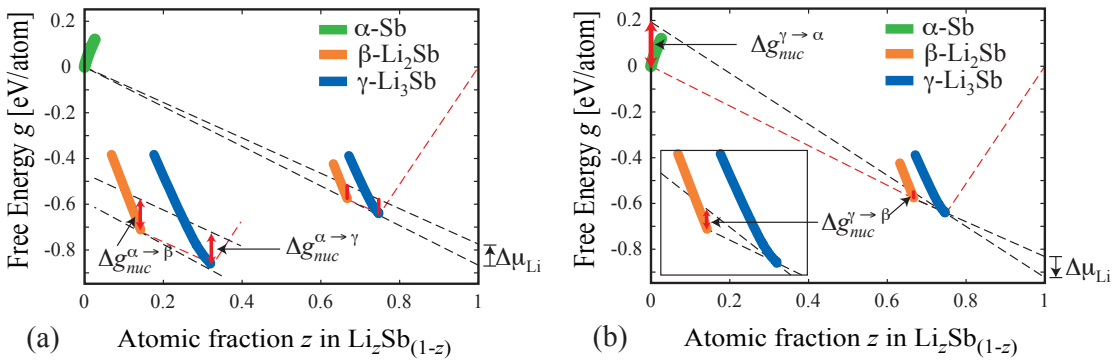

Figure 3.13: (a) The nucleation driving forces for β-Li_2Sb and γ-Li_3Sb in a supersaturated α-Sb phase when an overpotential of 0.1V relative to the equilibrium voltage plateau for the α-Sb to β-Li_2Sb reaction is imposed. (b) The nucleation driving forces for β-Li_2Sb and α-Sb in a supersaturated γ-Li_3Sb phase when an overpotential of 0.1V to extract Li from γ-Li_3Sb is imposed relative to the equilibrium voltage of the γ-Li_3Sb to β-Li_2Sb reaction.

librium voltage plateau for the α-Sb to β-Li_2Sb reaction is imposed. As is clear from Fig. 3.13a, the driving forces $\Delta g_{nuc}^{\alpha\to\beta}$ and $\Delta g_{nuc}^{\alpha\to\gamma}$ to nucleate β-Li_2Sb and γ-Li_3Sb from a supersaturated α-Sb phase upon Li insertion are very similar. Fig. 3.13b shows the nucleation driving forces for β-Li_2Sb and α-Sb, $\Delta g_{nuc}^{\gamma\to\beta}$ and $\Delta g_{nuc}^{\gamma\to\alpha}$, when an overpotential of 0.1V to extract Li from γ-Li_3Sb is imposed relative to the equilibrium voltage of the γ-Li_3Sb to β-Li_2Sb reaction. In this case, the $\Delta g_{nuc}^{\gamma\to\alpha}$ is substantially larger than $\Delta g_{nuc}^{\gamma\to\beta}$. The much larger difference in concentration between α-Sb and γ-Li_3Sb compared to that between β-Li_2Sb and γ-Li_3Sb results in a lever effect that significantly enhances the nucleation driving force for α-Sb relative to that for β-Li_2Sb.

The lever effect becomes more apparent when the driving force for nucleation is plotted as a function of over (under) potential. Fig. 3.14a shows the nucleation driving force for β-Li_2Sb and γ-Li_3Sb when an overpotential to insert Li is applied to α-Sb. Since the concentrations of Li_2Sb and Li_3Sb are very close to each other, the nucleation driving forces for both phases are almost identical in value, especially

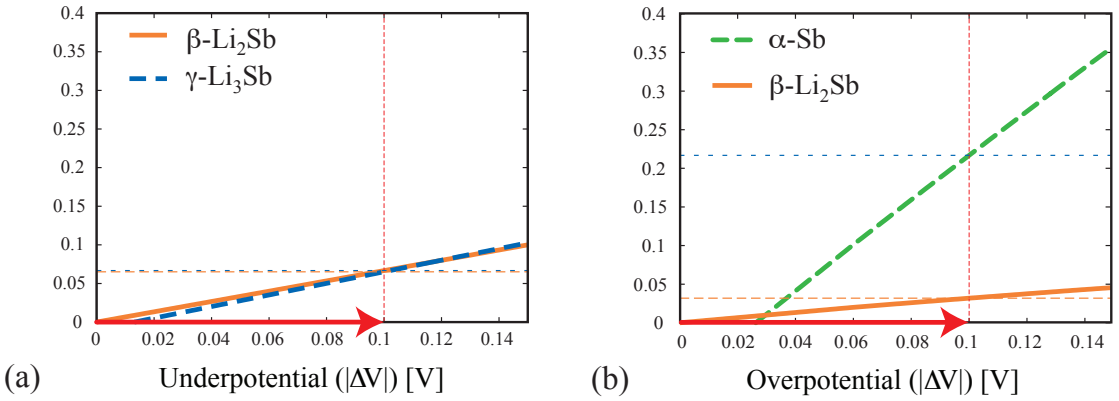

Figure 3.14: The nucleation driving forces as a function of overpotential. (a) The nucleation driving force for β-Li_2Sb and γ-Li_3Sb when an overpotential to insert Li is applied to α-Sb. (b) The nucleation driving forces for β-Li_2Sb and α-Sb when an overpotential to extract Li from γ-Li_3Sb is applied.

for large over potentials. Consistent with this, weak Li_3Sb resonances are observed even in the $Li_{0.75}Sb$ sample (i.e., during the Sb-Li_2Sb process). The situation is very different when applying an overpotential to extract Li from γ-Li_3Sb, as shown in Fig. 3.14b. The driving force for the nucleation of α-Sb exceeds that of β-Li_2Sb already at overpotentials as small as 0.03 eV. The insertion of Li into α-Sb, therefore, results in comparable driving forces for β-Li_2Sb and γ-Li_3Sb at all but the smallest overpotentials while the extraction of Li from γ-Li_3Sb very quickly produces much larger driving forces for the nucleation of α-Sb than for β-Li_2Sb.

The thermodynamic and kinetic properties calculated in this work suggest that much higher overpotentials are accessible in γ-Li_3Sb than in α-Sb. Li is remarkably mobile in γ-Li_3Sb, with migration barriers predicted between 0.1 to 0.13 eV. These migration barriers are lower even than those encountered in intercalation compounds.[80, 83, 10, 11] Furthermore, the calculated free energy of off-stoichiometric γ-Li_3Sb indicates that this phase can very easily tolerate a high concentration of vacancies. The metastable part of the calculated voltage profile of γ-Li_3Sb (Fig. 3.7) shows that

overpotentials of ~ 0.2 are easily achievable through the introduction of Li vacancies. Li can therefore be extracted very rapidly from γ-Li_3Sb and in large numbers, resulting in high overpotentials. The predicted Li mobility at dilute concentrations within the A7 crystal structure of Sb, in contrast, is very low, with migration barriers around 0.7 eV and above. Reaching large underpotentials due to the insertion of Li in excess of the solubility limit of α-Sb (with respect to β-Li_2Sb formation) will not occur rapidly as a result of sluggish Li mobility.

As with path hysteresis in $CuTi_2S_4$, a model displacement reaction analyzed using a first-principles multi-scale approach[90], path hysteresis in the Li-Sb alloying reaction arises from a very high Li diffusion coefficient in the fully lithiated phase. The kinetic ease of extracting Li from the fully lithiated phase renders a metastable path kinetically more accessible than the true equilibrium path. The lever effect on the nucleation driving forces then likely leads to the nucleation of α-Sb rather than the thermodynamically more stable intermediate β-Li_2Sb phase. In the Li-Sb system, path hysteresis upon charge (i.e. Li extraction) should be avoidable if Li extraction occurs sufficiently slowly in a voltage window where a driving force to nucleate β-Li_2Sb exists but where a similar driving force to nucleate α-Sb is not present. Nevertheless, path hysteresis may be difficult to suppress using realistic charge rates, since β-Li_2Sb is thermodynamically stable in only a very small voltage window and the Li mobility in Li_3Sb is exceptionally high.

3.5 Conclusion

The aim of this work was to identify the origins of phase transformation hysteresis during the electrochemical cycling of Sb electrodes in Li-ion batteries. The phases that form during the electrochemical reaction of Li with Sb electrodes (α-Sb, β-Li_2Sb and γ-Li_3Sb) are crystallographically very similar. While β-Li_2Sb and γ-Li_3Sb are line compounds in the Li-Sb phase diagram, our first-principles statistical mechanical

analysis suggests that they can tolerate high concentrations of Li vacancies without incurring a large free energy penalty. Calculations of Li migration barriers predict that Li has a very low mobility in α-Sb, having to overcome migration barriers of the order of 0.7 eV. Li is, however, predicted to be remarkably mobile in γ-Li_3Sb and β-Li_2Sb with migration barriers between 0.15 and 0.25 eV. Mobility is seen experimentally for non-stoichiometric γ-Li_3Sb. An analysis of nucleation driving forces reveals a large lever effect upon Li removal from γ-Li_3Sb, with the nucleation driving force for α-Sb exceeding that for β-Li_2Sb already at small overpotentials. This, together with a very high Li mobility in γ-Li_3Sb, which facilitates large overpotentials, provides an explanation for the phase transformation hysteresis observed when cycling Sb electrodes. Non-stoichiometry of the alloy phases coupled with rapid Li transport can play a critical role in controlling the structural pathways taken by electrode materials on charge.

The triggers of phase transformation hysteresis identified here for the Li-Sb alloying reaction are likely also prevalent in intercalation compounds and other alloying reactions that suffer from path hysteresis. While high cation mobilities are usually desirable, especially when the equilibrium path passes through a solid solution, it may lead to path hysteresis when phase transformations must also occur that are kinetically more sluggish than metastable Li insertion/extraction through diffusion. The overpotentials that arise when the electrode passes through a metastable solid solution can then lead to thermodynamic driving forces to transform to phases having a larger change in Li concentration than intermediate phases along the equilibrium path. This will be more likely in systems where intermediate phases are only stable in a narrow voltage window, as is the case for Li_2Sb in the Li-Sb system. These principles suggest that the suppression of path hysteresis requires a balance among all competing kinetic processes during Li insertion and removal, especially between the rates of Li diffusion and phase transformations.

CHAPTER IV

Elucidate the intrinsic properties of Li-Cu_2Sb electrode that facilitate reversibility and minimize hysteresis

4.1 Introduction

Displacement and conversion reactions are another possible alternative reaction mechanisms to achieve a high capacity in which the insertion of the shuttled ion is coupled with the displacement or extrusion of a transition metal from the electrochemically active compound. As discussed in Section I, in contrast to intercalation materials, displacement and conversion reactions are able to react with many electrons per transitional metal. They utilize the full charge state M_{x^+} of the metal ion within the electrode material reducing it to the M^0 charge state as the metal precipitates out upon discharge.[66, 74] This can result in very high capacities. Indeed, materials that undergo conversion and displacement reactions, such MF_x (M = Fe or Cu)[86, 5], M_xO_y (M= Ru, Co, Ni, Cu, or Fe)[66, 31], MgH_2[55], and $Cu_{2.33}V_4O_{11}$[50] have a much higher capacity compared to the best intercalation compounds currently commercialized. For example, the theoretical capacity of FeF_2, which is a positive conversion electrode material, and RuO_2, which is an negative conversion electrode material, are 571mAhg^{-1}and 1130mAhg^{-1}respectively,[86, 7] while, the theoretical

capacity of graphite, which is a negative commercialized-insertion-material, is 372 $mAhg^{-1}$. [17, 75, 53, 44, 72, 73]

The kinetics of displacement and conversion reactions is substantially more complex than intercalation processes and remains poorly understood. While exhibiting very high capacities, compounds that undergo displacement and conversion reactions suffer from a variety of limitations that need to be overcome. These include a poor reversibility and large capacity losses during charge and discharge. As a consequence, almost all electrode compounds that rely on a displacement or conversion reaction exhibit an unacceptably large hysteresis in the voltage profile between charge and discharge.

One exception to this trend is Cu_2Sb, a candidate anode material that undergoes a displacement reaction with Li, but exhibits only a limited degree of hysteresis in the voltage profile between charge and discharge. The electrochemical reaction of Cu_2Sb with Li results in a sequence of intermediate compounds with varying concentrations of Li and Cu, but with strong structural similarities to the original compound.[24] Although Li insertion causes large variations in lattice parameters, it does not produce compounds that have a different Sb back bone. Sb within Cu_2Sb forms a face centered cubic (fcc) sublattice, which is preserved as lithium enters the compound and simultaneously displaces Cu. In this sense, the reaction of Li with Cu_2Sb can be viewed as a displacement reaction, although the large variations in volume may result in kinetic processes that are similar to conversion reactions where the original compound is completely replaced with new compounds in a reconstructive manner.

Here we perform a comprehensive first-principles study of the thermodynamic properties associated with the Cu_2Sb+Li displacement reaction as well as a variety of kinetic properties related to Li and Cu diffusion. Our aim is to elucidate the intrinsic properties of the various reaction compounds that facilitate reversibility and minimize hysteresis between discharge and charge. A previous theoretical study of a model

displacement reaction that relied on first-principles thermodynamic and kinetic data and a phase field model to describe kinetics at the electrode particle level identified particular thermodynamic and kinetic properties intrinsic to the electrode chemistry and crystal structure that are responsible for the large hysteresis in displacement and conversion reactions. The study demonstrated that a primary source of hysteresis in these compounds arises from a difference in reaction path between charge and discharge. Phase field simulation of the displacement reaction identified the triggers that lead to the selection of a different reaction path between charge and discharge. These included (i) a large difference in the diffusion coefficients between Li and the displaced ion and (ii) a lack of a thermodynamic driving force for the reinsertion of the displaced ion upon removal of Li during charge along the discharge reaction path. Our focus here is to ascertain whether these conditions are satisfied in the reaction products of Cu_2Sb+Li.

4.2 Method

First principles energy were calculated within the generalized gradient approximation (GGA) to DFT as parameterized by Perdew-Burke-Ernzerhof (PBE).[62] We used the Vienna Ab initio simulation package (VASP) plane wave pseudo-potential code [38, 39] with the projector augmented wave method (PAW) to describe the interactions between valence and core electrons [40, 12]. The valence states of the various PAW pseudopotentials were: Li 1s, 2s, and 2p, Cu $3d^{10}$ and $4p^1$ and Sb $5s^2$ and $5p^3$. The plane-wave basis set cutoff energy was set to 400 eV, and a gamma point-centered k-point mesh with a density consistent with a 12x12x12 k-point mesh density in the primitive fcc cell reciprocal lattice was used for each structure. Ionic positions and lattice parameters of each structure were fully relaxed.

To study off stoichiometry at room temperature, we also construct the cluster expansions and perform Monte Carlo simulations. More details were discussed in

Section 2.2.2.

In addition to considering configurational degrees of freedom, we also studied the role of vibrational excitations on phase stability along the Cu-Sb binary to resolve apparent inconsistencies between zero Klevin DFT predictions and experimental observations. Vibrational free energies were calculated within the quasi-harmonic approximation, whereby the Helmholtz free energy due to harmonic phonon excitations, $F(V,T)$, was calculated at several increments of volume ranging from -5 % to $+5$ % of the zero Kelvin PBE predicted equilibrium volume. The minimum of $F(V,T)$ with respect to volume at each temperature T corresponds to the Gibbs free energy at zero pressure. Force constants were fit to forces calculated with PBE (using VASP) in large supercells in which different ions were perturbed relative to their equilibrium positions. Individual displacements were chosen based on high-symmetry directions within each supercells. Supercells containing 32, 32, and 18 primitive cells of Cu, Sb(A7), and Cu_2Sb, respectively were used to extract force constants. Resulting forces were incorporated into a least squares fit with the original atomic displacements to obtain force constants. Dynamical matrices were subsequently constructed using these force constants. The phonon density of states, composed of sampling the phonon frequencies in the Brillouin zone, was used to obtain $F^H(T,V)$ for each of the three phases.

4.3 Results

4.3.1 Thermodynamic Properties

The shape of the free energy surface as a function of concentration plays an important role in determining whether path hysteresis will be triggered during a displacement or conversion reaction [90]. We investigated the thermodynamic properties of the various phases that form during the lithiation of Cu_2Sb, first at zero Kelvin

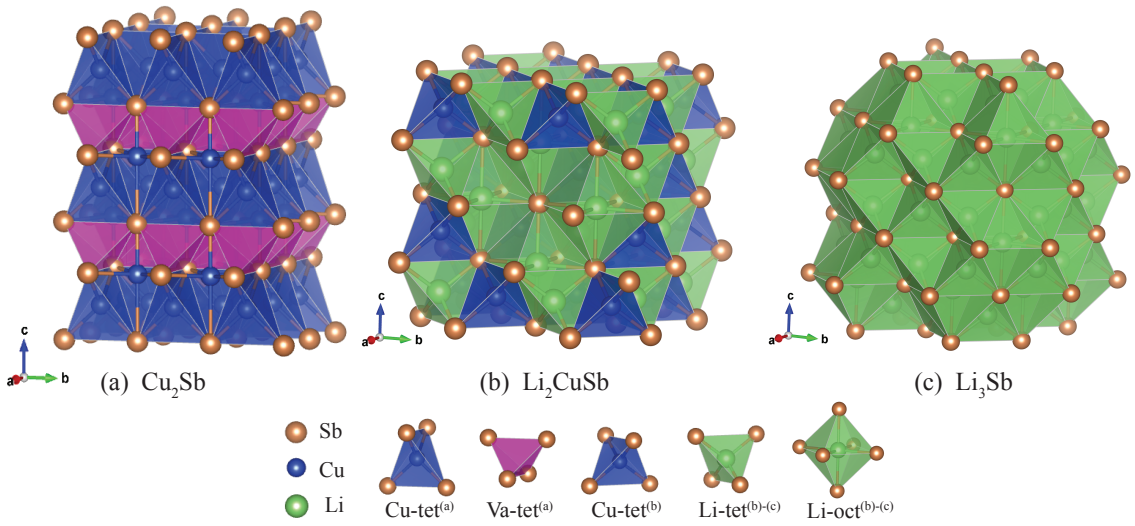

Figure 4.1: Crystal structures of (a) Cu_2Sb (P4/nmm)[61] (b) Li_2CuSb ($F\bar{4}3m$)[71] and (c) Li_3Sb ($Fm\bar{3}m$)[68, 15]

using DFT-PBE as implemented in VASP and subsequently at finite temperature by applying Monte Carlo simulations to a ternary cluster expansion parameterized with the DFT-PBE energies.

The Li-Cu-Sb ternary contains several stable compounds. Cu_2Sb has an fcc Sb sublattice and belongs to space group P/4nmm (No.129) [61]. Its crystal structure is shown in Figure 4.1a. One Cu per Cu_2Sb formula unit fills the octahedral interstitial sites while the other Cu orders over half of the tetrahedral interstitial sites of the fcc Sb sublattice. The Cu occupying tetrahedral sites segregate between alternating (001) planes of the fcc Sb sublattice, thereby giving the crystal a tetragonal symmetry. Electrochemical lithiation of Cu_2Sb results in the extrusion of Cu coupled with the formation of a ternary compound, having nominal stoichiometry Li_2CuSb with space group $F\bar{4}3m$ (No.216). The composition of Li_2CuSb is not well established, with evidence of an off-stoichiometric solid solution [71, 24, 47]. Li_2CuSb also has an fcc sublattice. The Cu orders over half the tetrahedral sites, however, the Cu ordering differs from that in Cu_2Sb, forming a zinc-blende ordering when considering only

the Cu and Sb sublattices. The Li ions of Li_2CuSb fill all the octahedral sites and remaining tetrahedral sites. Experimental and first-principles evidence suggests that Li_2CuSb has a tendency to tolerate Li vacancies over the Li-tetrahedral sites [71, 24, 47]. Further lithiation leads to additional Cu extrusion and the formation of Li_3Sb, which again has an fcc Sb sublattice with Li ions filling all interstitial tetrahedral and octahedral sites. The compound belongs to the $Fm\bar{3}m$ (No.225) space group [68, 15] and is shown in Figure 4.1c. In addition to Cu_2Sb, Li_2CuSb and Li_3Sb, a hexagonal Li_2Sb is also stable in the Li-Cu-Sb ternary. Li_2Sb, however, does not form during lithiation of Cu_2Sb or during subsequent Li removal from the Li_3Sb+Cu two-phase mixture. Li_2Sb is the only compound that does not have an fcc Sb sublattice. Instead the Sb sublattice is isomorphic to the omega phase of Zr [30, 76].

4.3.1.1 Zero Kelvin properties

In view of the uncertainty about the composition range in which the Li_2CuSb phase and the fact that all phases that form during lithiation of Cu_2Sb share a common fcc Sb sublattice, we enumerated 686 symmetrically distinct orderings of Li, Cu and vacancies over the tetrahedral and octahedral sites of fcc Sb. We calculated the total energies of theses configurations with DFT-PBE as implemented in VASP.

Figure 4.2 shows a zero Kelvin phase diagram in ternary composition space obtained by applying the common tangent construction to the formation energies, defined as

$$\Delta e(x,y) = e(x,y) - x \cdot e_{Li} - y \cdot e_{Cu} - (1-x-y) \cdot e_{Sb} \tag{4.1}$$

where x and y are the atomic fractions of Li and Cu respectively. The total energy $e(x,y)$ of a configuration was calculated with DFT-PBE and is normalized by the total number of atoms. The reference energies for the elemental components, e_{Li}, e_{Cu}

and e_{Sb}, were calculated in their room temperature stable crystal structures, which are bcc for Li, fcc for Cu and A7 for Sb. These energies are also normalized per atom.

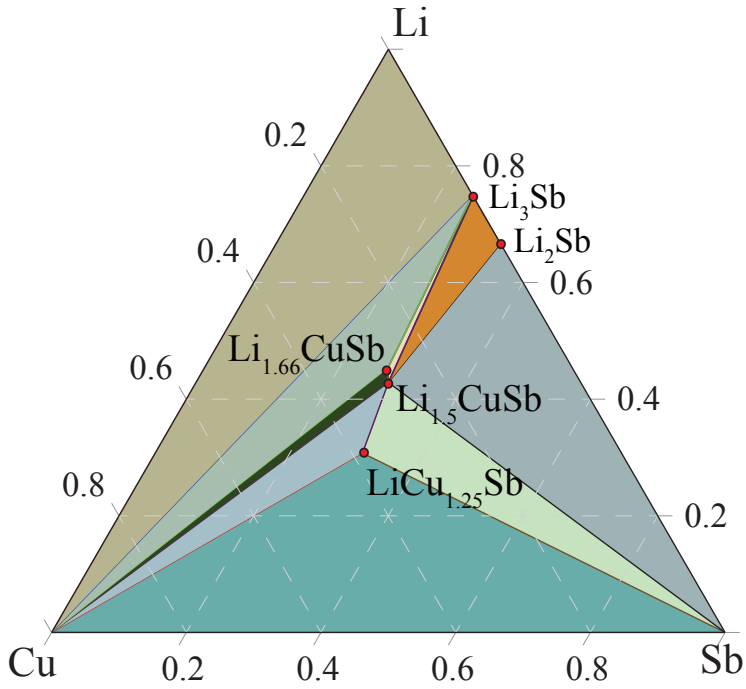

Figure 4.2: A projection of the convexhull in ternary composition space obtained by DFT calculations. The formation energies of different configurations calculated per atom using pure Li(bcc), Cu(fcc), and Sb(A7) as reference.

Each point in the phase diagram corresponds to the concentration of a stable ordered phase at 0 K. The lines connecting two points denote two-phase regions, while the triangles correspond to three-phase regions. Three ternary ordered phases are found to be stable: $LiCu_{1.25}Sb$, $Li_{1.5}CuSb$ and $Li_{1.66}CuSb$. All three compounds have Li occupying the octahedral sites and Cu filling half the tetrahedral sites ordered to form an fcc sublattice. The remaining tetrahedral sites are either filled by Cu and vacancies as in $LiCu_{1.25}Sb$, or by Li and vacancies as in $Li_{1.5}CuSb$ and $Li_{1.66}CuSb$ as can be seen in Figure 4.3. Many other orderings that are almost stable have similar Li, Cu and vacancy arrangements over the octahedral and tetrahedral sites. While there is a strong site preference for Li filling all the octahedral sites and for Cu filling

half of the tetrahedral sites, the resulting LiCuSb stoichiometry is not predicted to be a ground state. Additional Cu and(or) Li must be inserted to the remaining tetrahedral sites to form stable compounds. The strong site preference of Li and Cu atoms within LiCuSb was also predicted by Matsuno et al[46].

Several phases are predicted to be stable along the Li-Sb binary. These include the cubic Li_3Sb phase and the hexagonal Li_2Sb phase. We also found that the introduction of dilute vacancies to cubic Li_3Sb in large unit cells at compositions $Li_{2.96}Sb$ and $Li_{2.98}Sb$ leads to stable phases that reside on the convexhull. In contrast to the Li_xCu_ySb compounds, Li removal from Li_3Sb to form $Li_{2.96}Sb$ and $Li_{2.98}Sb$ occurs most easily by placing Li vacancies on the octahedral sites.

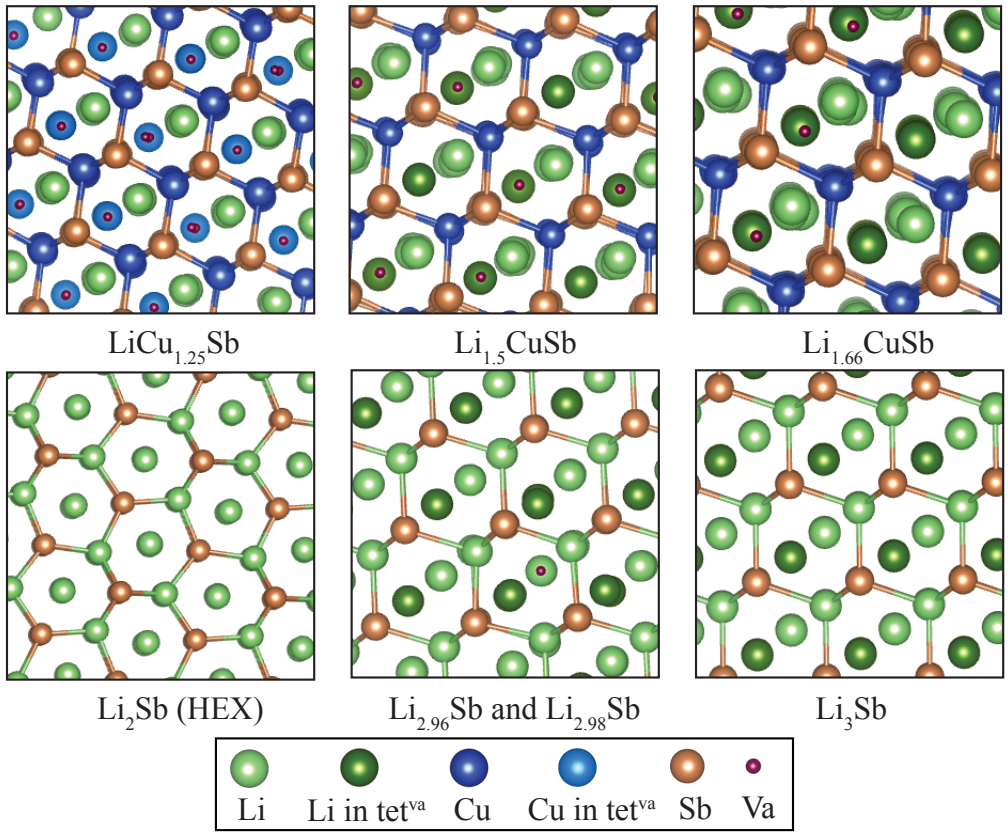

Figure 4.3: The crystal structures predicted as stable phases from the DFT calculation. All ground states structures except Li_2Sb have the fcc Sb sublattice. Li_2Sb has hexagonal symmetry.

Surprisingly, the Cu_2Sb compound is not predicted to be a ground state relative to Cu (fcc) and Sb (A7) using DFT-PBE, having a positive formation energy of 8.5 meV per atom. We recalculated the formation energy of Cu_2Sb relative to Cu (fcc) and Sb (A7) using a variety of different approximations to DFT (PW91, LDA), different pseudopotentials, with and without spin polarization and using different U parameters within DFT+U approximations. In all cases, Cu_2Sb was predicted to have a positive formation energy.

The failure of approximations to DFT to predict Cu_2Sb as a stable phase in the Cu-Sb binary implies one of two possibilities: (i) DFT within the approximations considered here fails to accurately describe bonding in the Cu_2Sb compound, or (ii) Cu_2Sb is only stable at elevated temperature due to vibrational entropy. There is evidence that DFT-PBE incorrectly describes formation energies in other Cu containing alloys due to an incorrect prediction of the Cu d-orbital energy levels. A recent study by Zhang et al[92], for example, showed that DFT-PBE predicts incorrect zero Kelvin ground states in the Cu-Au alloy. They showed that the correct ground states are recovered with the use of a screened form of Hartree Fock as implemented in the HSE06 hybrid functional approach[41]. Applying the same HSE06 hybrid functional approach[41] to the Cu-Sb binary, we find that Cu_2Sb is predicted to be a stable compound having a formation energy of -47.1 meV/atom. We also explored the possibility that DFT-PBE correctly predicts formation energies in the Cu-Sb binary, but that vibrational entropy stablizes the Cu_2Sb compound at elevated temperature. Vibrational free energies for fcc Cu, A7 Sb and Cu_2Sb were calculated within the quasi-harmonic approximation by fitting force constants to DFT-PBE calculations of forces when atoms are displaced relative to their equilibrium positions (see methods section for details). The calculated formation free energy of Cu_2Sb defined as $\Delta G_{Cu_2Sb} = G_{Cu_2Sb} - 2G_{Cu} - G_{Sb}$ based on DFT-PBE is shown in Fig4.4. Clearly, vibrational entropy stabilizes Cu_2Sb relative to decomposition into Cu (fcc) and Sb

(A7) with increasing temperature, becoming thermodynamically stable at 190 K. At room temperature, Cu_2Sb is predicted to have a negative formation free energy of -13.4 meV per atom.

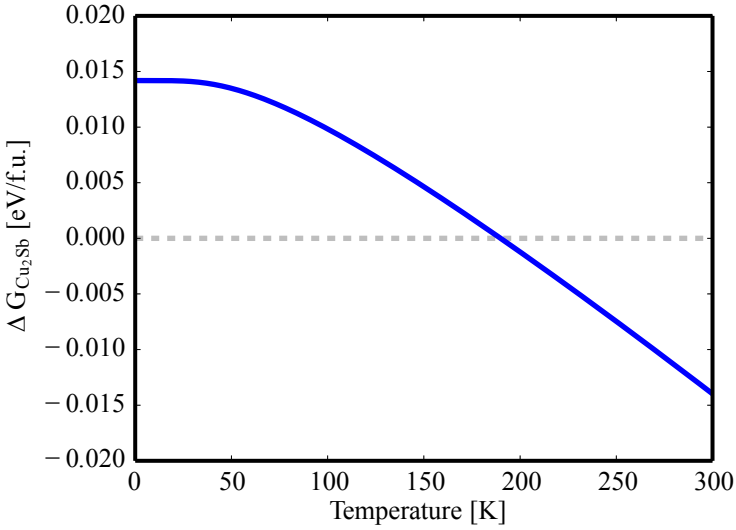

Figure 4.4: Gibbs formation free energy of Cu_2Sb as calculated with the quasi-harmonic approximation. The temperature at which Cu_2Sb becomes stabilized relative to Cu and Sb(A7) is at 190 K.

4.3.1.2 Room temperature thermodynamic properties

The DFT-PBE formation energies of the symmetrically distinct configurations over the fcc Sb sublattice were used to parameterize the expansion coefficients of a ternary cluster expansion Hamiltonian. We only used the configurations that maintained an fcc Sb sublattice after relaxation. Furthermore, we primarily used configurations having formation energies within 500 meV from the convex hull. Our optimal cluster expansion includes four point terms (two for tetrahedral sites and two for octahedral sites), 12 pair clusters, 32 triplet cluster, and 15 quadruplet clusters. The root-mean-square error (RMS), which is an indicator of the quality of the fit, is 12.87 meV per interstitial site, while the cross-validation score (CV), which is a measure of the ability of the cluster expansion to predict energies that are not included in the

fit, is 16.18 meV per interstitial site. Unlike DFT calculation, an extra configuration, $Li_{1.33}CuSb$ is predicted as a stable structure. However, the formation energy difference between DFT calculation and cluster expansion was 3 meV. This is within the fitting error of the cluster expansion and close to the numerical accuracy of DFT-PBE with respect to k-point sampling. When we count on errors from the fitting, this cluster expansion qualitatively well predicted ground states with DFT-PBE calculation.

Grand canonical Monte Carlo simulations were applied to the cluster expansion to calculate the dependence of the grand canonical energy as well as the Li and Cu concentrations on temperature and Li and Cu chemical potentials μ_{Cu} and μ_{Li}. Free energies were calculated with free energy integration techniques [77, 88]. As reference states for free energy integration, we used stoichiometric Li_3Sb for the Li-rich, Cu-poor region and ternary ground state ordered configurations at low temperature to calculate free energies in the ternary composition space. Low temperature free energies in the reference states were calculated with low-temperature expansions [77, 36].

Figure 4.5a shows the calculated ternary phase diagram at 300 K. The phase diagram was determined by applying the common tangent construction to calculated free energies. The free energies for the Li-containing phases were those calculated with the grand canonical Monte Carlo simulations. For Cu_2Sb, we used the vibrational formation free energy to ensure that it appears as a stable phase. We did not include vibrational free energy contributions for any of the Li-containing phases. The implicit assumption when neglecting vibrational excitations is that their inclusion will not qualitatively change the topology of the phase diagram away from the Cu-Sb binary. The calculated phase diagram shows a stable ternary solid solution, having composition Li_xCu_ySb with x ranging between 1.3 and 1.6 and with y ranging between 1 and 1.02. The octahedral sites of the fcc Sb sublattice in the solid solution are exclusively filled by Li, while the Cu fill half the tetrahedral sites forming an fcc sublattice. The remaining tetrahedral sites contain disordered Li and vacancies, with a

very dilute concentration of Cu at the more Cu rich concentrations. These sublattice concentrations, predicted with a ternary cluster expansion describing disorder over all interstitial sties, are qualitatively consistent with a study by Matsuno [47] who used a binary cluster expansion describing Li-vacancy disorder over the tetrahedral sites occupied by Li and the octahedral sites. The Monte Carlo simulations applied to the ternary cluster expansion suggest that there is very little Cu disorder and a minimal concentration of Cu over the tetrahedral sites occupied primarily by Li and vacancies.

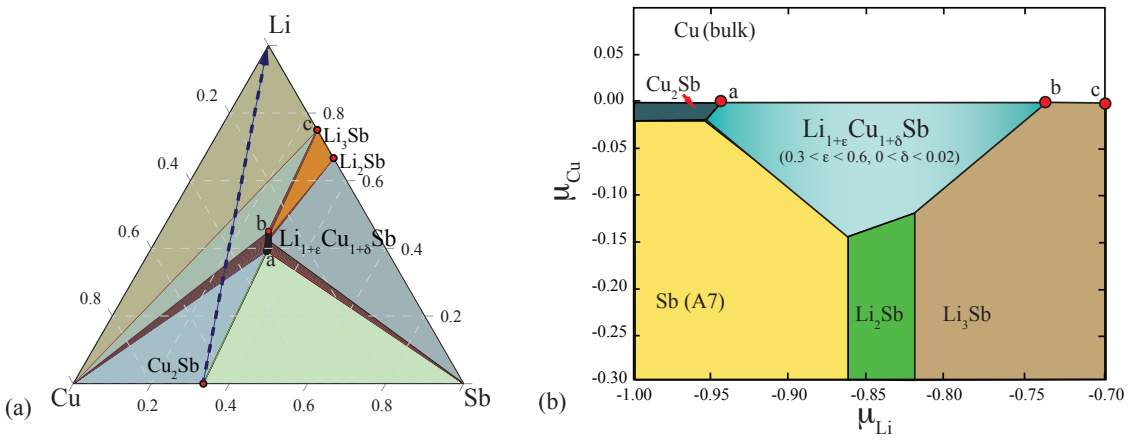

Figure 4.5: (a) A projection of the convexhull in ternary composition space obtained by the grand canonical Monte Carlo calculation at 300 K. (b) Phase stability as a function of the of Li and Cu chemical potentials, μ_{Li} and μ_{Cu} at 300K

Phase stability can also be plotted as a function of the Li and Cu chemical potentials, μ_{Li} and μ_{Cu}, as shown in Figure 4.5b. This phase diagram was calculated by minimizing the grand canonical free energies of each phase at fixed chemical potentials μ_{Li} and μ_{Cu}. The reference states for the Li and Cu chemical potentials in Figure 4.5b are bcc Li and fcc Cu respectively. Hence, pure Cu is stable for positive Cu chemical potentials, independent of the Li concentration, while pure Li is stable for positive Li chemical potentials. Pure Sb is stable for very negative Li and Cu chemical potentials. The lithium rich Li_2Sb and Li_3Sb phases become stable at in-

creasing μ_{Li} and sufficiently negative μ_{Cu}. The solid solution $Li_{1+\varepsilon}Cu_{1+\delta}Sb$ phase is stable over a sizable Li and Cu chemical potential range.

The voltage of an electrochemical cell is related to the Li chemical potentials of the cathode and anode according to

$$V = -(\mu_{Li} - \mu^0_{Li})/e \tag{4.2}$$

where, μ_{Li} is the Li chemical potential in the positive electrode and μ^0_{Li} is the Li chemical potential of the reference anode, which we choose to be metallic Li. Figure 4.6 shows the calculated voltage as a function of Li content x in Li_xCu_ySb along a path in ternary composition space denoted by the dashed arrow in Figure 4.5a. Since the electrode passes through three-phase and two-phase regions containing pure Cu along this path, the Cu chemical potential in Li_xCu_ySb is equal to that of fcc Cu, which due to our choice of reference state is equal to zero (i.e. μ_{Cu}=0). The first plateau in the voltage profile ($0 < x < 1.3$) corresponds to a passage through the Cu + Cu_2Sb + $Li_{1+\varepsilon}Cu_{1+\delta}Sb$ three phase region where the Li chemical potential remains constant as the relative phase fractions of the three coexisting phases changes upon Li insertion or removal. The three phase region is a point in the chemical potential phase diagram (point a in Figure 4.5b). The voltage profile between $1.3 < x < 1.6$ decreases continuously since the electrode then passes through the two-phase region between a solid solution of $Li_{1+\varepsilon}Cu_{1+\delta}Sb$ and Cu. The second plateau emerges as the electrode passes through the three phase region between $Li_{1+\varepsilon}Cu_{1+\delta}Sb$ + Li_3Sb + Cu. This three phase region corresponds to point b in the chemical potential phase diagram Figure 4.5b. Also shown in Figure 4.6 (dashed red line) is the voltage when Li reacts with Sb in the absence of Cu. This voltage profile exhibits two plateaus separated by a small step due to the stability of the hexagonal Li_2Sb phase.

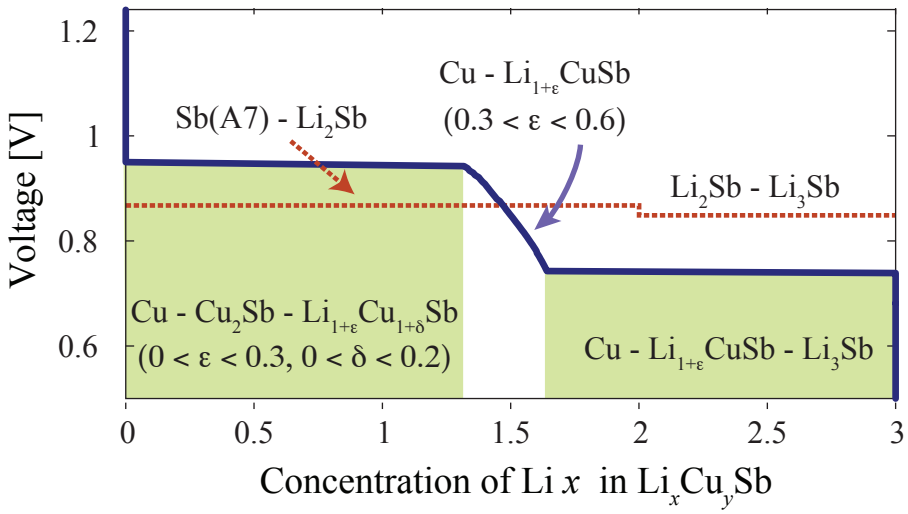

Figure 4.6: The calculated voltage is obtained from MC calculation using the Nernst equation. Because pure Cu is extruded by insertion of Li, chemical potential of Cu is fixed as 0 while lithiation precess. Thus voltage is obtained by finding equilibrium concentrations of Li and Cu at μ_{Cu}= 0. (The calculated equilibrium voltage curve in Li-Sb system as a function of Li concentration is shown in red dot line)

4.3.2 Kinetic Properties

An important trigger of path hysteresis in conversion and displacement reactions was found to be a large difference in the diffusion coefficients of Li compared to that of the displaced cation in the fully lithiated phase [90]. To elucidate why the hysteresis in the displacement reaction of Cu_2Sb with Li is small compared to other chemistries, we investigated the migration barriers for Li and Cu diffusion in Li_3Sb, the fully lithiated end product of the displacement reaction.

Past first principle studies of the Li-Sb alloying reaction have predicted a very high Li mobility in Li_3Sb. Dilute vacancies in Li_3Sb prefer to occupy the octahedral sites. The migration barrier for a Li hop from a tetrahedral site into a vacant octahedral site in Li_3Sb is predicted to be $\sim$ 0.1 eV, a barrier that is substantially lower than in most intercalation compounds. The Li mobility in Li_3Sb is therefore very high. Here we also calculated the migration barrier for a Li hop from a tetrahedral site to

an octahedral site with a neighboring Cu in an adjacent tetrahedral site. Figure 4.7a shows the migration barrier of this Li hop, with the calculated migration barrier of 80 meV in the presence of a neighboring Cu being even lower than that in the absence of Cu. Also evident in Figure 4.7a is the tendency of Cu to change the site preference for the vacancy, with the vacancy now preferring the tetrahedral site over the octahedral site by 25 meV. This site preference for the vacancy is similar to that exhibited by the ternary $Li_{1+\varepsilon}Cu_{1+\delta}Sb$ solid solution.

We also considered all possible migration paths of Cu in Li_3Sb. We found that an isolated Cu in Li_3Sb is unstable in an octahedral site next to a vacant nearest neighbor tetrahedral site. The energy of the crystal increases monotonically as Cu migrates from a tetrahedral site to an adjacent vacant octahedral site. Cu hops from a tetrahedral site to a nearest neighbor vacant octahedral site therefore cannot occur. As a result, Cu migration in the presence of an isolated vacancy is only possible between nearest neighbor tetrahedral sites as shown in Figure 4.7b. The migration barrier for this hop is predicted to be 1.2 eV, a value that is substantially higher than that of Li in Li_3Sb and of Li in other common intercalation compounds. This hop mechanism is therefore unlikely to contribute much to macroscopic Cu diffusion.

Li_3Sb is likely to have a high concentration of vacancies upon Li removal from the electrode during charging due to its exceptionally high Li mobility and thermodynamic stability (both energetic and entropically driven) of a Li-deficient solid solution of $Li_{3-z}Sb$. We therefore also explored Cu migration mechanisms and barriers in the presence of a pair of vacancies. Figure 4.7c shows the calculated migration barrier as Cu migrates from a tetrahedral site to an adjacent vacant tetrahedral site in the presence of a neighboring vacant octahedral site. The hop path is curved, passing through the octahedral site as illustrated in Figure 4.7c. The migration barrier for this hop is 440 meV, which, while higher than that of Li diffusion in Li_3Sb, is of the same order as Li migration barriers in common intercalation compounds

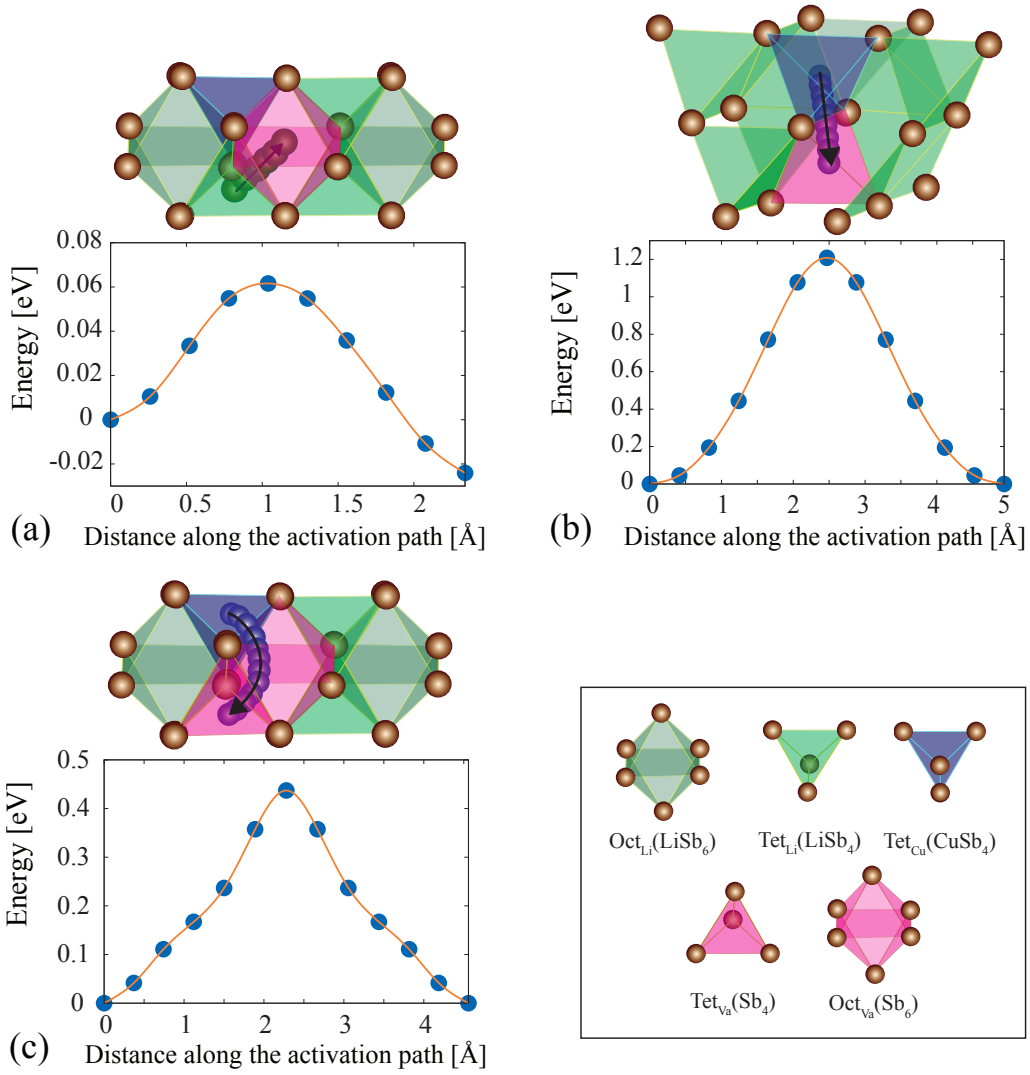

Figure 4.7: Migration barriers for Li hops and Cu hops in Li_3Sb. (a) Li hops from a tetrahedral site to adjacent vacant octahedral site next to a Cu tetrahedral site. (b) Cu hops from a tetrahedral site to adjacent vacant tetrahedral site (an isolated vacancy) (c) Cu hops from a tetrahedral site to adjacent vacant tetrahedral site through a vacant octahedral site (Cu hops into a divacancy).

[79, 11, 10]. This result suggests that vacancy clusters mediate Cu diffusion in Li_3Sb, in a similar way that vacancy clusters mediate Li diffusion in lithiated layered and spinel intercalation compounds [78]. The very fast Li mobility should ensure that the reorganization of vacancy clusters after each Cu hop is not rate limiting to Cu diffusion. The low-barrier divacancy Cu hop mechanism in a "sea" of very mobile Li ions, implies that Cu should have a high diffusion coefficient, similar to that of Li in the fully lithiated intercalation compounds.

4.4 Discussion

Conversion and displacement reactions in the electrodes of Li-ion batteries promise substantially higher capacities than can be achieved with intercalation compounds. However, the kinetic complexity of these reaction mechanisms, arising from the requirement to spatially redistribute a second species in addition to Li ions, often results in an unacceptably high hysteresis between charge and discharge. This hysteresis is due to a difference in the reaction path between charge and discharge [21, 33, 90]. While the number of reaction paths during a displacement reaction upon Li insertion are quite limited as the second mobile species must be displaced to provide sites for the incoming Li, a large multitude of reaction paths are available during charge. In the extremes, Li removal from the discharge product can either (i) be accompanied by the simultaneous reinsertion of the second cationic species such that the electrode retraces the original discharge path or (ii) occur without any reinsertion of the displaced cation. Any other path between the two extremes in which a fraction of the displaced cations reenters the crystal is also possible. In the second extreme, the path followed during Li removal differs substantially from that followed during Li insertion and the voltage will exhibit a large hysteresis between charge and discharge.

Compared to other electrode chemistries that undergo a displacement or conversion reaction, Cu_2Sb is unusual in that it exhibits a negligible hysteresis. While

the first voltage plateau due to the conversion of Cu_2Sb to a two-phase mixture of the ternary $Li_{1+\varepsilon}Cu_{1+\delta}Sb$ phase and metallic Cu during Li insertion is not reversible upon Li extraction, the subsequent reactions are. The reaction path followed during the second voltage plateau in which $Li_{1+\varepsilon}Cu_{1+\delta}Sb$ reacts further with Li to form Li_3Sb and metallic Cu is readily retraced experimentally upon Li extraction to reform $Li_{1+\varepsilon}Cu_{1+\delta}Sb$. Hence any difference between the discharge voltage and the charge voltage is due to dissipative polarization and not to a difference in reaction pathways.

A theoretical study of hysteresis accompanying the displacement reaction of Li with $CuTi_2S_4$ identified two triggers in the fully discharged state that cause path hysteresis [90]: (i) a large difference in mobility between Li and the displaced cationic species (i.e. Cu), with the displaced cation being substantially less mobile than Li and (ii) a lack of a thermodynamic driving force for the reinsertion of the displaced cation upon retracing the discharge path during charge. The results of this study suggest that the absence of path hysteresis in the Li-Cu-Sb ternary must be due to unique thermodynamic and kinetic properties of Li_3Sb, the phase that forms after complete discharge.

Li removal from the fully discharged electrode, consisting of a two-phase mixture of Li_3Sb and Cu, must be accompanied by the simultaneous reinsertion of Cu into Li_3Sb to reform $Li_{1+\varepsilon}Cu_{1+\delta}Sb$. Otherwise Li extraction will lead to the formation of either Li_2Sb or, as occurs during the Li-Sb alloying reactions, the formation of pure Sb. As can be seen in Figure 4.6, the equilibrium voltage profiles for the two reaction paths differ significiantly.

When Li_3Sb coexists with metallic Cu in the fully discharged state, it contains a very dilute concentration of dissolved Cu. In this two-phase equilibrium, the Cu chemical potential within Li_3Sb will be equal to that of metallic Cu, μ^o_{Cu}, which is equal to zero when using metallic Cu as the reference for the chemical potential. In

the phase diagram of Figure 4.5b the two-phase coexistence between Li_3Sb and Cu will reside along the line between points b and c, depending on the externally imposed voltage (which determines the Li chemical potential). In order for Cu to reinsert into Li_3Sb such that it can transform to $Li_{1+\varepsilon}Cu_{1+\delta}Sb$, the Cu chemical potential within Li_3Sb must be negative. Otherwise there is no thermodynamic driving force for Cu to leave the metal precipitates and dissolve in Li_3Sb. A sufficient amount of Cu must dissolve in Li_3Sb in order to supersaturate the phase with Cu such that there is a nucleation driving force to form $Li_{1+\varepsilon}Cu_{1+\delta}Sb$.

It is useful to visualize the trajectory in chemical potential space for a particular path in concentration space, which can be determined using the calculated free energy of $Li_xCu_ySb_{1-x-y}$ around the Li_3Sb stoichiometry. Figure 4.8 compares several trajectories in chemical potential space relative to the equilibrium phase diagram. As is clear from path I in Figure 4.8, Li extraction without Cu insertion will generate a negative Cu chemical potential. Hence the electrochemical removal of Li driven by an increase in the voltage (and thereby decreasing the Li chemical potential), will set up chemical driving forces for Cu in the metallic phase to enter Li_3Sb. The trajectory of path I in Figure 4.8 never intersects the stability domain of the $Li_{1+\varepsilon}Cu_{1+\delta}Sb$ solid solution however. Hence, to avoid transforming directly to Li_2Sb or pure Sb, Cu insertion and diffusion must be sufficiently rapid compared to the rate of Li extraction to deflect the trajectory in chemical potential space along a path such as path II, which does pass through the $Li_{1+\varepsilon}Cu_{1+\delta}Sb$ domain. As can be seen in Figure 4.8, path II corresponds to a scenario where Li removal is accompanied by simultaneous insertion of Cu.

While the migration barrier for Cu diffusion in Li_3Sb in the presence of vacancies is higher than that of Li, it is nevertheless not much higher than typical barriers predicted for high rate capable intercalation compounds such as layered Li_xCoO_2, spinel Li_xTiO_2, and Li_xTiS_2 [79, 11, 10]. Intercalation compounds having similar migration

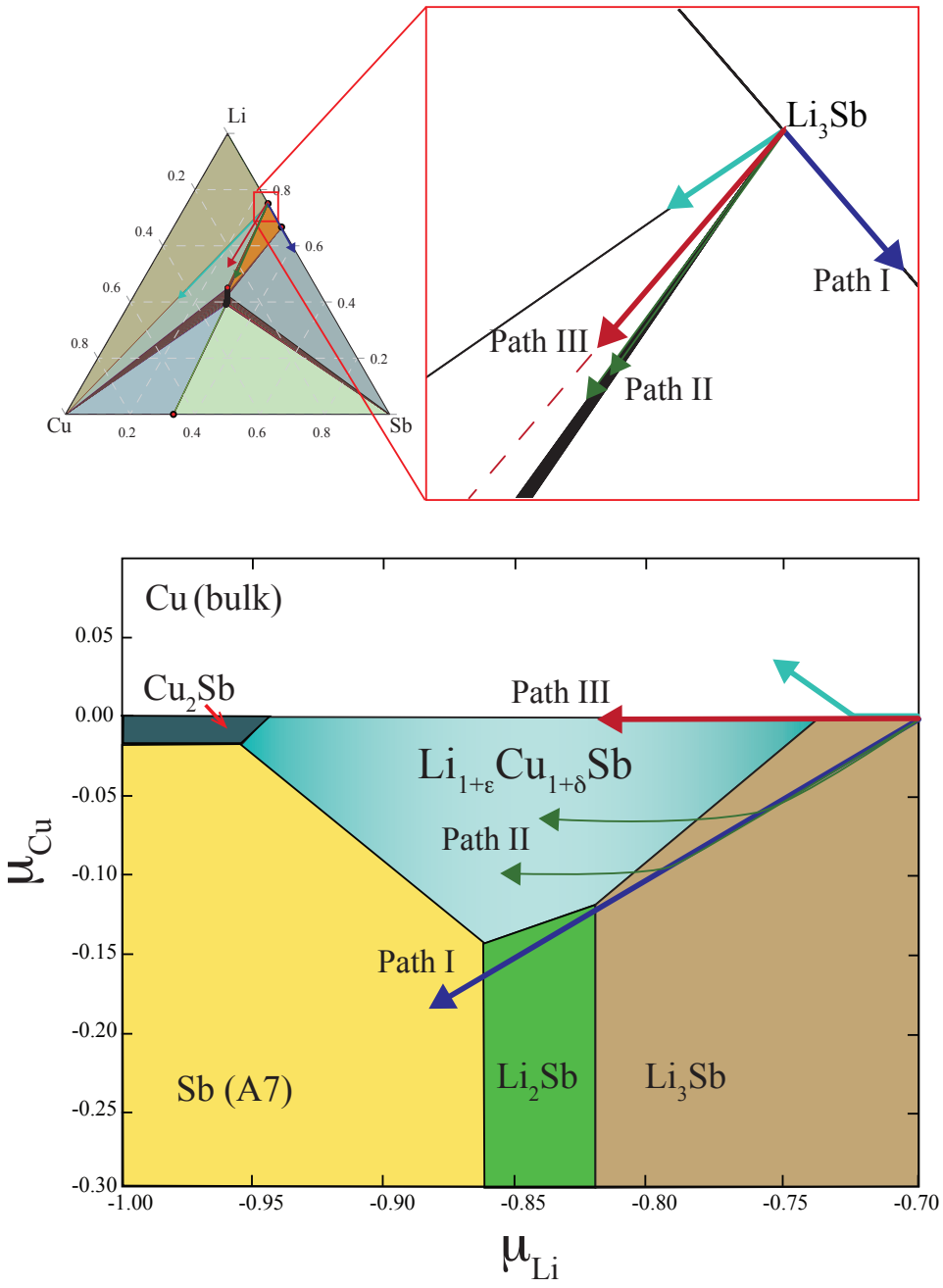

Figure 4.8: Schematic illustration of several charge reaction trajectories in chemical potential space for a particular path in concentration space.

barriers as predicted with DFT and where diffusion is mediated by divacancies rarely require large overpotentials. Typical intercalation compounds rarely require more than 0.1 to 0.2 eV over potentials to achieve a reasonable charge or discharge rate. This suggests that driving forces of -0.1 to -0.2 eV may be sufficient to reinsert Cu on the time scale of typical charge rates as involves similar insertion processes involving Cu diffusion in Li_3Sb, mediated by divacancy diffusion with migration barriers of the order of 450 meV.

While the predicted ternary Li-Cu-Sb phase diagram qualitatively agrees with experiment, the failure of DFT-PBE to predict Cu_2Sb as a ground state along the Cu-Sb binary as well as similar documented failures in other Cu containing alloys suggest that the qualitative predictions of formation energies may not be very accurate. Since the contributions of vibrational excitations to the free energy do lead to a stabilization of Cu_2Sb relative to a two-phase mixture of Sb and Cu, it is not evident whether Hartree-Fock corrections to DFT, which do predict a negative formation energy for Cu_2Sb, are needed to explain the room temperature stability of this phase. If, however, Hartree-Fock corrections to DFT as implemented in HSE06 are crucial to more quantitatively predict formation energies of the Cu containing compounds, our HSE06 results for Cu_2Sb, predicting a negative formation energy of -43 meV/atom, suggests that the PBE formation energies of the $Li_{1+\varepsilon}Cu_{1+\delta}Sb$ ternary compounds are likely under predicted. While this may not alter the qualitative phase diagrams, a lowering of the ternary formation energies will widen the chemical potential interval in which the $Li_{1+\varepsilon}Cu_{1+\delta}Sb$ phases are stable, increasing the amount of polarization in Cu chemical potential that can be tolerated to maintain a reversible reaction to $Li_{1+\varepsilon}Cu_{1+\delta}Sb$ during charging of the Li_3Sb + Cu two phase mixture.

4.5 Conclusion

We investigated the thermodynamic properties of the various compounds that form during the lithiation of Cu_2Sb. We identified the existence of a stable ternary solid solution $Li_{1+\varepsilon}Cu_{1+\delta}Sb$ with the strong site preference of Li filling all the octahedral sites and Cu filling half of the tetrahedral sites in the fcc Sb sublattice. In addition, our first-principles study of kinetic properties predicted that Cu has a high mobility in Li_3Sb through a vacancy cluster hop mechanism and the very fast Li mobility in Li_3Sb ensures that the vacancy clusters can reorganize after each Cu hop. Therefore, high mobility of Cu in Li_3Sb and the existence of a strong stable solid solution $Li_{1+\varepsilon}Cu_{1+\delta}Sb$ ensure the formation of $Li_{1+\varepsilon}Cu_{1+\delta}Sb$ upon Cu reinsertion in Li_3Sb. These kinetic and thermodynamic properties together are responsible for good reversibility and a minimal hysteresis in this system.

CHAPTER V

Strain induced phase transformation upon Li insertion in TiO_2(B) and Li insertion mechanism of Ca:TiO_2(B)

In situ high-resolution transmission electron microscopy (HRTEM) performed by Sungjoo Kim, revealed the occurrence of a strain-induced phase transformation upon Li ion insertion into TiO_2(B). This experimental observation motivated a first-principles investigation of phase stability of TiO_2 polymorphs as a function of Li concentration. We predict the existence of a thermodynamic driving force and a crystallographic pathway for a phase transformation of TiO_2(B) upon Li insertion to the anatase form of $Li_{0.5}TiO_2$. We also investigate intrinsic thermodynamic and kinetic properties associated with Li insertion into Ca:TiO_2(B), a new variant of TiO_2(B) with extra Ca-modified layers to the original TiO_2(B).[91] We identified possible Li insertion sites in this new structure and calculated possible Li migration paths using first principles calculation.

5.1 Strain induced phase transformation upon Li insertion in TiO_2(B)

5.1.1 Phase stability of Li_xTiO_2 polymorphs upon lithiation

We performed a first-principles investigation of phase stability among the bronze B, anatase and spinel forms of Li_xTiO_2 as a function of Li concentration. These polymorphs are candidate anode materials due to their low voltage and their structural stability as a function of Li-ion concentration. We calculated the formation free energies of lithiated TiO_2 polymorphs (Li_xTiO_2) by parameterizing first-principles cluster expansions of the configurational energy associated with Li-vacancy disorder within each polymorph and subjecting the cluster expansions to Monte Carlo simulations. Figure 5.1 shows the calculated formation free energies, which are defined as:

$$\Delta F(x) = F(x) - xE_{TiO_2} - (1-x)E_{LiTiO_2} \tag{5.1}$$

where F(x) is the free energy at concentration x in Li_xTiO_2 for a particular host structure. All free energies shown in Figure 5.1 are calculated by integrating the Li chemical potential as a function of Li concentration obtained from Monte Carlo calculation at 300K. E_{TiO_2} and E_{LiTiO_2} are the energy of the anatase TiO_2 and fully lithiated anatase $LiTiO_2$, respectively. As shown in Figure 5.1, in the absence of lithium, both anatase and bronze polymorphs are substantially more stable than the spinel structure. However, upon Li insertion, anatase and spinel Li_xTiO_2 become more stable relative to bronze B. At x=0.5 in Li_xTiO_2, an ordered spinel phase $LiTi_2O_4$ becomes the most stable structure. This agrees well with previous experimental studies on formation of spinel $LiTi_2O_4$.[18] The relative phase stabilities of Li_xTiO_2 at x=0 and x=1 in this study are in good agreement with previous DFT calculation performed by Liu, et al.[32] The calculated energy difference between $LiTi_2O_4$(B) and

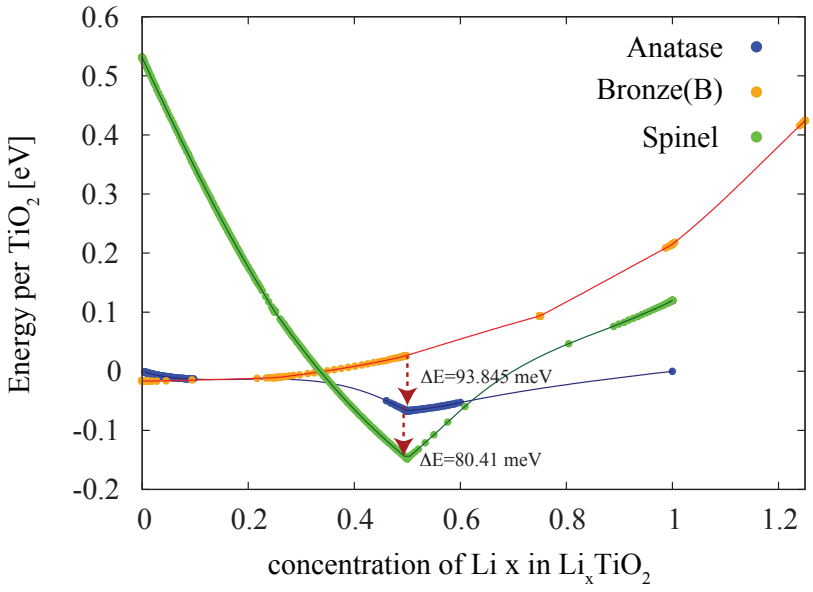

Figure 5.1: The calculated formation energies of different polymorphs of Li_xTiO_2 at 300K with respect to pure anatase TiO_2 and fully lithiated anatase phase $LiTiO_2$. The free energies of anatase Li_xTiO_2[9], Li_xTiO_2(B)[19] and spinel Li_xTiO_2 are represented with blue, orange, and green dots respectively

anatase-derivative β-$LiTi_2O_4$ is 94 meV while that between anatase and spinel is 81 meV per TiO_2 formula unit. The energy difference between $LiTi_2O_4$(B) and spinel $LiTi_2O_4$ is 174 meV per TiO_2 formula unit. The anatase form of Li_xTiO_2 becomes the most stable phase among the three polymorphs as x approaches 1.

5.1.2 Possible Phase transformation mechanism

The calculated free energy curves for the three polymorphs of lithiated titania implies that there is a strong thermodynamic driving force for the formation of anatase and spinel forms of Li_xTiO_2 upon Li insertion into the TiO_2(B) structure. However, this does not necessarily suggest that both phases can easily be formed from bronze $LiTi_2O_4$(B) since the nucleation of anatase or spinel will likely be accompanied by a large strain energy penalty as a result of misfit strains relative to the original $LiTi_2O_4$(B).

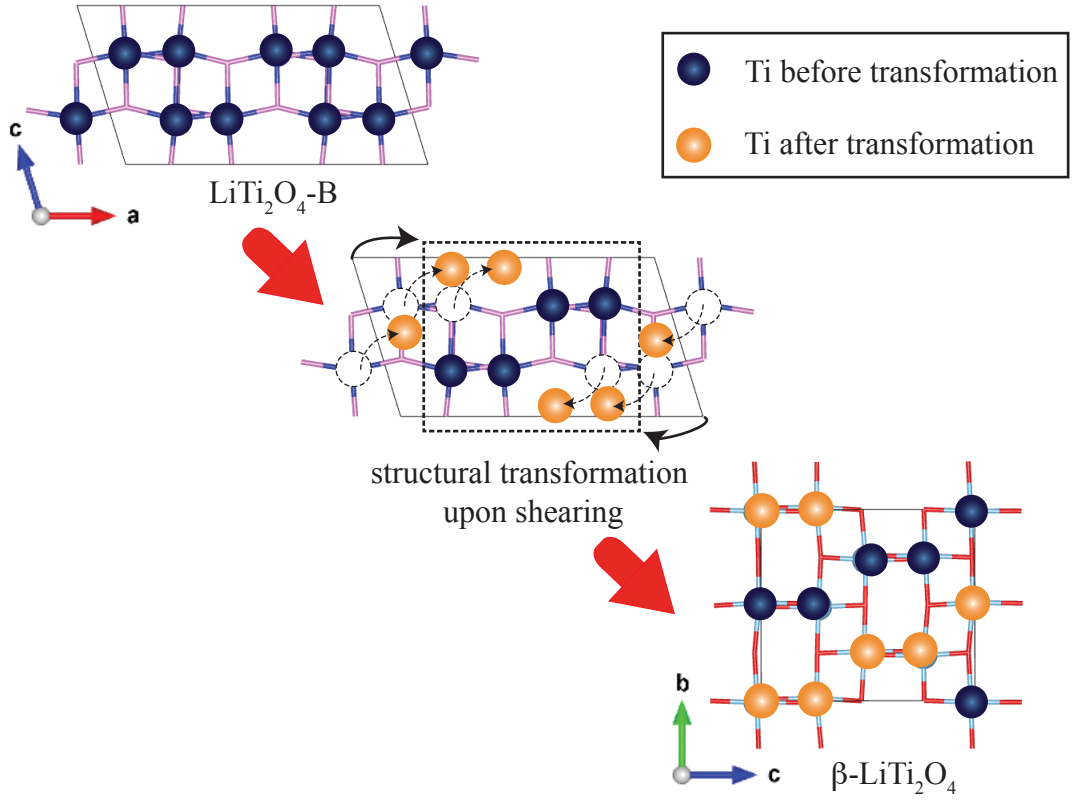

Figure 5.2: The structural relationship between $LiTi_2O_4$(B) and β-$LiTi_2O_4$ before and after shear-induced structural transformation. Li atoms are omitted to show clearly the configuration of Ti and O ordering upon structural transformation

In this section, we identify the crystallographic pathways that link bronze B $LiTi_2O_4$ to the anatase and spinel forms having the same Li concentration.

A direct crystallographic path connects bronze $LiTi_2O_4$(B) with anatase $LiTi_2O_4$ and relies on a shear and distortion as shown in Figure 5.2. By shearing the corner of a $LiTi_2O_4$(B) unitcell diagonally, the monoclinic unit cell can be transformed to the orthorhombic unitcell of ordered anatase $LiTi_2O_4$ (Figure 5.2). A similar crystallographic pathway linking bronze Li_xTiO_2(B) to spinel Li_xTiO_2 does not exist and the transformation from bronze Li_xTiO_2(B) and spinel Li_xTiO_2 requires a combination of strains along with the reordering of Ti and Li over the octahedral sites of the oxygen sublattice.

In view of the crystallographic similarities between Li_xTiO_2(B) and anatase Li_xTiO_2, the likelihood exists that two phases can coexist coherently. To analyze this possibility, we applied the Green-Lagrange strain tensor E to calculate the transformation strain required to deform one crystal into the other. If the transformation strain is small or can occur with a strain invariant plane common to both phases, the phase transformation may occur coherently without incurring large coherency strain energy penalties. The transformation strain can be defined using the starting phase as the reference. The Green-Lagrange strain is defined as:

$$E = \frac{F^+F - I}{2} \tag{5.2}$$

where F and I are the 3×3 deformation gradient matrix and the identity matrix respectively. F^+ corresponds to the transpose of F. The deformation gradient matrix F relates the lattice matrix of the transformed crystal L' to the lattice matrix of the original crystal L, according to L'=FL (where the column vectors of L are the lattice vectors). We used the lattice matrix calculated from first principles calculation.

According to Khachaturian's treatment of coherency strains[34], a transformation can proceed coherently in the absence of coherency strains along a strain invariant planes if one of the three eigenvalues of E is equal to 0, one is greater than 0, and one is less than 0.

Transformation path	λ_1	λ_2	λ_3
TiO_2(B) → Anatase TiO_2	-0.2073	0.0113	0.2705
$LiTi_2O_4$(B) → β-$LiTi_2O_4$	-0.2197	-0.0513	0.3872

Table 5.1: The eigenvalues of the transformation strains for various crystallographic transformation paths using lattice parameters from DFT calculation

Table 5.1 shows the eigenvalues of the transformation strains for various crystallographic transformation paths using lattice parameters from DFT calculation. They all show one positive and one negative eigenvalue as well as an eigenvalue close to

zero. This suggests that coexistence can occur along a plane that undergoes minimal strain in both phases. Note though that the eigenvalues close to zero are not exactly zero, and thus none of the transformation strains exactly entail a strain invariant plane. If any of these transformations occur coherently, they will be accompanied by a certain degree of coherency strain.

According to Khachaturyan treatment of coherency strain in which the elastic modulus of the original and new phase are identical, the elastic energy of an inclusion of the new phase within the lithiated TiO_2(B) matrix phase can be calculated using the following equation:

$$E(\vec{n}) = \frac{1}{2} \iiint_{-\infty}^{\infty} \frac{d^3k}{(2\pi)^3} B(\vec{n}) |\Theta(k)|^2 \tag{5.3}$$

where $\Theta(k)$ is the Fourier transform of the shape function of an arbitrarily shaped coherent inclusion and $\iiint_{-\infty}^{\infty} \frac{d^3k}{(2\pi)^3} |\Theta(k)|^2$ is equal to the volume of the nucleated phase. B($\vec{n}$) is a function of orientation of the new phase inclusion and is defined as:

$$B(\vec{n}) = \lambda_{ijkl} \epsilon^0_{ij} \epsilon^0_{kl} - n_i \sigma^0_{ij} \Omega_{jl}(\vec{n}) \sigma^0_{lm} n_m \tag{5.4}$$

where the λ_{ijkl} are the elastic moduli calculated via first principles and Ω_{jl} is the inverse tensor to $\Omega^{-1}_{ij}(\vec{n}) = \lambda_{ijkl} n_k n_l$. Table 5.2 shows the calculated elastic module used to calculate B($\vec{n}$). The elastic modulus were calculated by Yizhou Wang in internal report.

The minimum B($\vec{n}$) corresponds to the orientation of a plate of the new phase with minimum strain energy and defines the habit plane. Figure 5.3 schematically illustrates the orientation relationship between $LiTi_2O_4$ and β-$LiTi_2O_4$ and the interface plane with minimal strain energy. The atomic configuration at the interface between $LiTi_2O_4$(B) and β-$LiTi_2O_4$ matches very well with the one observed via *in*

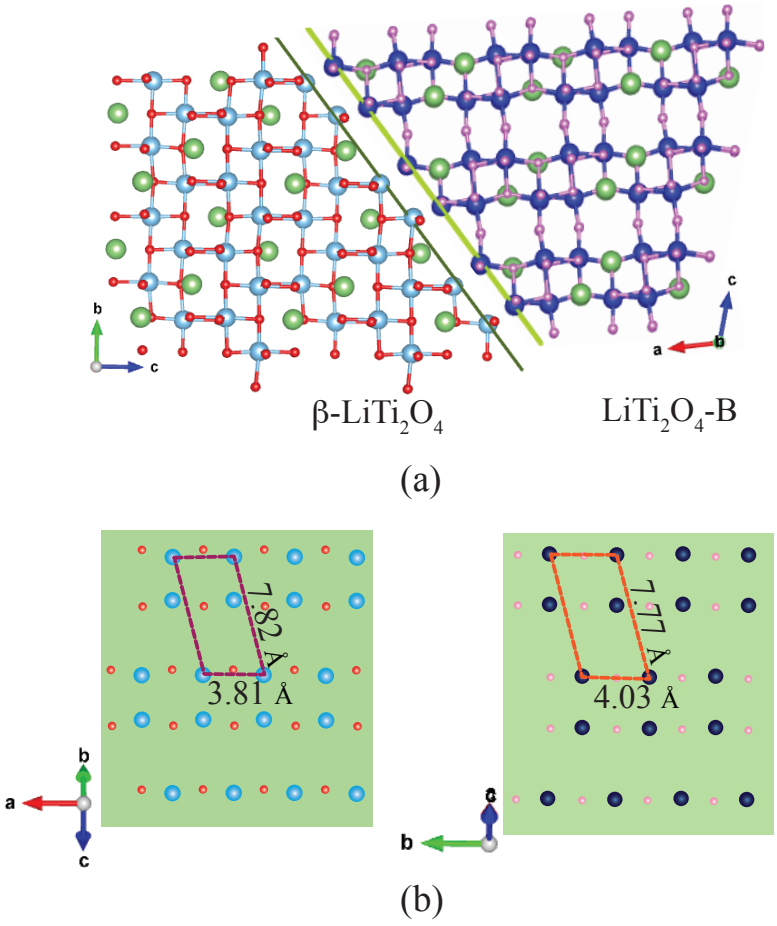

Figure 5.3: (a) The schematic illustration of the interfacial relationship along the most energy favorable habit plane upon β-$LiTi_2O_4$ phase inclusion in $LiTi_2O_4$(B). (b) The comparison of ordering of Ti and O atoms at the habit plane.

Structure	C_{ij}
Anatase TiO_2	$\begin{bmatrix} 333.40 & 142.74 & 139.73 & 0 & 0 & 0 \\ 142.74 & 333.40 & 139.66 & 0 & 0 & 0 \\ 139.73 & 139.73 & 191.39 & 0 & 0 & 0 \\ 0 & 0 & 0 & 47.2 & 0 & 0 \\ 0 & 0 & 0 & 0 & 47.2 & 0 \\ 0 & 0 & 0 & 0 & 0 & 59.29 \end{bmatrix}$
β-$LiTi_2O_4$	$\begin{bmatrix} 366.85 & 106.99 & 152.32 & 0 & 0 & 0 \\ 106.99 & 296.75 & 43.18 & 0 & 0 & 0 \\ 152.32 & 43.18 & 182.17 & 0 & 0 & 0 \\ 0 & 0 & 0 & 80.88 & 0 & 0 \\ 0 & 0 & 0 & 0 & 71.92 & 0 \\ 0 & 0 & 0 & 0 & 0 & 91.9 \end{bmatrix}$

Table 5.2: Calculated elastic modulus [in GPa] of anatase Li_xTiO_2 (x=0, and 0.5)

situ TEM upon Li insertion into TiO_2(B).

5.1.3 Conclusion

We identified the possible phase transformation between different lithiated titania polymorphs upon Li-ion insertion into TiO_2(B). Our aim in Section 5.1 was to elucidate the origins and crystallographic pathway for the bronze B to anatase transformation observed experimentally. We found that in the absence of lithium, both anatase and bronze polymorphs of TiO_2 are much more stable than the spinel form. However, upon Li insertion, anatase and spinel Li_xTiO_2 become energetically more favorable indicating the existence of a thermodynamic driving force for the transformation of bronze B Li_xTiO_2 to either the anatase or spinel forms. While spinel is more stable at x=0.5, there exists a more facile transformation path requiring only strains but no atomic reordering between the bronze B structure and ordered anatase $Li_{0.5}TiO_2$. Application of Khachaturyans approach to analyzing coherency strain energies, we found that the anatase form of $LiTi_2O_4$ can form coherently in $LiTi_2O_4$(B)

phase along crystallographic planes that are almost strain free. The atomic configuration at the interface between the two phases matches well with the one observed via *in situ* TEM upon Li insertion into TiO2(B).

5.2 Li insertion mechanism of Ca:TiO_2(B)

5.2.1 A new variant of TiO_2(B) with extra Ca-modified layers

In a recently published study by Zhang et al.[91], it was shown that calcium can stabilize a bronze B variant of TiO_2(B) by forming $CaTi_5O_{11}$. This new compound has the potential to serve as an anode material for Li-ion batteries having a theoretical capacity of 294 $mAhg^{-1}$. Zhang et al suggested that Li ions can access the $CaTi_5O_{11}$ crystal structure through the well-aligned channels in the a-b plane and along the b-axis. Especially when the a- and b-axes of $CaTi_5O_{11}$ are exposed to the surface, $CaTi_5O_{11}$ was shown to exhibit much better rate capabilities than c-axis-oriented TiO_2(B). We performed first-principles calculations to investigate the possible stable Li sites and Li insertion mechanism in $CaTi_5O_{11}$.

5.2.2 Crystal structure and Stable Li sites

Based on structural information provided by Zhang et al.[91], we performed DFT calculations using VASP to optimize the lattice parameters and atomic position of $CaTi_5O_{11}$. We used the generalized gradient approximation (GGA) as parameterized by Perdew-Burke-Ernzerhof (PBE)[62] with the projector augmented wave mothod (PAW).[40, 12] An energy cutoff of 400 eV and a gamma point-centered 4×9×2 k-point mesh for the unitcell of $Ca_4Ti_{20}O_{44}$ were used.

The optimized crystal structure of $CaTi_5O_{11}$ is shown in Figure 5.4a. This is an orthorhombic structure with four Ca atoms in the unit cell. The predicted lattice parameters are a=12.148 Å, b=3.8013 Å, c=17.99 Å, which agree well with experimental

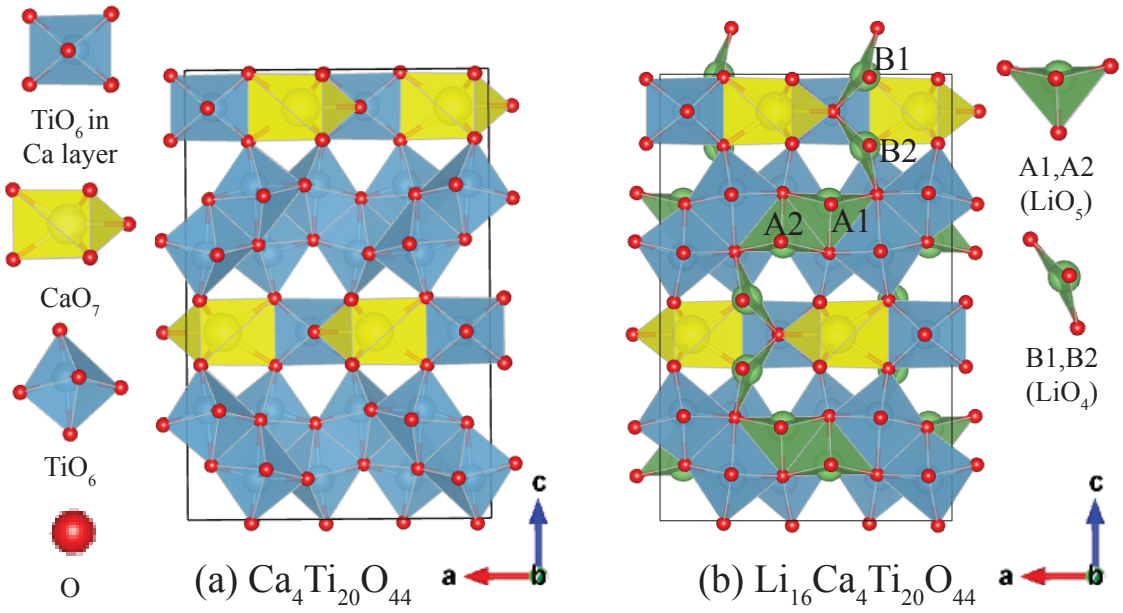

Figure 5.4: Crystal structure of (a) Ca:TiO_2 ($CaTi_5O_{11}$) and (b) Li-Ca:TiO_2 ($Li_4CaTi_5O_{11}$) projected along [0 1 0] directions. There are four symmetrically distinct stable Li sites in Ca:TiO_2 which are A1, A2, B1 and B2.

lattice parameters (a=12.1702 Å, b=3.8013 Å, and c=17.9841 Å)[91]. We identified four symmetry operations including identity, two glide planes, and one 2-fold screw axis, which belong to the space group $Pna2_1$(33).

To find possible stable Li sites, we inserted Li ions in all possible open spaces and then relaxed cell vectors and internal coordinates of the unitcell having stoichiometry $LiCa_4Ti_{20}O_{44}$. Figure 5.4b shows the stabilized lithium sites in $Ca_4Ti_{20}O_{44}$ structure. Four symmetrically distinct lithium sites have been identified and labeled A1, A2, B1, and B2. The A1 and A2 sites are 5-fold coordinated to oxygen atoms and are similar to the stable Li A1 sites in TiO_2(B)[19, 3]. The B1 and B2 sites are new stable lithium sites due to the presence of Ca modified layers and are 4-fold coordinated to oxygen atoms.

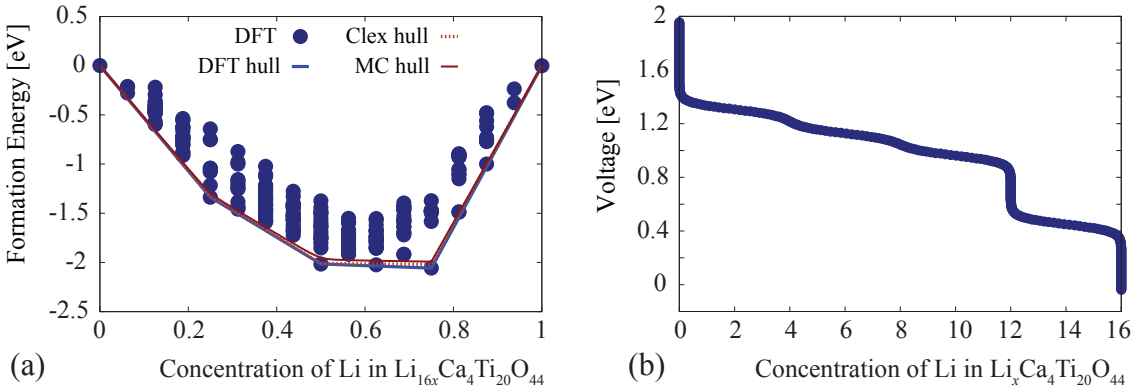

Figure 5.5: (a) Formation energies of Li-vacancy configurations per unitcell ($Li_{16x}Ca_4Ti_{20}O_{44}$) calculated from first-principles calculations (filled blue circle). The energies of the ground states are connected with a blue line forming a convexhull. The convexhull predicted by cluster expansion and Monte Carlo calculation also showed with dotted red line and solid red line respectively. (b) The calculated voltage curve as a function of Li concentration in $Li_xCa_4Ti_{20}O_{44}$ at 300 K was obtained using grand canonical Monte Carlo simulations with a cluster expansion.

5.2.3 Thermodynamic properties

Based on the stable Li sites, we enumerated symmetrically distinct Li-vacancy orderings over the stable Li sites in the unitcell. We calculated the total free energies of these configurations with DFT-PBE as implemented in VASP. The formation energies defined according to:

$$\Delta E(x) = E(Li_xCa_4Ti_{20}O_{44}) - xE(Li_{16}Ca_4Ti_{20}O_{44}) - (1-x)E(Ca_4Ti_{20}O_{44}) \quad (5.5)$$

where $E(Li_xCa_4Ti_{20}O_{44})$ is the energy of a specific Li-vacancy arrangement at concentration x in $Li_xCa_4Ti_{20}O_{44}$ shown in Figure 5.5a.

DFT calculations predict that A1 and A2 sites should fill first up to a Li concentration of x=0.5. After all A1 and A2 sites are filled by Li, B1 and B2 sites will accommodate the remaining Li ions. At a Li concentration of x=0.75, Li ions are equally distributed in both B1 and B2 sites.

Out of 274 configurations calculated, configurations having formation energies close to the convex hull were used to parameterize the expansion coefficients of a cluster expansion Hamiltonian. The resulting cluster expansion contains nine ECI: an empty cluster, four point clusters, and four pair clusters. The root-mean-square (RMS) error between calculated energies and the cluster-expaned values is 3.57 meV per interstitial site, while the weighted cross-validation score (WCV) is 20.38 meV per interstitial site. As shown in Figure 5.5a, the convexhull predicted by the cluster expansion (dotted red line) matches the convexhull from DFT calculation well.

The cluster expansions were subjected to grand canonical Monte Carlo simulations to predict the dependence of the Li chemical potential on Li concentration. Figure 5.5b shows the calculated voltage curve as a function of Li concentration. It shows a smooth solid solution until the concentration of Li reaches about 0.75 (12 Li in the unitcell). After forming the ordered phase having stoichiometry $Li_{12}Ca_4Ti_{20}O_{44}$, further Li insertion proceeds through another solid solution until the compounds is fully lithiated having composition $Li_{16}Ca_4Ti_{20}O_{44}$.

5.2.4 Kinetic properties

Li migration barriers for diffusion play an important role in selecting a kinetic path and determining the behavior of an electrode during charge and discharge. Using the nudged elastic band method implemented in VASP, we calculated the migration barriers of Li in $Ca_4Ti_{20}O_{44}$. We used a $1\times3\times1$ supercell of the orthorhombic unitcell and only considered the migration barrier at dilute Li concentrations.

In $CaTi_5O_{11}$, individual Li ions can occupy four distinct interstitial sites: A1, A2, B1 and B2. We considered all possible Li hops from one site to an adjacent interstitial site. Figure 5.6a illustrates Li migration pathways with low migration energies. Interestingly at a very dilute Li concentration by increasing unitcell along b-axis, B1 and B2 sites are more stable than A1 and A2 sites by $\sim$17 meV. Li can hop

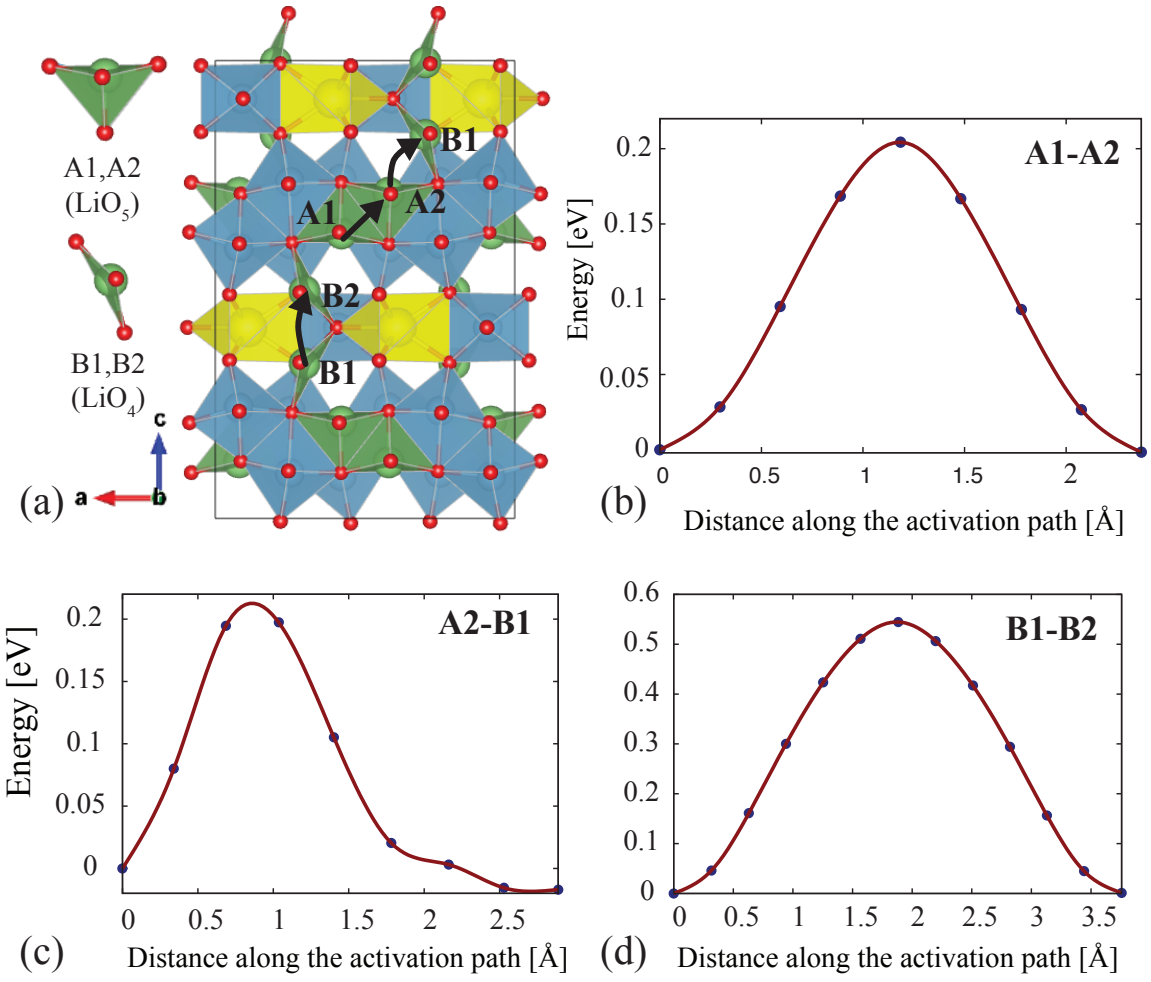

Figure 5.6: (a) All low-barrier migration pathway for a Li hop in $Ca_4Ti_{20}O_{44}$ at dilute Li concentrations. (b) Li hops from an A1 site to A2 site. (c) Li hops from an A2 site to B1 site. (d) Li hops from B1 to B2 site.

between A1 and A2 sites or between A and B sites (from A2 to B1 or B2 to A1) with low energy barriers within an a-c plane. The calculated Li migration barriers shown in Figure 5.6b and Figure 5.6c are 195-205 meV. The Li migration barrier from the B1 site to the B2 site along the c-axis is 545 meV as shown in Figure 5.6d. Although the migration barrier is higher than other Li hops in the a-c plane, this value is similar to that of Li migration barriers in other known intercalation compounds.[79]

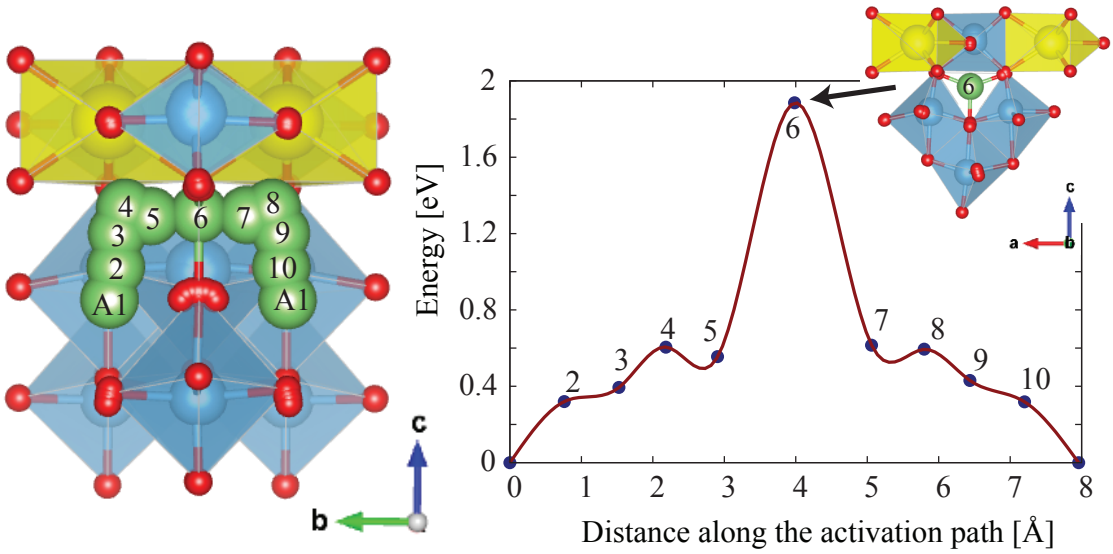

Figure 5.7: The calculated migration barrier of Li hop from site A1 to site A1 through b-axis. Each intermediate Li site and energy along the migration path are indicated with numbers.

Hops between A1 sites along the b-axis are also possible, although the barrier for this hop is 1.8 eV as shown in Figure 5.7. Li must diffuse through the trigonal plane, which shares edges with three adjacent TiO_6 octahedra. Because of the Ca-modified layer, the b-axis is not an open channel. This hop mechanism is therefore unlikely to contribute much to macroscopic Li diffusion. Therefore, we expect Li diffusion to occur two-dimensionally within the a-c plane.

5.3 Conclusion

We identified stable Li sites in $CaTi_5O_{11}$, which we have labeled A1, A2, B1 and B2. From the first-principles study of the thermodynamic properties, $CaTi_5O_{11}$ maintains its original crystal structure and shows solid solution behavior upon Li insertion. Calculations of Li migration barriers predict that Li has a high mobility along two-dimensional pathways parallel to the a-c plane, although Li can hardly diffuse through a b-axis due to the Ca-modified layer.

CHAPTER VI

Thermodynamic and kinetic properties of cubic $Na_3TiP_3O_9N$, a secondary Na-Ion battery cathode

In this chapter, we report on first-principles calculations that supported an experimental study performed in Prof Khalifah's group demonstrating that the nitridophosphate compound $Na_3TiP_3O_9N$ is a good candidate as a cathode electrode material in Na-ion batteries. First principles calculations elucidated the Na sites that become vacant first upon electrochemical Na removal. The calculated voltage exhibits a single solid solution without any intermediate plateaus. Furthermore, first principles calculations suggest that the lowest energy diffusion pathway incorporates the Na1 and Na3 sites while the diffusion pathway between Na1 and Na2 site is energetically unfavorable. This work has been published in Chemistry of Materials, an American Chemical Society journal.

6.1 First-Principles Calculations

First-principles calculations were performed using the generalized gradient approximation (GGA-PBE) to density functional theory (DFT) and the Hubbard model extension (GGA+U) as implemented in the Vienna *ab initio* Simulation package (VASP).[38] The effect of the core electrons on the valence states was treated with

the projector augmented wave (PAW) method.[12] A plane wave energy cutoff of 600 eV was used. The k-point sampling within the Brillouin one was performed with a 3×3×3 mesh for the primitive unit cell (containing a total 68 atoms). Equivalent k-point densities were used for supercells of the primitive unit cell. All calculations were performed using spin polarization with ferromagnetic ordering of the initial magnetic moments. GGA+U calculations were performed with the method of Dudarev et al.[22] with an effective Coulombic potential of U_{Jeff} = U-J (effectively, J=0).

It was found that pure GGA calculations with U=0 underestimated the average voltage by more than 1 V, which can be attributed to a large self-interaction error in GGA for localized electronic states. In contrast to simple oxides of Ti like TiO_2, the cubic structure and the isolated Ti octahedra within it are more likely to localize electronic states around Ti. By performing a systematic study of the dependence of the average voltage of the $Na_3TiN(PO_3)_3$-$Na_2TiN(PO_3)_3$ couple relative to a Na metal reference anode on the Hubbard U parameter, we determined that a value of U=5.0 eV predicts an average voltage of 2.7 V, which is close to the experimentally measured average voltage. We used this value of U to further analyze phase stability and thermodynamic properties at room temperature. The energies of five different Na-vacancy arrangements over the Na1 sites of this structure were calculated within GGA+U. For each Na-vacancy configuration over the Na1 sites, we enumerated all symmetrically distinct Ti^{3+}/Ti^{4+} arrangements and used these to initialize the DFT calculations (by initializing magnetic moments consistent with the particular Ti^{3+}/Ti^{4+} charge ordering). The lowest energy for each of the Na-vacancy configurations was then used to parametrize a cluster expansion[67] to describe the variation of the fully relaxed energy with Na-vacancy arrangement. Due to the large distance between neighboring Na1 sites, the cluster expansion Hamiltonian only includes pair, triplet, and quadruplet clusters extending up to the first-nearest neighbor cell. Grand canonical Monte Carlo simulations were applied to the cluster expansion to predict

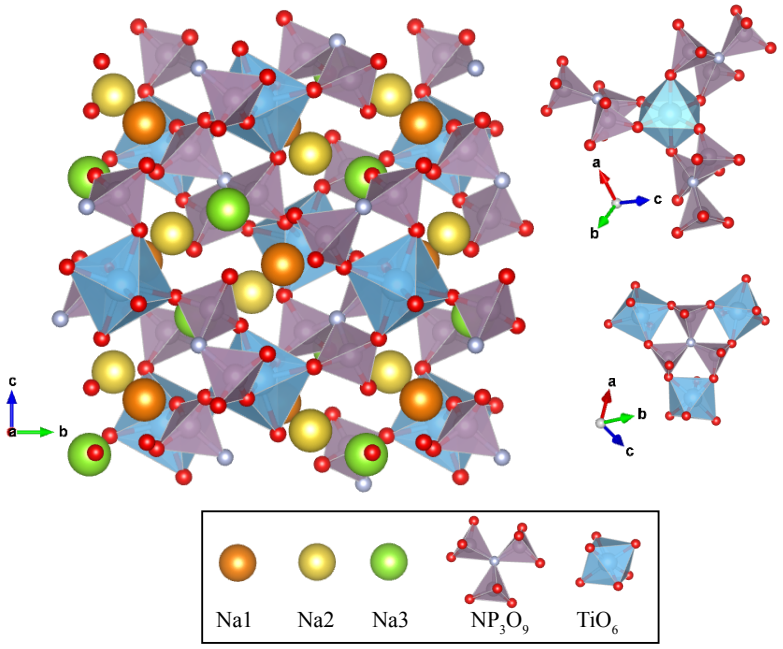

Figure 6.1: Crystal structure of $Na_3TiP_3O_9N$ view along the (100) direction. The connectivity of trimers of PO_3N tetrahedra with isolated TiO_6 octahedra shown on the right.

the equilibrium voltage curve (which is related to negative of the Na chemical potential). Migration barriers for Na hops to vacant neighboring sites were calculated with the nudged elastic band method as implemented in VASP using both GGA and GGA+U methods.

6.2 Crystallography

The crystal structure of $Na_3TiP_3O_9N$ is composed of TiO_6 octahedra which are linked by trimmers of PO_3N tetrahedral that share a center N ion and Na ions which are located in three symmetrically distinct sites, as can be seen in Figure 6.1. Four $Na_3TiP_3O_9N$ formula units form a cubic unit cell, which belongs to the space group $P2_13$ (No.198). The structure has three symmetrically distinct sites labeled Na1, Na2, and Na3.

First principles calculations done both within the GGA and with GGA+U predicts

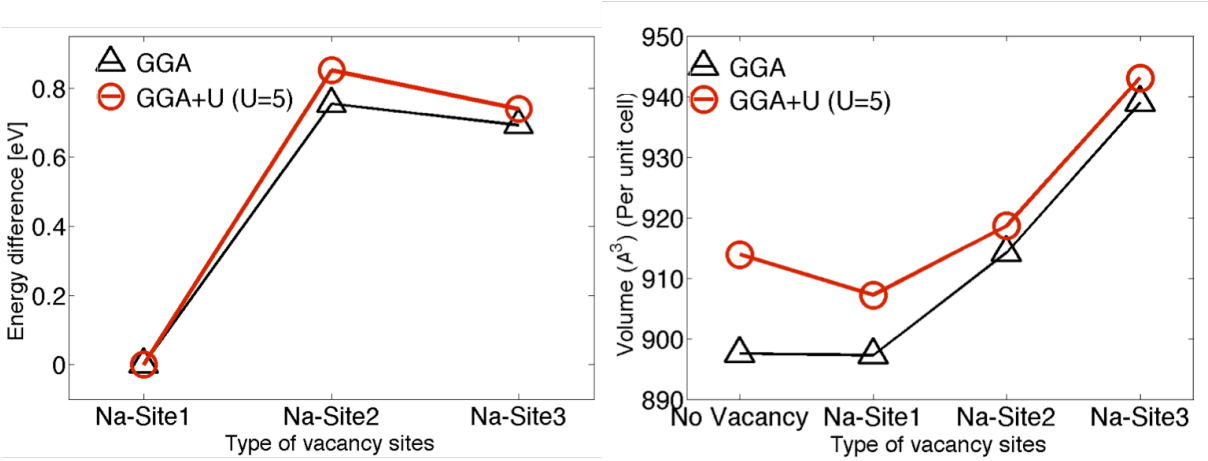

Figure 6.2: Calculated free energy (a) and volume change (b) associated with Na removal from each of the three crystallographic sites of $Na_3TiP_3O_9N$ (energies and volumes are per primitive unit cell containing four $Na_3TiP_3O_9N$)

that Na vacancies are most stable at the Na1 site. Placing the vacancies in the other sodium sites increase the energy by 210 meV (Na2) or 180 meV (Na3) per formula unit, as can be seen in Figure 6.2a. In addition, Figure 6.2b shows the volume changes upon Na removal. Both the GGA and GGA+U calculations predict a small volume change of -0.6% upon removal of Na from $Na_3TiP_3O_9N$ to form $Na_2TiP_3O_9N$, which is in good agreement with experimental observation.

6.3 Thermodynamic properties

The voltage profile of $Na_{2+x}TiP_3O_9N$ was calculated with Monte Carlo simulations performed on a cluster expansion Hamiltonian describing the energy of Na-vacancy disorder parameterized by GGA+U total energy calculations. At 0K, GGA+U calculations predict a miscibility gap between $Na_2TiP_3O_9N$ and $Na_3TiP_3O_9N$. However, various Na-vacancy ordered structures have only a slightly positive formation energy relative to $Na_2TiP_3O_9N$ and $Na_3TiP_3O_9N$, and as a result, Monte Carlo simulations predict that solid-solution behavior with a slightly sloping voltage profile should be seen at room temperature (shown in Figure 6.3), behavior which is indeed observed

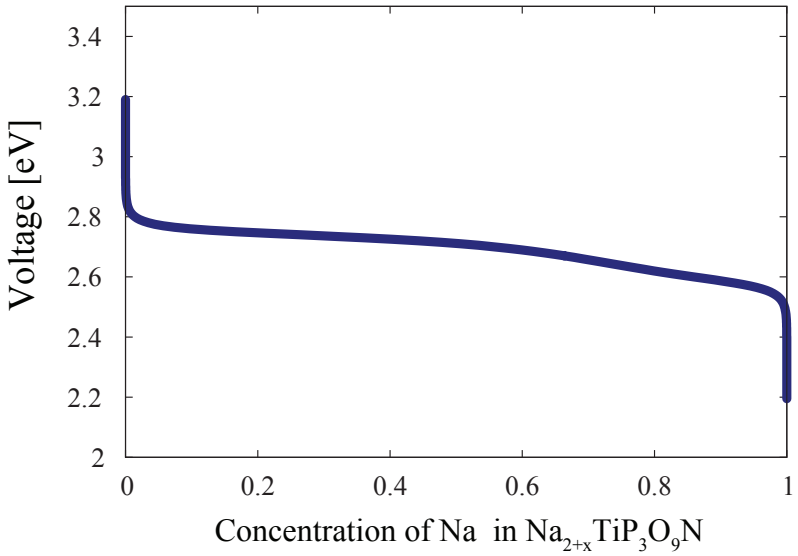

Figure 6.3: The calculated voltage curve predicted by Monte Carlo calculation as a function of Na concentration in $Na_{2+x}TiP_3O_9N$ at 300K.

in experimental GITT measurements.

6.4 Kinetic properties

The energy barriers of three possible diffusion pathways were calculated by GGA and GGA+U methods upon introduction of one Na vacancy in the 68 atom primitive cell. We calculated two different migration pathways between the Na1 and Na3 site, which are denoted as S13 and L13.

Figure 6.4 shows the S13 path, which corresponds to Na migration from Na1 to Na3 along the short path. The maximum energy barrier of this Na hop is the order of 0.87 eV. This high-energy barrier arises because Na-ion must migrate through an equilateral triangle formed by three O atoms. The high-energy barrier for the S13 path suggests that this pathway is unlikely to be important to ion diffusions in $Na_3TiP_3O_9N$.

Figure 6.5 shows migration barrier L13 from Na1 to Na3 along the long path. Unlike the S13 path, it passes through an intermediate local minimum coinciding

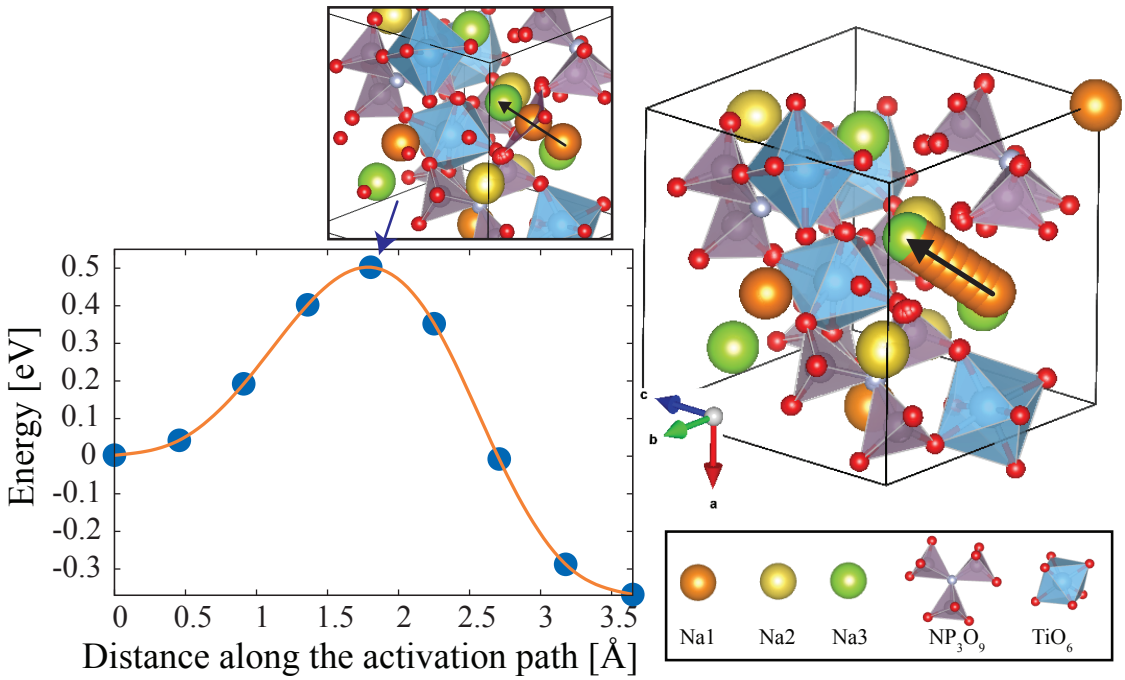

Figure 6.4: Migration barrier calculated by GGA+U methods for Na hops along from Na1 to Na3 for the shorter path (S13).

with a 4-fold oxygen coordinated site, similar to the intermediate tetrahedral sites of Li hops in many Li intercalation compounds. Although the net energy barrier of 0.75 eV for moving from Na3 to Na1 is high, the possibility of a stable intermediate would lower the theoretical barrier to only 0.50 eV, a value in good agreement with experimental results. The simple GGA energy profile obtained without the inclusion of a Hubbard U shows a similar total energy barrier (0.62 eV) as can be seen in Figure 6.6, but does not exhibit a well-resolved intermediate site.

The complexity of the energy landscape connecting the Na1 and Na3 sites makes it uncertain that the total migration barrier from Na1 to Na3 can simply be equated to an average activation barrier obtained experimentally. Further kinetic Monte Carlo simulations will be needed to better determine the equivalent average migration barrier for a complex energy landscape with many distinct hop types having a spectrum of migration barriers.

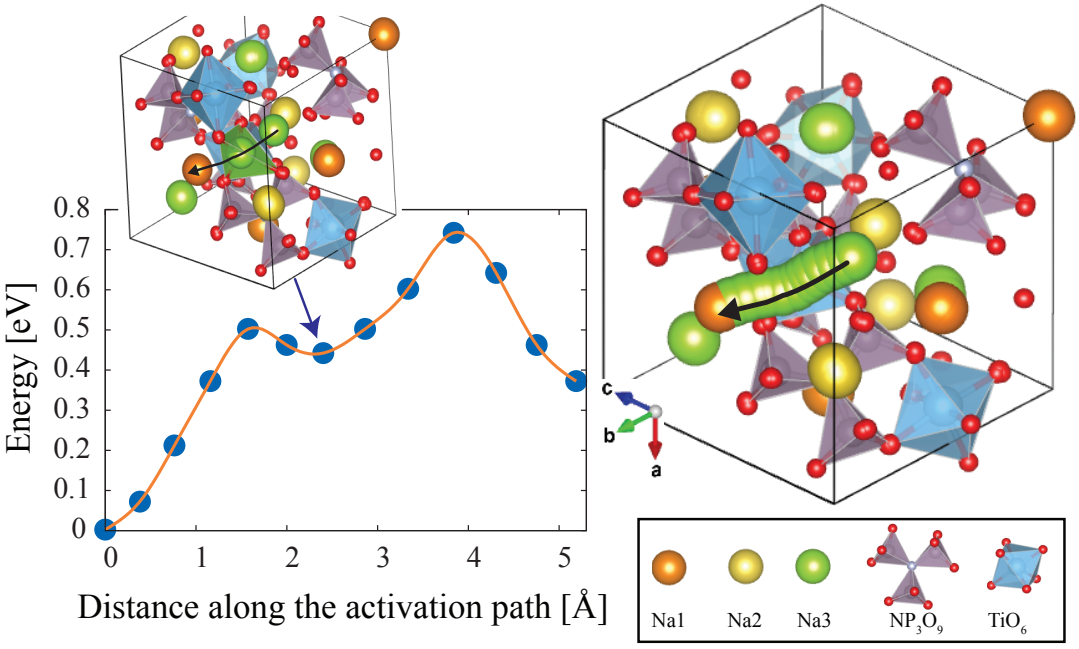

Figure 6.5: Migration barrier calculated by GGA+U methods for Na hops along from Na3 to Na1 for the longer path (L13).

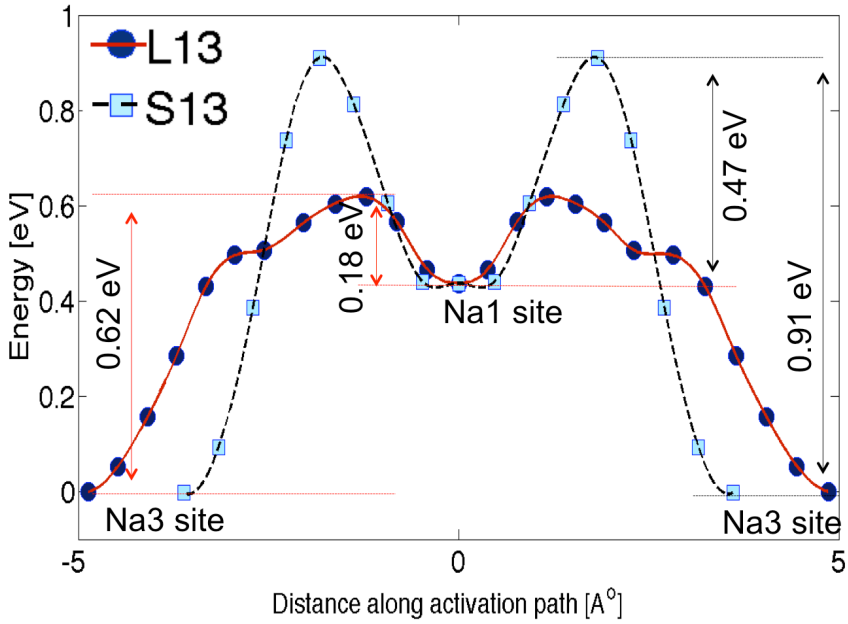

Figure 6.6: Migration barriers calculated by GGA methods along the short (S13) and long (L13) Na1-Na3 pathways.

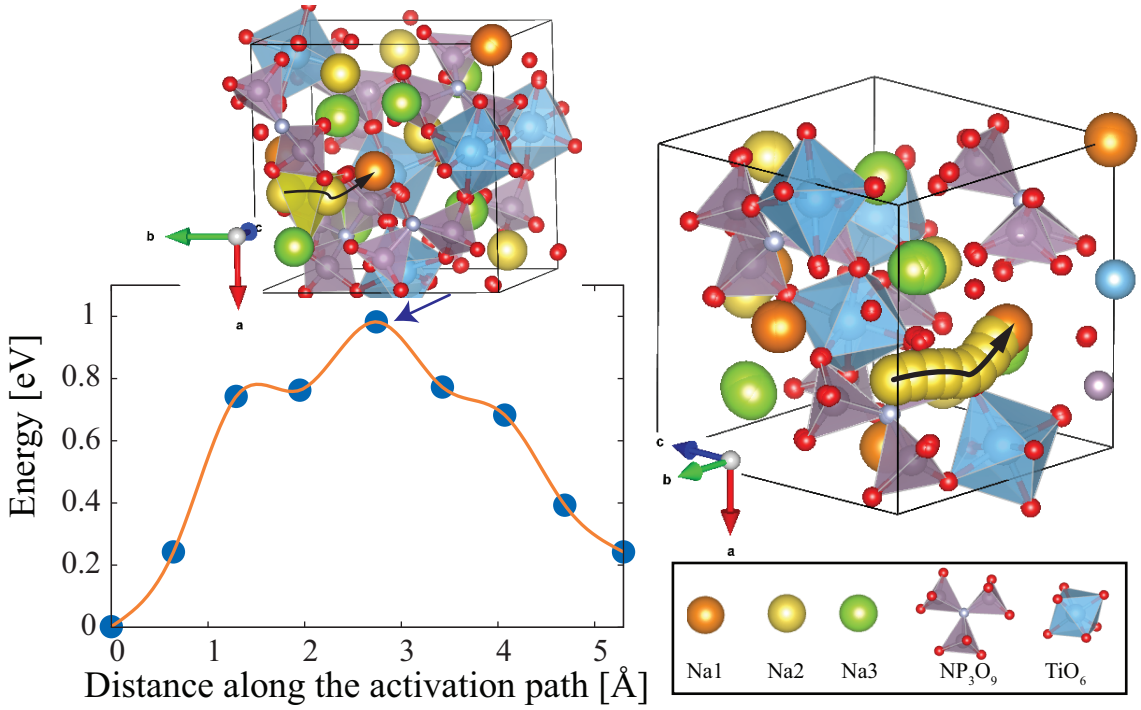

Figure 6.7: Migration barrier calculated by GGA+U methods for Na hops along from Na1 to Na2 (P13).

Figure 6.7 shows the migration barrier for Na migration between the Na1 and Na2 sites (P12). This high energy barrier of 0.98 eV for the P12 path is too large to significantly contribute to the overall ionic mobility of $Na_3TiP_3O_9N$.

Figure 6.8 shows all symmetrically equivalent L13 pathways. These hops form a three-dimensional network, allowing three dimensional Na diffusion.

6.5 Conclusion

First principles calculations predict that Na1 site is depopulated during sodium removal. The lowest energy pathway was found to be along the L13 path from Na1 and Na3 resulting in three-dimensional Na diffusion. The 3D Na-ion migration pathways, extremely small volume changes and good cyclic voltage range make this structure type particularly attractive for rechargeable Na-ion battery applications.

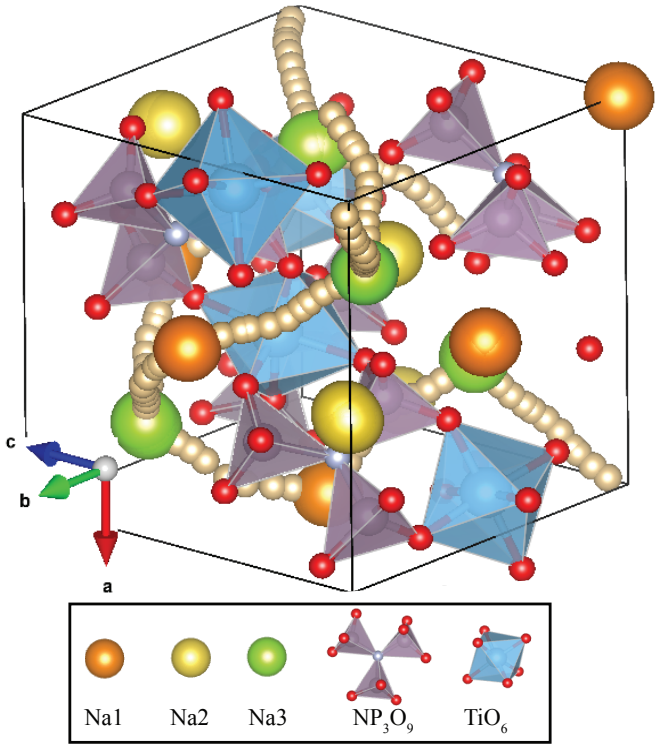

Figure 6.8: The connectivity of symmetrically equivalent low migration pathways (L13).

CHAPTER VII

Conclusion

An underlying aim of this thesis was to elucidate the origins of hysteresis and irreversibility in high capacity electrode chemistries. To this end, we focused on the Li-Sb binary and the Li-Cu_2Sb ternary, both candidate anode materials with high theoretical capacities. We also investigated factors that lead to irreversibilities in titanate based phases.

In the Li-Sb binary, we predict a very high Li mobility in Li_3Sb, which leads to large overpotentials during charge where the driving force for the nucleation of Sb is substantially larger than that of Li_2Sb upon Li extraction from Li_3Sb. A high cation mobility is usually desirable especially when the equilibrium path passes through a solid solution. However, as manifested in the Li-Sb system, it may lead to path hysteresis when Li extraction requires the occurrence of phase transformations. When the electrode passes through a metastable solid solution and reaches high overpotentials, a lever effect sets in whereby much larger nucleation driving forces emerge for phases with a larger change in Li concentration than for intermediate phases along the equilibrium path. These results suggest that to suppress path hysteresis, a balance among all competing kinetic processes during Li insertion and removal is required, especially between the rates of Li diffusion and phase transformations.

In the Li-Cu_2Sb displacement system, we identified the intrinsic properties of the

various compounds that form in the Li-Cu-Sb ternary that facilitate reversibility and minimize hysteresis between charge and discharge. We found that Cu has a high mobility in Li_3Sb through a vacancy cluster hop mechanism, with the very fast Li mobility in Li_3Sb ensuring that the vacancy clusters can reorganize after each Cu hop. In addition, the existence of a stable solid solution $Li_{1+\varepsilon}Cu_{1+\delta}Sb$ in a wide range of Li and Cu chemical potentials ensures the formation of $Li_{1+\varepsilon}Cu_{1+\delta}Sb$ upon Cu reinsertion in Li_3Sb. These kinetic and thermodynamic properties together are responsible for good reversibility and a minimal hysteresis in this system.

To elucidate the factors that lead to irreversibility between discharge and charge, we focused on the TiO_2(B) intercalation system. We identified strong structural similarities between $LiTi_2O_4$ (B) and anatase $LiTi_2O_4$. A calculation of the free energy of TiO_2(B) and anatase TiO_2 as a function of Li concentration showed that anatase $LiTi_2O_4$ is more stable than $LiTi_2O_4$(B). Using Khachaturyans formalism to analyze coherent mechanical equilibrium, we also found that anatase $LiTi_2O_4$ can be formed coherently in $LiTi_2O_4$(B) phase along crystallographic planes that are almost strain free. This result sheds light on thermodynamic driving forces and crystallographic pathways that lead to irreversibility during charge and discharge cycles.

In addition to investigating the origins of hysteresis and irreversibility, we also studied the electrochemistry of novel intercalation host materials such as $CaTi_5O_{11}$ and $Na_3TiP_3O_9N$ for Li-ion and Na-ion battery applications, respectively.

For the $CaTi_5O_{11}$ system, we identified stable Li sites and the most favorable Li migration pathways. Our first principle calculations predict solid solution behavior within $Li_xCaTi_5O_{11}$ upon Li insertion. Furthermore, we predict a high Li mobility along two-dimensional pathways parallel to the a-c plane. For the $Na_3TiP_3O_9N$ system, we explored the possible Na removal sites and diffusion pathways with low migration barriers.

BIBLIOGRAPHY

BIBLIOGRAPHY

[1] M. P. Allen and D. J. Tildesley. *Computer Simulation of Liquids*. Clarendon Press; Oxford University Press, Oxford [Oxfordshire] : New York, 1987.

[2] G. G. Amatucci and N. Pereira. Fluoride based electrode materials for advanced energy storage devices. *J. Fluorine Chem.*, 128(4):243–262, APR 2007.

[3] C. Arrouvel, S. C. Parker, and M. S. Islam. Lithium Insertion and Transport in the TiO_2-B Anode Material: A Computational Study. *Chem. Mater.*, 21(20):4778–4783, OCT 27 2009.

[4] N. W. Ashcroft and N. D. Mermin. *Solid state physics.* Holt, Rinehart and Winston, New York, 1976.

[5] F. Badway, A. N. Mansour, N. Pereira, J. F. Al-Sharab, F. Cosandey, I. Plitz, and G. G. Amatucci. Structure and electrochemistry of copper fluoride nanocomposites utilizing mixed conducting matrices. *Chem. Mater.*, 19(17):4129–4141, AUG 21 2007.

[6] L. Baggetto, P. Ganesh, C.-N. Sun, R. A. Meisner, T. A. Zawodzinski, and G. M. Veith. Intrinsic thermodynamic and kinetic properties of Sb electrodes for Li-ion and Na-ion batteries: experiment and theory. *J. Mater. Chem. A*, 1(27):7985–7994, 2013.

[7] P. Balaya, H. Li, L. Kienle, and J. Maier. Fully reversible homogeneous and heterogeneous Li storage in RuO_2 with high capacity. *Adv. Funct. Mater.*, 13(8):621–625, AUG 2003.

[8] R. W. Balluffi, S. M. Allen, and W. C. Carter. *Nucleation.* John Wiley and Sons, Inc., 2005.

[9] A.A. Belak, Y. Wang, and A. Van der Ven. Kinetics of Anatase Electrodes: The Role of Ordering, Anisotropy, and Shape Memory Effects. *Chem. Mater.*, 24(15):2894–2898, AUG 14 2012.

[10] J. Bhattacharya and A. Van der Ven. Phase stability and nondilute Li diffusion in spinel $Li_{1+x}Ti_2O_4$. *Phys. Rev. B*, 81(10), MAR 2010.

[11] J. Bhattacharya and A. Van der Ven. First-principles study of competing mechanisms of nondilute Li diffusion in spinel Li_xTiS_2. *Phys. Rev. B*, 83(14), APR 18 2011.

[12] P. E. Blöchl. Projector augmented-wave method. *Phys. Rev. B*, 50:17953–17979, Dec 1994.

[13] V. Blum, G.L.W. Hart, M.J. Walorski, and A. Zunger. Using genetic algorithms to map first-principles results to model Hamiltonians: Application to the generalized Ising model for alloys. *Phys. Rev. B*, 72(16), OCT 2005.

[14] M. Born and R. Oppenheimer. Quantum theory of molecules. *Ann. Physik*, 84(20):0457–0484, 1927.

[15] G. Brauer and F. Zintl. The constitution of phosphide, arsenide, antimonide and bismutide of lithium, natrium and kalium (23 Announcement on metal and alloy). *Z. Phys. Chem. B-Chem. E.*, 37(5/6):323–352, OCT 1937.

[16] P. G. Bruce, B. Scrosati, and J.-M. Tarascon. Nanomaterials for rechargeable lithium batteries. *Angewandte Chemie International Edition*, 47(16):2930–2946, 2008.

[17] J. Cabana, L. Monconduit, D. Larcher, and R. M. Palacin. Beyond Intercalation-Based Li-Ion Batteries: The State of the Art and Challenges of Electrode Materials Reacting Through Conversion Reactions. *Avd. Mater.*, 22(35):E170–E192, SEP 15 2010.

[18] R.j. Cava, D.W. Murphy, S. Zahurak, A. Santoro, and R.S. Roth. The Crystal-Structures Of The Lithium-Inserted Metal-Oxides $Li_{0.5}TiO_2$ Anatase, $LiTi_2O_4$ Spinel, And $Li_2Ti_2O_4$. *J. Solid State Chem.*, 53(1):64–75, 1984.

[19] A.S. Dalton, A.A. Belak, and A. Van der Ven. Thermodynamics of Lithium in TiO_2(B) from First Principles. *Chem. Mater.*, 24(9):1568–1574, MAY 8 2012.

[20] D. deFontaine. Cluster approach to order-disorder transformations in alloys. In Ehrenreich, H and Turnbull, D, editor, *Solid. State. Phys.*, volume 47 of *Solid State Phys.*, pages 33–176. Academic Press, 1994.

[21] R. E. Doe, K. A. Persson, Y. S. Meng, and G. Ceder. First-Principles Investigation of the Li-Fe-F Phase Diagram and Equilibrium and Nonequilibrium Conversion Reactions of Iron Fluorides with Lithium. *Chem. Mater.*, 20(16):5274–5283, AUG 26 2008.

[22] SL Dudarev, GA Botton, SY Savrasov, CJ Humphreys, and AP Sutton. Electron-energy-loss spectra and the structural stability of nickel oxide: An LSDA+U study. *Phys. Rev. B*, 57(3):1505–1509, JAN 15 1998.

[23] S. Evers and L. F. Nazar. New Approaches for High Energy Density Lithium-Sulfur Battery Cathodes. *Acc. Chem. Res.*, 46(5):1135–1143, MAY 21 2013.

[24] L.M.L. Fransson, J.T. Vaughey, R. Benedek, K. Edstrom, J.O. Thomas, and M.M. Thackeray. Phase transitions in lithiated Cu_2Sb anodes for lithium batteries: an in situ X-ray diffraction study. *Electrochem. Commum.*, 3(7):317–323, JUL 2001.

[25] Girishkumar, G. and McCloskey, B. and Luntz, A. C. and Swanson, S. and Wilcke, W. Lithium - Air Battery: Promise and Challenges. *J. Phys.Chem. Lett.*, 1(14):2193–2203, JUL 15 2010.

[26] T.D. Hatchard and J.R. Dahn. In situ XRD and electrochemical study of the reaction of lithium with amorphous silicon. *J. Electrochem. Soc.*, 151(6):A838–A842, 2004.

[27] G. Henkelman and H. Jonsson. Improved tangent estimate in the nudged elastic band method for finding minimum energy paths and saddle points. *J. Chem. Phys.*, 113(22):9978–9985, DEC 8 2000.

[28] F. Herman, J.P. Van Dyke, and I.B. Ortenburger. Improved Statistical Exchange Approximation For Inhomogeneous Many-Electron Systems. *Phys. Rev. Lett*, 22(16):807–811, 1969.

[29] K.C. Hewitt, L.Y. Beaulieu, and J.R. Dahn. Electrochemistry of InSb as a Li insertion host problems and prospects. *J. Electrochem. Soc.*, 148(5):A402–A410, MAY 2001.

[30] B. S. Hickman. Formation Of Omega Phase In Titanium And Zirconium Alloys - A Review. *J. Mater. Sci*, 4(6):554–563, 1969.

[31] Y.-Y Hu, Z. Liu, K.-W. Nam, O. J. Borkiewicz, J. Cheng, X. Hua, Matthew T. Dunstan, X. Yu, K. M. Wiaderek, L.-S. Du, K. W. Chapman, P. J. Chupas, X.-Q. Yang, and C. P. Grey. Origin of additional capacities in metal oxide lithium-ion battery electrodes. *Nat. Mater.*, 12(12):1130–1136, DEC 2013.

[32] S. Kerisit, K. M. Rosso, Z. Yang, and J. Liu. Computer Simulation of the Phase Stabilities of Lithiated TiO_2 Polymorphs. *J. Phys. Chem. C*, 114(44):19096–19107, NOV 11 2010.

[33] B. Key, M. Morcrette, J.-M. Tarascon, and C. P. Grey. Pair Distribution Function Analysis and Solid State NMR Studies of Silicon Electrodes for Lithium Ion Batteries: Understanding the (De)lithiation Mechanisms. *J.Am.Chem.Soc.*, 133(3):503–512, JAN 26 2011.

[34] A. G. Khachaturian. *Theory of structural transformations in solids*. Wiley, New York, 1983.

[35] S.W. Kim, D.H. Seo, X. Ma, G. Ceder, and K. Kang. Electrode Materials for Rechargeable Sodium-Ion Batteries: Potential Alternatives to Current Lithium-Ion Batteries. *Adv. Energy Mater.*, 2(7, SI):710–721, JUL 2012.

[36] A.F. Kohan, P.D. Tepesch, G. Ceder, and C. Wolverton. Computation of alloy phase diagrams at low temperatures. *Comput. Mater. Sci.*, 9(3-4):389–396, JAN 1998.

[37] W. Kohn and L.J. Sham. Self-Consistent Equations Including Exchange and Correlation Effects. *Phys. Rev.*, 140(4A):1133–1138, 1965.

[38] G. Kresse and J. Furthmüller. Efficient iterative schemes for *ab initio* total-energy calculations using a plane-wave basis set. *Phys. Rev. B*, 54:11169–11186, Oct 1996.

[39] G. Kresse and J. Furthmller. Efficiency of ab-initio total energy calculations for metals and semiconductors using a plane-wave basis set. *Comput. Mater. Sci.*, 6(1):15 – 50, 1996.

[40] G. Kresse and D. Joubert. From ultrasoft pseudopotentials to the projector augmented-wave method. *Phys. Rev. B*, 59:1758–1775, Jan 1999.

[41] A. V. Krukau, O. A. Vydrov, A. F. Izmaylov, and G. E. Scuseria. Influence of the exchange screening parameter on the performance of screened hybrid functionals. *J. Chem. Phys.*, 125(22):224160, 2006.

[42] M. Levy. Universal Variational Functionals Of Electron-Densities, 1St-Order Density-Matrices, And Natural Spin-Orbitals And Solution Of The V-Representability Problem. *Proc. Natl. Acad. Sci*, 76(12):6062–6065, 1979.

[43] Y.-C. Lu, B. M. Gallant, D. G. Kwabi, J. R. Harding, R. R. Mitchell, M. S. Whittingham, and Y. Shao-Horn. Lithium-oxygen batteries: bridging mechanistic understanding and battery performance. *Energy Environ. Sci.*, 6:750–768, 2013.

[44] R. Malini, U. Uma, T. Sheela, M. Ganesan, and N.G. Renganathan. Conversion reactions: a new pathway to realise energy in lithium-ion batteryreview. *Ionics*, 15(3):301–307, 2009.

[45] R. M. Martin. *Electronic structure: basic theory and practical methods*. Cambridge University Press, Cambridge, UK ; New York, 2004.

[46] S. Matsuno, M. Noji, T. Kashiwagi, M. Nakayama, and M. Wakihara. Construction of the ternary phase diagram for the Li-Cu-Sb system as the anode material for a lithium ion battery. *J.Phys. Chem. C*, 111(20):7548–7553, MAY 24 2007.

[47] S. Matsuno, M. Noji, M. Nakayama, M. Wakihara, Y. Kobayashi, and H. Miyashiro. Dynamics of phase transition in Li-Cu-Sb anode material for rechargeable lithium ion battery. *J. Electrochem. Soc.*, 155(2):A151–A157, 2008.

[48] D. A. McQuarrie. *Statistical thermodynamics*. Harper & Row, New York, 1973.

[49] M. Morcrette, D. Larcher, J.-M. Tarascon, K. Edstrom, J. T. Vaughey, and M. M. Thackeray. Influence of electrode microstructure on the reactivity of Cu_2Sb with lithium. *Electrochim. Acta*, 52(17):5339–5345, MAY 5 2007.

[50] M. Morcrette, P. Rozier, L. Dupont, E. Mugnier, L. Sannier, J. Galy, and J.-M. Tarascon. A reversible copper extrusion-insertion electrode for rechargeable Li batteries. *Nat. Mater.*, 2(11):755–761, NOV 2003.

[51] A. Mukhopadhyay and B. W. Sheldon. Deformation and stress in electrode materials for Li-ion batteries. *Prog. Mater. Sci.*, 63:58–116, Jun. 2014.

[52] W. Muller. Preparation And Crystal-Structure Of Li_2Sb. *Z. Naturforsch. B.*, 32(3):357–359, 1977.

[53] N. Nitta and G. Yushin. High-Capacity Anode Materials for Lithium- Ion Batteries: Choice of Elements and Structures for Active Particles. *Part. Part. Syst. Char.*, 31(3):317–336, MAR 2014.

[54] M.N. Obrovac and L. Christensen. Structural changes in silicon anodes during lithium insertion/extraction. *Electrochem. Solid-State Lett.*, 7(5):A93–A96, 2004.

[55] Y. Oumellal, A. Rougier, G. A. Nazri, J-M. Tarascon, and L. Aymard. Metal hydrides for lithium-ion batteries. *Nat. Mater.*, 7(11):916–921, NOV 2008.

[56] V. Palomares, P. Serras, I. Villaluenga, K. B. Hueso, J. Carretero-Gonzalez, and T. Rojo. Na-ion batteries, recent advances and present challenges to become low cost energy storage systems. *Energy Environ. Sci.*, 5:5884–5901, 2012.

[57] C.-M. Park, J.-H. Kim, H. Kim, and H.-J. Sohn. Li-alloy based anode materials for li secondary batteries. *Chem. Soc. Rev.*, 39:3115–3141, 2010.

[58] C.-M. Park, S. Yoon, S.-I. Lee, J.-H. Kim, J.-H. Jung, and H.-J. Sohn. High-rate capability and enhanced cyclability of antimony-based composites for lithium rechargeable batteries. *J. Electrochem. Soc.*, 154(10):A917–A920, 2007.

[59] R. G. Parr and W. Yang. *Density-functional theory of atoms and molecules*. Oxford University Press ; Clarendon Press, New York : Oxford [England], 1989.

[60] M.C. Payne, M.P. Teter, D.C. Allan, T.A. Arias, and J.D. Joannopoulos. Iterative Minimization Techniques For Abinitio Total-Energy Calculations - Molecular-Dynamics And Conjugate Gradients. *Rev. Mod. Phys.*, 64(4):1045–1097, OCT 1992.

[61] W.B. Pearson. The Cu_2Sb And Related Structures. *Z Kristallogr*, 171(1-2):23–39, 1985.

[62] J. P. Perdew, K. Burke, and M. Ernzerhof. Generalized gradient approximation made simple. *Phys. Rev. Lett.*, 77:3865–3868, Oct 1996.

[63] J.P. Perdew and K. Burke. Comparison shopping for a gradient-corrected density functional. *Int. J. Quant. Chem.*, 57(3):309–319, FEB 5 1996. 8th International Congress of Quantum Chemistry, Prague, Czech Republic, JUN 19-23, 1994.

[64] J.P. Perdew and Y. Wang. Accurate and Simple Analytic Representation of The Electron-Gas Correlation-Energy. *Phys. Rev. B*, 45(23):13244–13249, JUN 15 1992.

[65] J.C. Phillips and L. Kleinman. New Method For Calculating Wave Functions In Crystals And Molecules. *Phys. Rev.*, 116(2):287–294, 1959.

[66] P. Poizot, S. Laruelle, S. Grugeon, L. Dupont, and J.-M. Tarascon. Nano-sized transition-metaloxides as negative-electrode materials for lithium-ion batteries. *Nature*, 407(6803):496–499, SEP 28 2000.

[67] J.M. Sanchez, F. Ducastelle, and D. Gratias. Generalized Cluster Description Of Multicomponent Systems. *Physica A*, 128(1-2):334–350, 1984.

[68] J. Sangster and A.D. Pelton. The Li-Sb (Lithium-Antimony) System. *J. Phase Equilib.*, 14(4):514–517, 1993.

[69] D. S. Sholl and J. A. Steckel. *Density functional theory a practical introduction*. Wiley, Hoboken, N.J., 2009.

[70] D. J. Singh. *Planewaves, pseudopotentials, and the LAPW method*. Kluwer Academic Publishers, Boston, 1994.

[71] S. Soliman. Theoretical investigation of Cu-containing materials with different valence structure types: $BaCu_2S_2$, Li_2CuSb, and LiCuS. *J. Phys. Chem. Solids*, 75(8):927–930, AUG 2014.

[72] P. L. Taberna, S. Mitra, P. Poizot, P. Simon, and J.-M. Tarascon. High rate capabilities Fe3O4-based Cu nano-architectured electrodes for lithium-ion battery applications. *Nat. Mater.*, 5(7):567–573, Jun 2006.

[73] J.-M. Tarascon. Key challenges in future Li-battery research. *Phil. Trans. R. Soc. A*, 368(1923):3227–3241, JUL 28 2010.

[74] J.-M. Tarascon, S. Grugeon, M. Morcrette, S. Laruelle, P. Rozier, and P. Poizot. New concepts for the search of better electrode materials for rechargeable lithium batteries. *C.R. Chimie*, 8(1):9 – 15, 2005.

[75] M.M. Thackeray, J.T. Vaughey, C.S. Johnson, A.J. Kropf, R. Benedek, L.M.L. Fransson, and K. Edstrom. Structural considerations of intermetallic electrodes for lithium batteries. *J. Power Sources*, 113(1):124–130, JAN 1 2003.

[76] M.P. Usikov and V.A. Zilbershtein. Orientation Relationship Between Alpha-Phases And Omega-Phases Of Titanium And Zirconium. *Phys. Status Solidi A*, 19(1):53–58, 1973.

[77] A. Van de Walle and M. Asta. Self-driven lattice-model monte carlo simulations of alloy thermodynamic properties and phase diagrams. *Modell. Simul. Mater. Sci. Eng.*, 10(5):521, 2002.

[78] A. Van der Ven, J. Bhattacharya, and A. A. Belak. Understanding Li Diffusion in Li-Intercalation Compounds. *Acc. Chem. Res.*, 46(5):1216–1225, MAY 21 2013.

[79] A. Van der Ven and G. Ceder. Lithium diffusion in layered Li_xCoO_2. *Electrochem. Solid-State Lett.*, 3(7):301–304, Jul. 2000.

[80] A. Van der Ven, G. Ceder, M. Asta, and P. D. Tepesch. First-principles theory of ionic diffusion with nondilute carriers. *Phys. Rev. B*, 64:184307, Oct 2001.

[81] A. Van der Ven, K. Garikipati, S. Kim, and M. Wagemaker. The Role of Coherency Strains on Phase Stability in Li_xFePO_4: Needle Crystallites Minimize Coherency Strain and Overpotential. *J. Electrochem. Soc.*, 156(11):A949–A957, 2009.

[82] A. Van der Ven, J. C. Thomas, Q. Xu, and J. Bhattacharya. Linking the electronic structure of solids to their thermodynamic and kinetic properties. *Math. Comput. Simul.*, 80(7, SI):1393–1410, March 2010.

[83] A. Van der Ven, J. C. Thomas, Q. Xu, B. Swoboda, and D. Morgan. Nondilute diffusion from first principles: Li diffusion in Li_xTiS_2. *Phys. Rev. B*, 78(10), SEP 2008.

[84] J.T. Vaughey, C.S. Johnson, A.J. Kropf, R. Benedek, M.M. Thackeray, H. Tostmann, T. Sarakonsri, S. Hackney, L. Fransson, K. Edstrom, and J.O. Thomas. Structural and mechanistic features of intermetallic materials for lithium batteries. *J. Power Sources*, 97-8(SI):194–197, JUL 2001. 10th International Meeting on Lithium Batteries, COMO, Italy, May 28-Jun 02, 2000.

[85] G. H. Vineyard. Frequency Factors And Isotope Effects In Solid State Rate Processes. *J. Phys. Chem. Solids*, 3(1-2):121–127, 1957.

[86] F. Wang, R. Robert, N. A. Chernova, N. Pereira, F. Omenya, F. Badway, X. Hua, M. Ruotolo, R. Zhang, L. Wu, V. Volkov, D. Su, B. Key, M. S. Whittingharn, C. P. Grey, G. G. Amatucci, Y. Zhu, and J. Graetz. Conversion Reaction Mechanisms in Lithium Ion Batteries: Study of the Binary Metal Fluoride Electrodes. *J. Am. Chem. Soc.*, 133(46):18828–18836, NOV 23 2011.

[87] M. Winter and J. O. Besenhard. Electrochemical lithiation of tin and tin-based intermetallics and composites. *Electrochim. Acta.*, 45(12):31 – 50, 1999.

[88] Q. Xu and A. Van der Ven. First-principles investigation of migration barriers and point defect complexes in B2-NiAl. *Intermetallics*, 17(5):319–329, MAY 2009.

[89] N. Yabuuchi, K. Kubota, M. Dahbi, and S. Komaba. Research development on sodium-ion batteries. *Chem. Rev.*, 114(23):11636–11682, 2014. PMID: 25390643.

[90] H.-C. Yu, C. Ling, J. Bhattacharya, J. C. Thomas, K. Thornton, and A. Van der Ven. Designing the next generation high capacity battery electrodes. *Energy Environ. Sci.*, 7:1760–1768, 2014.

[91] K. Zhang, M.B. Katz, B. Li, S.J. Kim, X. Du, X. Hao, J. R. Jokisaari, S. Zhang, G. W. Graham, A. Van der Ven, B. M. Bartlett, and X. Pan. Water-Free Titania-Bronze Thin Films with Superfast Lithium-Ion Transport. *Adv. Mater.*, 26(43):7365–7370, NOV 19 2014.

[92] Y. Zhang, G. Kresse, and C. Wolverton. Nonlocal First-Principles Calculations in Cu-Au and Other Intermetallic Alloys. *Phys. Rev. Lett.*, 112(7), FEB 20 2014.